Precision Spectroscopy of Coherent Dark States in Thermal Cesium Vapour

vorgelegt von

Alexa Nagel
aus
Bonn

im April 1999

Inauguraldissertation
zur
Erlangung des Doktorgrades
der Mathematisch-Naturwissenschaftlichen Fakultät

der

Rheinischen Friedrich-Wilhelms-Universität
zu Bonn

Angefertigt mit Genehmigung der Mathematisch-Naturwissenschaftlichen Fakultät der Rheinischen Friedrich-Wilhelms-Universität, Bonn

Referent: Prof. Dr. D. Meschede
Korreferent: Prof. Dr. K. Heinloth

Tag der Promotion: 24.6.1999

Contents

1 Introduction

Quantum mechanics has extended the concept of interference from classical waves to transition amplitudes between simultaneously possible processes. Well-known manifestations of this type of interference include, e.g., the observation of single particle interferometry which is destroyed by any sort of which-path information.

The phenomenon of coherent population trapping (CPT), characterized by a sharp decrease in absorption under resonant excitation of a three-level system by a bichromatic light field and first observed about 20 years ago, results from a combination of such interference processes between transition amplitudes and the concept of atomic coherence. In a resonantly excited two-level atom atomic coherence appears as the in-phase and quadrature components of the induced atomic dipole moment, which naturally involves both atomic levels. In a three-level atom with two ground states resonantly coupled to a common excited state by a bichromatic light field, coherences are induced similarly on both transitions. This, in turn, leads to the creation of coherence between the two ground states formerly not coupled to each other. Then an explanation of the CPT phenomenon is given by a description of the atom with the help of so-called coupled and non-coupled states which both consist of a coherent superposition of the two ground states. While destructive interference leads to a vanishing transition amplitude from the uncoupled to the excited state, atomic coherence is needed for this state to be stable so that atomic population can be accumulated over certain time intervals. The time evolution of the atomic system is such that it is always out of phase with the driving light fields. Thus atomic population is lost for absorption and fluorescence processes, the atom remains dark despite resonant illumination. Another approach towards coherent population trapping has been given, where scattering processes between the two ground states were considered [Coh92]. In this picture destructive interference between various Raman transition amplitudes again leads to a decrease in excited state population on Raman resonance.

The net effect of reduced absorption and fluorescence is well visible for a macroscopic ensemble of atoms, e.g., in a thermal vapour. In contrast to conventional 'bright' resonances, where steepest dispersion is always accompanied by maximum absorption, coherent population trapping combines an ultrahigh non-linear index of refraction [Sch95] with vanishing absorption. This is, of course, advantageous whenever a large resonant transmission signal is required. For instance, it has been shown possible to actually observe the propagation dynamics of light pulses travelling through an otherwise opaque medium at an astonishingly slow speed of only $10^{-7} \cdot c$ [Kas95, Hau99, Kas99].

But coherent population trapping is far from merely being an interesting phenomenon and several applications are currently being developed. For instance, laser cooling below the recoil limit was achieved with the help of a process called 'velocity-selective coherent population trapping' (VSCPT) [Asp88]. In a suitable experimental configuration atoms with low enough velocity are accumulated in a non-coupled state that depends both on internal atomic degrees of freedom and

translational momentum, thus salvaging the atom from further heating by photon scattering. A slightly different atomic level configuration has led to the prediction and observation of lasing without population inversion [ZIB95, LUK96] which is discussed as a method to construct short wavelength lasers. More possibilities have been discussed and demonstrated, as reviewed by ARIMONDO [ARI96A].

A very promising application arises from calculations that compare the quantum noise sensitivity limit of a conventional optical pumping magnetometer (OPM) with that of a CPT-based device [SCU92, FLE94]. It was predicted for a special configuration that the ultimate sensitivity of the latter could by far exceed that of an OPM and even the best devices presently available, so-called SQUIDs (superconducting quantum interference device). Even possible applications with respect to the search for time reversal violation in atoms have been proposed [FLE95].

The work of this thesis is closely connected with the concept of an experimental implementation of such a high sensitivity magnetometer. Because recent advances in semiconductor laser technology have opened up new possibilities to construct a very compact and robust device it is also hoped to find a wide range of more practical applications, e.g., in medicine. Since detailed understanding of many details and control of systematic effects are essential for reliable operation of such a magnetometer the major focus of this thesis lies on a detailed characterization of CPT resonances in thermal cesium vapour. For practical reasons (atomic level configuration, availability of diode lasers, high enough vapour pressure at room temperature etc.) this is currently the medium of choice but an extension to rubidium is planned.

The first two chapters will give an introduction into the theoretical models developed in order to understand the CPT resonance dependence on a multitude of external parameters for the special experimental configurations used.

Chapter three describes the two different experimental configurations. Whereas the initial set-up was characterized by the versatility needed for many systematic investigations of CPT resonances, the new set-up, which is based on a novel type diode laser, already constitutes a step towards an extremely simple and robust device as it is needed for practical applications outside the laboratory environment.

In chapter four which occupies major parts of this thesis a wide range of systematic investigations is reported and compared with the theoretical models of the first chapters. This also includes the search for possible optimization of experimental parameters. For instance, the use of buffer gas techniques facilitated the reduction of the CPT linewidth observed to below 50 Hz.

The contents of the last chapter consists of two proof-of-principle experiments for the sensitive detection of small magnetic fields and the determination of the g-factor ratio. Although the set-up was far from being optimized, oscillating fields in the kHz range with a flux density amplitude of only several pT could already be detected.

2 Coherent Population Trapping (CPT)

2.1 Coherent population trapping in a Λ-system

The interaction of an atomic three-level system in Λ-configuration with a near-resonant bichromatic light field exhibits the intriguing quantum mechanical phenomenon of coherent population trapping (CPT). As indicated by the name, under suitable resonance conditions coherent interaction with the two light fields has the atom trapped in a particular ground state superposition that is not coupled to the excited state any more due to transition amplitude interference. Hence, resonant excitation and fluorescence are suppressed dramatically. To the observer this process appears as a 'dark resonance' with a narrow linewidth determined in principle by ground state properties. First experimental evidence of this effect goes back to 1976 [ALZ76].

Efficient preparation of this dark state requires a suitable level configuration which is depicted in fig. 2.1. Two long-lived ground states $|1\rangle$ and $|2\rangle$ are coupled to a common excited state $|3\rangle$ by a bichromatic light field with frequency components ω_1, ω_2, where each frequency component is assumed to interact with one of the transitions only.

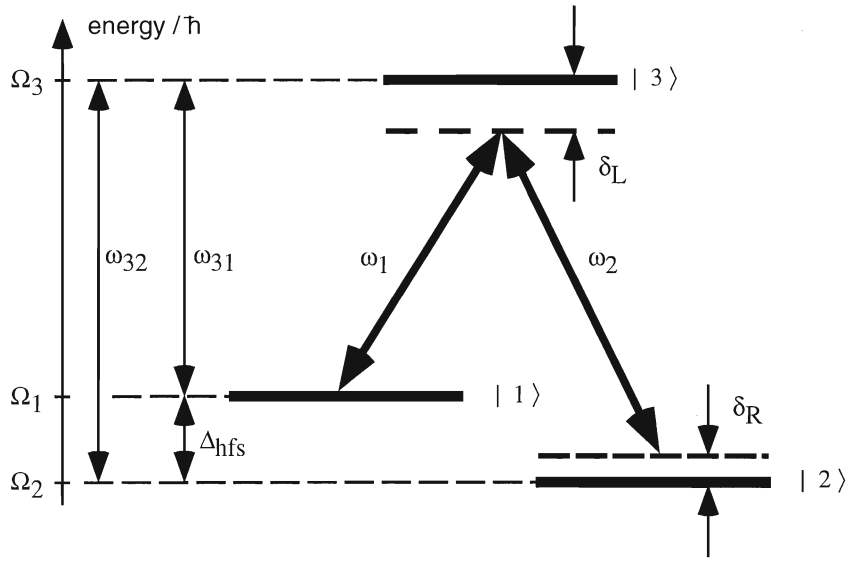

Figure 2.1: *Level configuration for the observation of CPT resonances. The notation introduced here will be used throughout the thesis.*

Optical pumping is the most obvious process to occur in such a system: in the presence of only one laser field depopulation pumping transfers atomic population into the respective uncoupled ground state where it can no longer absorb the laser light. Hence, after a time determined by the ratio of the excitation to spontaneous decay rate the medium appears dark. The presence of the second laser field, however, again leads to strong absorption from the formerly uncoupled state. Thus increased absorption over a frequency range roughly corresponding to the homogeneous

linewidth of the excited state is expected for a resonant bichromatic field in such a Λ-system. In addition to this effect the experiment also shows a dramatic decrease in absorption over a normally much narrower frequency range: coherent population trapping occurs if the difference frequency of the two light fields matches the ground state splitting, even if both light fields alone resonantly interact with their respective levels. The following paragraphs will explain this behaviour in more detail and present some theoretical considerations which will be made use of in later chapters.

The system under investigation includes the atomic levels denoted as in fig. 2.1 and the light field $E = E_1 \cos(\omega_1 t + \varphi_1) + E_2 \cos(\omega_2 t + \varphi_2)$ which will always be treated purely classically. As usual the Rabi frequencies g_1, g_2 characterizing interaction strengths are defined as

$$g_i = -\frac{d_{3i} E_i}{\hbar} \tag{2.1}$$

$$g_{\text{eff}} = \sqrt{|g_1|^2 + |g_2|^2} \tag{2.2}$$

where $d_{3i} = -e \langle 3| \hat{r} |i\rangle$, $i = 1, 2$, denotes the matrix elements of the electric dipole operator $\hat{d}$. Polarization dependence will be discussed in a later chapter (see 3.3) so that in this section vector properties of $\hat{d}$ will be ignored and all Rabi frequencies are assumed real.

In the semiclassical approach the Hamiltonian describing the interaction of the atom with the bichromatic light field (in rotating wave and electric dipole approximation) reads:

$$\begin{aligned} H &= H_0 + H_{\text{int}} \\ &= \sum_i \hbar \Omega_i |i\rangle \langle i| + \frac{\hbar g_1}{2} e^{-i\omega_1 t - i\varphi_1} |3\rangle \langle 1| + \frac{\hbar g_2}{2} e^{-i\omega_2 t - i\varphi_2} |3\rangle \langle 2| + h.c. \end{aligned} \tag{2.3}$$

Instead of the bare ground states $|1\rangle$ and $|2\rangle$ it is instructive to consider the so-called coupled and non-coupled states $|C\rangle$ and $|NC\rangle$ defined as:

$$|NC\rangle = \frac{1}{g_{\text{eff}}} (g_2 e^{-i\Omega_1 t} |1\rangle - g_1 e^{-i\Omega_2 t} e^{i(\varphi_2 - \varphi_1)} |2\rangle) \tag{2.4}$$

$$|C\rangle = \frac{1}{g_{\text{eff}}} (g_1 e^{-i\Omega_1 t} |1\rangle + g_2 e^{-i\Omega_2 t} e^{i(\varphi_2 - \varphi_1)} |2\rangle). \tag{2.5}$$

$|C\rangle, |NC\rangle$ are orthogonal to each other and $\{|C\rangle, |NC\rangle, |3\rangle\}$ is a basis for the system under investigation. On Raman resonance, i.e., if $\omega_2 - \omega_1 = \Omega_1 - \Omega_2$, $|NC\rangle$ is a solution of the Schrödinger equation $i\hbar \, \partial/\partial t \, |\psi\rangle = H |\psi\rangle$. Furthermore, one easily shows that, for $\varphi_1 = \varphi_2$,

$$\langle 3| H_{\text{int}} |NC\rangle = 0 \qquad \text{whereas} \qquad \langle 3| H_{\text{int}} |C\rangle = \frac{\hbar g_{\text{eff}}}{2} e^{-i(\Omega_1 + \omega_1)t - 2i\varphi_1} . \tag{2.6}$$

An atom finding itself in the non-coupled (or 'dark') state $|NC\rangle$ is trapped and cannot leave the state via the interaction with the light fields since the transition amplitude to the excited state vanishes. But in order for $|NC\rangle$ to remain 'dark', coherence properties of the light fields are crucial. If φ_1, φ_2 fluctuate in time the atom in state $|NC\rangle$ at time $t = t_0$ will not follow the time development of $|NC\rangle$ but also get an admixture of the orthogonal state $|C\rangle$, since $|NC\rangle$

and $|C\rangle$ are mainly distinguished by a 180° relative phase shift between the two light fields. But as soon as an admixture of $|C\rangle$, which itself is not an eigenstate of H, comes into play the atom again takes part in absorption-emission cycles and thus leaves the dark state. However, in this picture the atom will actually never get into the dark state since stimulated emission into that state is not possible either.

2.2 Semiclassical density matrix approach

In order to find a more adequate approach towards the CPT phenomenon one has to include spontaneous emission into the model because it is the essential process for coherent dark state preparation. In the semiclassical approach this is done with the help of the density matrix formalism where spontaneous emission and other relaxation processes are included phenomenologically via a relaxation operator $\hat{R}$. Then the time development of the density operator $\hat{\rho} = \sum_{i,j} \alpha_{ij} |i\rangle \langle j|$ is given by the Liouville equation:

$$i\hbar \frac{\partial}{\partial t}\hat{\rho} = [H, \hat{\rho}] + \hat{R}\hat{\rho} \, . \tag{2.7}$$

Diagonal elements $\hat{\rho}_{ii}$ of the density matrix correspond to the populations of the i-th level whereas off-diagonal elements $\hat{\rho}_{ij}$ denote atomic coherences.

From a solution of the density matrix equations the expectation values of an operator $\hat{O}$ can be calculated via the relation

$$\langle \psi | \hat{O} | \psi \rangle = \mathrm{Tr}(\hat{\rho}\hat{O}) \, . \tag{2.8}$$

Using the Hamiltonian given in eq. (2.3) and introducing the following relaxation rates and notations:

$$\begin{aligned}
\delta_L &: \quad \text{optical detuning of the first laser, } \delta_L = \omega_1 - \omega_{31} \\
\delta_R &: \quad \text{Raman detuning, } \delta_R = \omega_2 - \omega_1 - \Delta_{\mathrm{hfs}} \\
\gamma_1, \gamma_2 &: \quad \text{optical population decay rates,} \\
\Gamma_1, \Gamma_2 &: \quad \text{optical dephasing rates,} \\
\gamma_{12} &: \quad \text{ground state population decay rate,} \\
\Gamma_{12} &: \quad \text{ground state dephasing rate,}
\end{aligned} \tag{2.9}$$

the density matrix equations result as :

$$\begin{aligned}
\tfrac{\partial}{\partial t}\rho_{11} &= \gamma_1\rho_{33} + g_1\mathrm{Im}(\rho_{31}) + \gamma_{12}(\rho_{22}-\rho_{11}) \\
\tfrac{\partial}{\partial t}\rho_{22} &= \gamma_2\rho_{33} + g_2\mathrm{Im}(\rho_{32}) - \gamma_{12}(\rho_{22}-\rho_{11}) \\
\tfrac{\partial}{\partial t}\rho_{33} &= -(\gamma_1+\gamma_2)\rho_{33} - g_1\mathrm{Im}(\rho_{31}) - g_2\mathrm{Im}(\rho_{32}) \\
\tfrac{\partial}{\partial t}\mathrm{Re}(\rho_{31}) &= -\Gamma_1\mathrm{Re}(\rho_{31}) - \delta_L\mathrm{Im}(\rho_{31}) - \frac{g_2}{2}\mathrm{Im}(\rho_{12}) \\
\tfrac{\partial}{\partial t}\mathrm{Im}(\rho_{31}) &= -\Gamma_1\mathrm{Im}(\rho_{31}) + \delta_L\mathrm{Re}(\rho_{31}) + \frac{g_1}{2}(\rho_{33}-\rho_{11}) - \frac{g_2}{2}\mathrm{Re}(\rho_{12}) \\
\tfrac{\partial}{\partial t}\mathrm{Re}(\rho_{32}) &= -\Gamma_2\mathrm{Re}(\rho_{32}) - (\delta_L+\delta_R)\mathrm{Im}(\rho_{32}) + \frac{g_1}{2}\mathrm{Im}(\rho_{12}) \\
\tfrac{\partial}{\partial t}\mathrm{Im}(\rho_{32}) &= -\Gamma_2\mathrm{Im}(\rho_{32}) + (\delta_L+\delta_R)\mathrm{Re}(\rho_{32}) + \frac{g_2}{2}(\rho_{33}-\rho_{22}) - \frac{g_1}{2}\mathrm{Re}(\rho_{12}) \\
\tfrac{\partial}{\partial t}\mathrm{Re}(\rho_{12}) &= -\Gamma_{12}\mathrm{Re}(\rho_{12}) - \delta_R\mathrm{Im}(\rho_{12}) + \frac{g_1}{2}\mathrm{Im}(\rho_{32}) + \frac{g_2}{2}\mathrm{Im}(\rho_{31}) \\
\tfrac{\partial}{\partial t}\mathrm{Im}(\rho_{12}) &= -\Gamma_{12}\mathrm{Im}(\rho_{12}) + \delta_R\mathrm{Re}(\rho_{12}) - \frac{g_1}{2}\mathrm{Re}(\rho_{32}) + \frac{g_2}{2}\mathrm{Re}(\rho_{31}).
\end{aligned} \tag{2.10}$$

All coherences ρ_{ij} are viewed in a rotating frame, i.e., a unitary transformation has eliminated explicit time dependence from the system of equations:

$$\begin{aligned}
\rho_{31} &= e^{i(\omega_1 t+\varphi_1)}\hat{\rho}_{31} \\
\rho_{32} &= e^{i(\omega_2 t+\varphi_2)}\hat{\rho}_{32} \\
\rho_{12} &= e^{i((\omega_2-\omega_1)t+\varphi_2-\varphi_1)}\hat{\rho}_{12}\,.
\end{aligned} \tag{2.11}$$

As none of the experiments to be described in this thesis was concerned with the actual time development of any quantum mechanical observable it is sufficient here to find steady state solutions for the density matrix equations. This can be done analytically without any further approximations. From eqs. (2.10) the density matrix elements $\mathrm{Re}(\rho_{32})$, $\mathrm{Im}(\rho_{32})$ that are relevant for a comparison with the experimentally recorded transmission signal can be calculated as

$$\mathrm{Re}(\rho_{32}) = \frac{(A_r+B_r\delta_L^2)\delta_R^3 + (C_r+D_r\delta_L^2)\delta_L\delta_R^2 + (E_r+F_r\delta_L^2)\delta_R + (G_r+H_r\delta_L^2)\delta_L}{N} \tag{2.12}$$

$$\mathrm{Im}(\rho_{32}) = \frac{(A_i+B_i\delta_L^2)\delta_R^2 + C_i\delta_L\delta_R + D_i\delta_L^2 + E_i}{N}, \tag{2.13}$$

with:

$$\begin{aligned}
N =& (A+B\delta_L^2)\delta_R^4 + (C+D\delta_L^2)\delta_L\delta_R^3 + (E+F\delta_L^2+G\delta_L^4)\delta_R^2 + (H+J\delta_L^2)\delta_L\delta_R \\
&+ K + L\delta_L^2 + M\delta_L^4\,.
\end{aligned} \tag{2.14}$$

The coefficients depend on decay rates and Rabi frequencies and are given explicitly in appendix B. $\mathrm{Im}(\rho_{32})$, $\mathrm{Re}(\rho_{32})$ describe the absorptive and dispersive properties of the system, respectively. An important point about these analytical formulae is that no further assumptions concerning Rabi frequencies and decay rates were made. Other authors reporting similar formulae have

always restricted themselves to either more symmetric systems (equal decay rates and Rabi frequencies) or the strong pump-weak probe situation ([ORR79], [KEL94], also see the review article by ARIMONDO [ARI96A]). But in order to realistically model the experimental situation (see chapter 3) it is essential to consider the asymmetric situation for arbitrary Rabi frequencies.

Before proceeding to the derivation of experimentally observable quantities from eqs. (2.12), (2.13) some interesting features of CPT resonances can already be discussed for the bare formulae for ρ_{32}. Figs. 2.2 and 2.3 illustrate calculations of ρ_{32} for two typical experimental situations, i.e., for both high and low intensity and ground state decay rates.

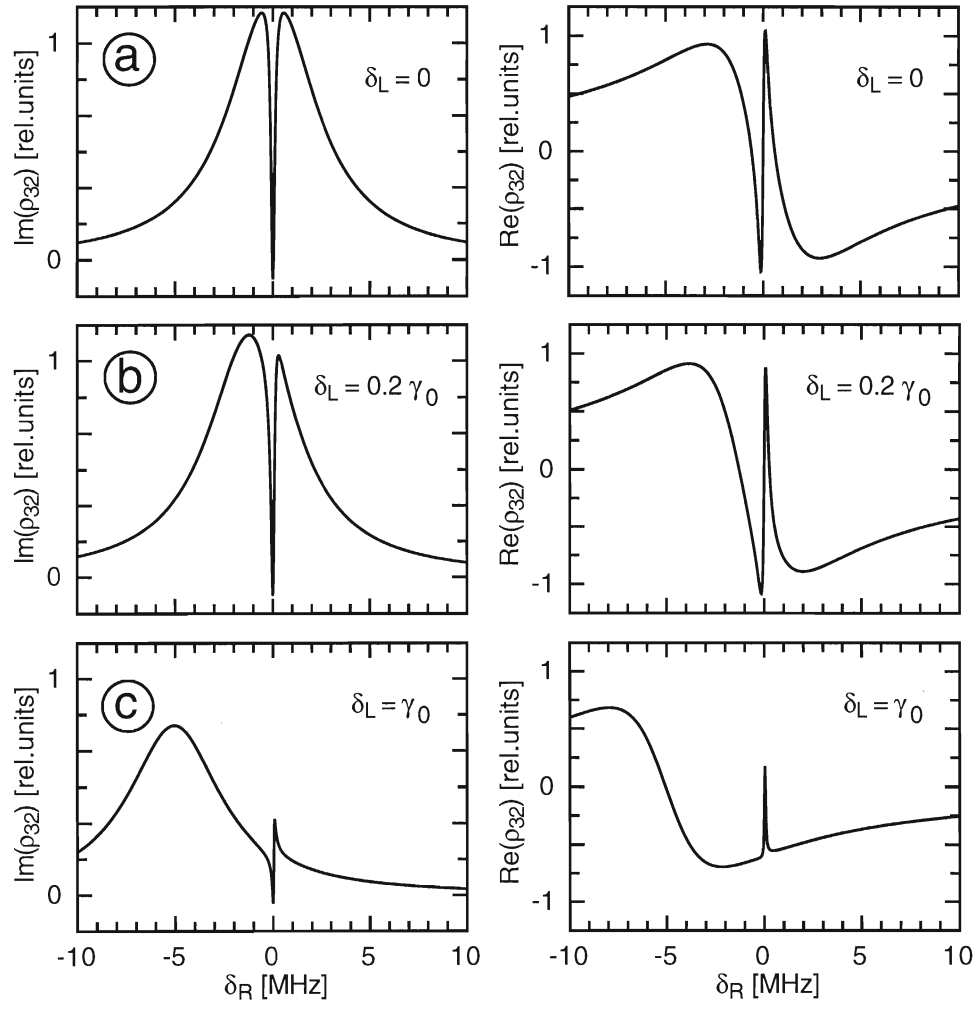

Figure 2.2: *Absorptive and dispersive dark resonance line shapes calculated from eqs.* (2.12), (2.13) *for various optical detunings* δ_L *and with the following parameters:* $\gamma_1 = 4\,\mathrm{MHz}$, $\gamma_{12} = \Gamma_{12} = 10\,\mathrm{kHz}$, $\gamma_2 = \frac{1}{4}\gamma_1$, $\Gamma_1 = \Gamma_2 = \frac{1}{2}(\gamma_1 + \gamma_2) =: \frac{1}{2}\gamma_0$, $g_1 = \frac{1}{4}\gamma_1$, $g_2 = \frac{1}{16}\gamma_1$. *For these rather high Rabi frequencies saturation broadening of the dark resonance allows to plot the dark resonance together with the optical resonance. Whereas the optical resonance directly shifts with* δ_L *the dark resonance shift is a much more subtle function of* δ_L.

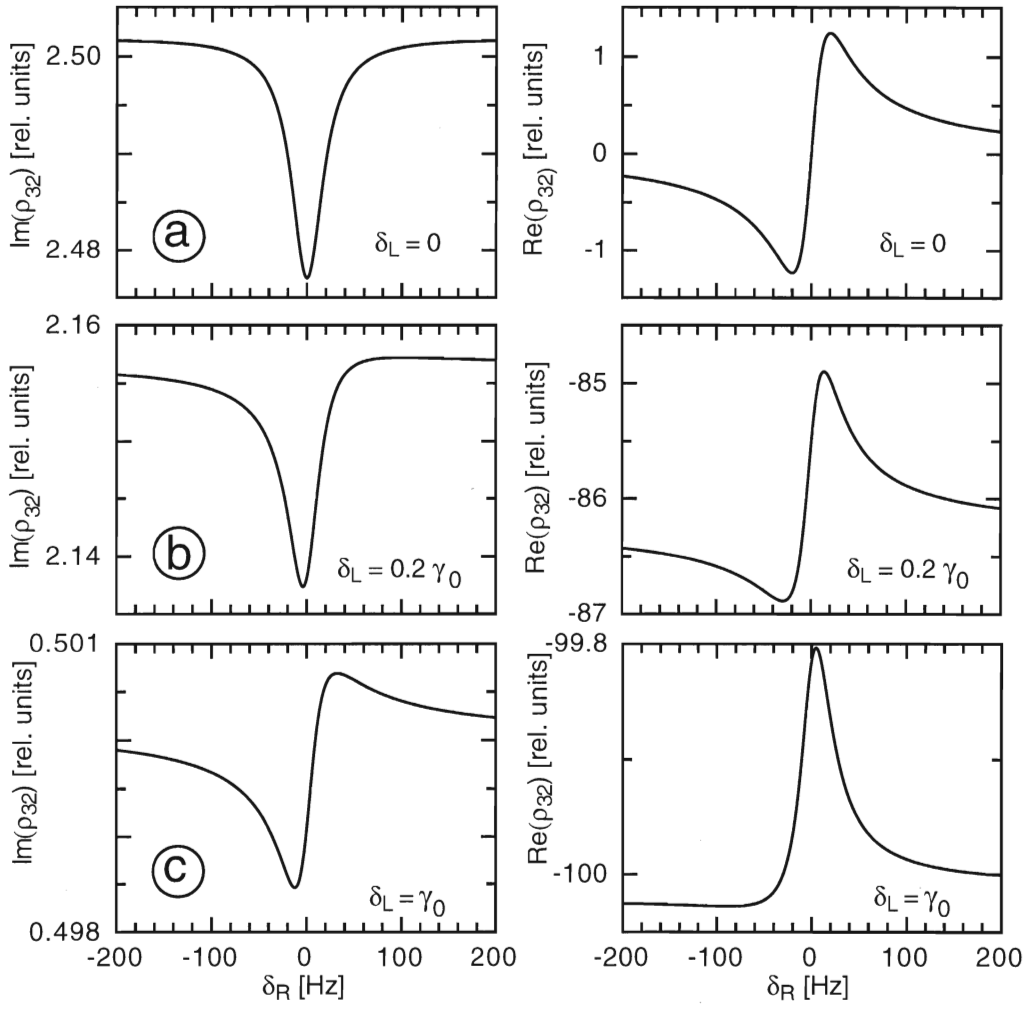

Figure 2.3: *Absorptive and dispersive dark resonance line shapes calculated from eqs.* (2.12), (2.13) *for the same optical detunings and decay rates as in fig. 2.2 but with different parameters* $\gamma_{12} = \Gamma_{12} = 20\,\mathrm{Hz}$, $g_1 = \frac{1}{4000}\gamma_1$, $g_2 = \frac{1}{4000}\gamma_2$. *Since in this case the optical resonance is much broader than the dark resonance only the latter is plotted.*

For zero optical detuning $\delta_L = 0$ both the broad optical resonance and the narrow dark resonance are centered at $\delta_R = 0$ and exhibit simple Lorentzian line shapes. With δ_L different from zero the dark resonance gradually shifts to $\delta_R \neq 0$, gets asymmetric, and its overall amplitude decreases. For larger detunings δ_L the absorption dip becomes accompanied by a lateral absorption peak. This behaviour has also been observed experimentally [ALZ76]. A quantitative description of all these effects depends in a rather complicated manner on Rabi frequencies and decay rates.

Although the experimental situation is more complicated than the case of an ideal 3-level atom at rest similar line shifts and asymmetries can actually be observed (see chapters 5.2, 5.4) and therefore it is worthwhile to investigate these asymmetries in more detail. In an experiment performed in thermal cesium vapour the Doppler shift due to the Maxwellian velocity distribution has the atoms experience different values of δ_L. But since the contrast of the dark resonance

decreases for increasing δ_L the main contribution towards the final signal stems from velocity classes with small δ_L. Hence it appears reasonable to consider a Taylor expansion of ρ_{32} with respect to δ_L. Partial fraction decomposition of the first-order Taylor expansion (which is a good approximation as long as $\delta_L \ll \gamma_0$, with $\gamma_0 = \gamma_1 + \gamma_2$) allows to separate contributions towards the line shape of the optical resonance from those of the dark resonance, where the latter are described by

$$\frac{1}{g_2}\mathrm{Re}^{(\mathrm{CPT})}(\rho_{32}) = \frac{D_1\delta_R}{\delta_R^2+N_0} + \frac{D_2\delta_R}{\delta_R^2+N_0}\delta_L + \frac{D_3\delta_R}{(\delta_R^2+N_0)^2}\delta_L + \frac{D_4}{\delta_R^2+N_0}\delta_L \tag{2.15}$$

$$-\frac{1}{g_2}\mathrm{Im}^{(\mathrm{CPT})}(\rho_{32}) = \frac{A_1}{\delta_R^2+N_0} + \frac{A_2\delta_R}{\delta_R^2+N_0}\delta_L + \frac{A_3\delta_R}{(\delta_R^2+N_0)^2}\delta_L\,. \tag{2.16}$$

In principle, this decomposition is only of interest because it will be used for fitting procedures later on (see chapter 5.2), therefore the coefficients A_i, D_i are not listed explicitly. The coefficient N_0 relevant for the discussion of saturation broadening reads

$$N_0 = \frac{E}{2A} - \frac{1}{2A}\sqrt{E^2-4KA}\,, \tag{2.17}$$

with coefficients A, E, K given in appendix B. Similar terms describe the optical resonance but are of no interest here.

In this approximation the dark resonance line shapes as a function of δ_R are given by the superposition of three different curves: absorptive (A_1, D_4) and dispersive Lorentzians (D_1, D_2, A_2) and the derivative of an absorptive Lorentzian (D_3, A_3). In the absence of Doppler shifts all contributions have the same linewidth and position whereas their superposition curve appears shifted. Fig. 2.4 illustrates this decomposition of an asymmetric dark resonance line shape into the three contributions: (1) absorptive Lorentzian, (2) dispersive Lorentzian, (3) derivative of an absorptive Lorentzian, for both the absorptive and the dispersive parts, where the parameters are the same as in fig. 2.3(b).

In the approximation of an atom at rest with $\delta_L = 0$ the dark resonance line shape is simply given by the Lorentzian of the first term of eqs. (2.15), (2.16). Hence in this case the dark resonance linewidth γ_{CPT} can be inferred as

$$\gamma_{\mathrm{CPT}} = 2\sqrt{N_0}\,. \tag{2.18}$$

For further simplification one considers the case of a symmetric system with $g_1 = g_2 =: g$, $\Gamma_1 = \Gamma_2 =: \Gamma$, $\gamma_1 = \gamma_2 = 2\Gamma$ and $\gamma_{12} = k \cdot \Gamma_{12}$. The introduction of the parameter k pays attention to the fact that relaxation between the two hyperfine-split ground states is usually not dominated by radiative decay, hence $\gamma_{12} = \Gamma_{12}/2$ has not necessarily to be valid. For low intensities, i.e., small g, γ_{CPT} can be replaced by its second-order Taylor expansion:

$$\gamma_{\mathrm{CPT}} = 2\Gamma_{12} + \frac{1}{2\Gamma}\left(1 + \frac{1}{1-\frac{\Gamma_{12}}{\Gamma}}\right)g^2 \tag{2.19}$$

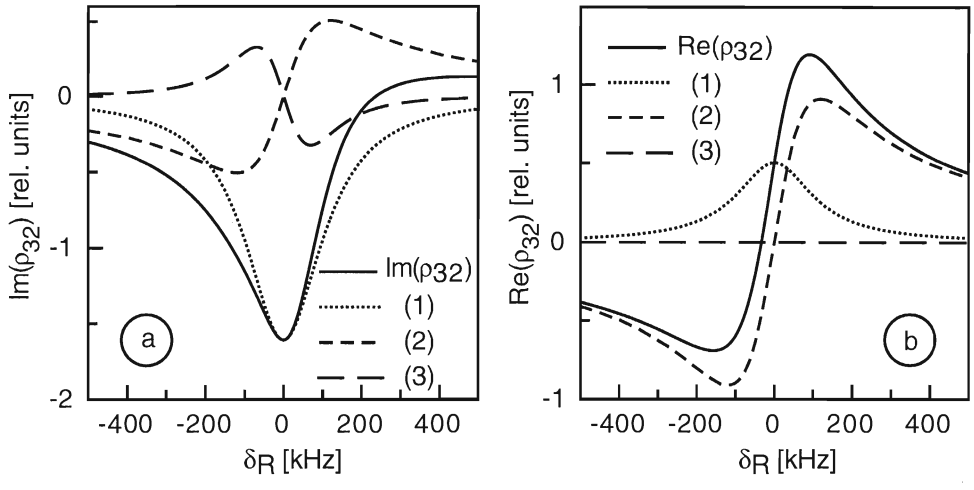

Figure 2.4: *Dark resonance line shape as a superposition of the three first-order Taylor expansion contributions: (a)* $\mathrm{Im}(\rho_{32})$*, (b)* $\mathrm{Re}(\rho_{32})$*. Dotted curves (1): absorptive Lorentzians, dashed curves (2): dispersive Lorentzians, dashed curves (3): derivatives of absorptive Lorentzians. Parameters used are the same as in fig. 2.3(b). Note that for* $\mathrm{Im}(\rho_{32})$ *the dispersion and absorption derivative contributions always show opposite sign. For this set of parameters the absorption derivative part only gives a negligible contribution to* $\mathrm{Re}(\rho_{32})$*.*

which is already independent of k. Finally, in the approximation of $\Gamma_{12} \ll \Gamma$ one gets

$$\gamma_{\mathrm{CPT}} = 2\Gamma_{12} + \frac{g^2}{\Gamma} \,. \tag{2.20}$$

This is exactly the result given in [Ari94], [Ari96a] without any details on derivation or validity limits. Under many experimental conditions the observed power broadening behaviour is in fact linear, thus at least qualitatively agreeing with eq. (2.20), despite the radical approximations necessary to arrive at this formula.

From the calculated line shapes for various optical detunings δ_L one can furthermore numerically determine the linewidth, amplitude, and position of the dark resonance as a function of δ_L, where 'position' shall always refer to the minimum of the absorption line. This was done using the same sets of parameters as in figs. 2.2 and 2.3, and the resulting curves are shown in fig. 2.5.

The curves show either axial symmetry (fig. 2.5(1) and (2)) or point symmetry (fig. 2.5(3)). Both the linewidth and line strength dependence on δ_L corresponds to an absorptive Lorentzian curve. The corresponding widths roughly equal the excited state linewidth, although the FWHM of fig. 2.5(1) appears to be slightly broader. Comparison of the situations (a) and (b) yields that these widths hardly depend on intensity. The fact that the CPT linewidth for the set of parameters (a) appears to increase with $|\delta_L|$ can be considered as an artifact due to the definition of the linewidth.

This CPT linewidth was always determined as the difference between the two frequencies for which the 'dark line' reached half its amplitude, which in the case of an almost dispersive

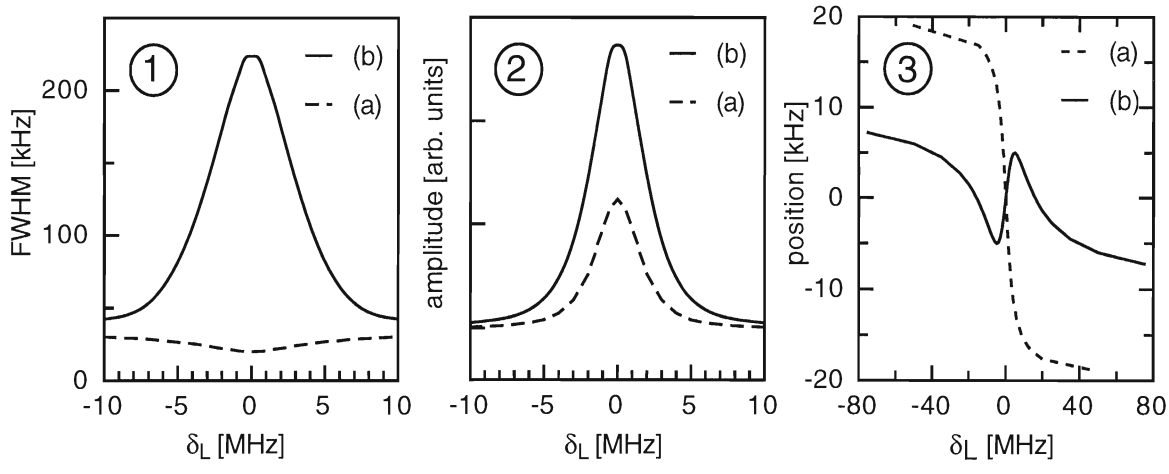

Figure 2.5: *Dark resonance dependence on the optical detuning δ_L:*
(1) FWHM, (2) amplitude, where the amplitude of curve (a) was enlarged by a factor of $2 \cdot 10^5$, (3) position, where the curve (a) was enlarged by a factor of 500, with:
(a) the same set of parameters as in fig. 2.3: $\gamma_{12} = \Gamma_{12} = 20\,Hz$, $g_1 = 1\,kHz$, $g_2 = 0.25\,kHz$;
(b) the same set of parameters as in fig. 2.2: $\gamma_{12} = \Gamma_{12} = 10\,kHz$, $g_1 = 1\,MHz$, $g_2 = 0.25\,MHz$.

line shape is not a very reasonable approach. The CPT position critically depends on Rabi frequencies and decay rates. In the particularly interesting parameter range of small δ_L the shift can even change sign and slope for altered parameters.

For a quantitative comparison with the experiment one has to take into account several additional aspects which will be discussed in the following chapter.

3 Theory of CPT resonances in thermal cesium vapour

In the preceding chapter coherent population trapping in a simple three-level Λ-system was discussed. But the situation encountered in an experiment performed in thermal cesium vapour is by far more complicated. Differences arise from both the complex internal level structure of the cesium atom and from the thermal motion of the atoms. Accordingly, this chapter deals with a suitable adaptation of the simple three-level model to realistic experimental conditions. The main concern of all theory presented here is to gain some physical insight into the observed phenomena and not to provide purely numerical solutions for a multilevel system. In chapter 5 quantitative comparison with the experiments will be sought for all the results developed here, in order to test the validity range of the simple models.

3.1 CPT resonances in thermal cesium vapour

All the experiments to be described in chapter 4 were performed on the cesium D_2 transition at 852 nm wavelength, the level configuration of which is depicted in fig. 3.1.

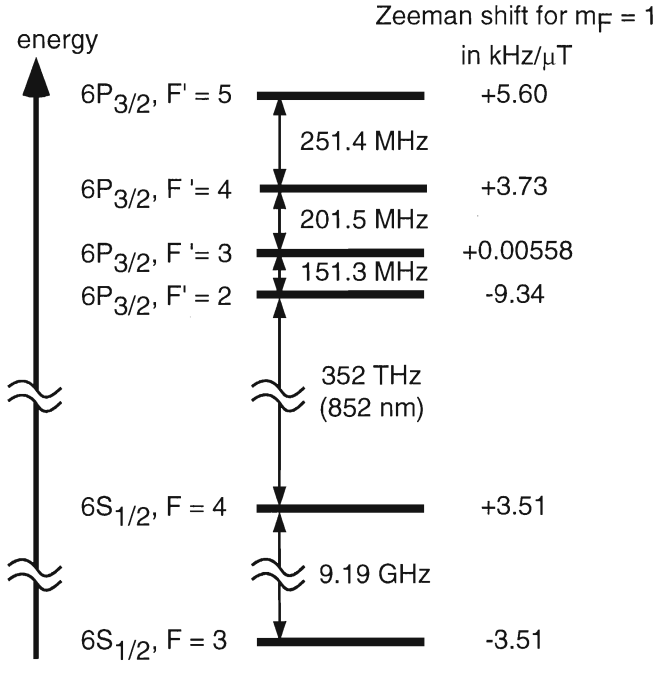

Figure 3.1: *Level configuration of the cesium D_2 line, including linear Zeeman shift rates.*

Atomic level structure Even at zero magnetic field the situation is more complicated than in the simple three-level Λ-system. The two hyperfine-split ground states $6S_{1/2}, F = 3, 4$ can form

a Λ-system with both the excited $6P_{1/2}$, $F' = 3$ and $F' = 4$ levels, whereas the $F' = 2, 5$ levels cannot simultaneously couple to both ground states due to electric dipole selection rules. It has been demonstrated theoretically as well as experimentally that the presence of additional atomic levels not involved in coherent dark state preparation considerably influences the dark resonance linewidth and the maximum transparency reached [REN97]. Further reduction of the dark resonance contrast due to background absorption can be expected for the experiment described here because the excited state hyperfine splitting is smaller than the thermal Doppler width. Either using a different level configuration such as the D_1 line which has the advantages of considerably larger hyperfine splittings and excited state components $F' = 3$, 4 only, or performing an atomic beam experiment with negligible Doppler width one could greatly increase the percentage of the overall transparency observed. In fact, a 90 % reduction of fluorescence intensity in the centre of the dark resonance has been demonstrated in an atomic beam experiment [KOR97].

Application of a magnetic field destroys the Zeeman degeneracy in all levels. Then the system under investigation gets even more complicated in that the number of atomic levels involved is increased from 6 to 48. The treatment of such a multilevel system will occupy major parts of this chapter.

Density matrix elements For a quantitative comparison with the experiments described in chapter 4 one has to calculate the transmission signal of a bichromatic field behind an optically thin medium of length l.

The macroscopic polarization P is given by $P = N\langle d\rangle$, where N is the number density of atoms and $\langle d\rangle$ the average induced atomic dipole moment which can be calculated according to eq. (2.8):

$$\begin{aligned}\langle d\rangle &= \mathrm{Tr}(\hat{\rho}\hat{d}) \\ &= \rho_{31}d_{31} + \rho_{32}d_{32} + c.c. \end{aligned} \tag{3.1}$$

On the other hand, for each optical frequency ω_j, the polarization is related to the complex non-linear atomic susceptibility $\chi(\omega_j) = \chi'(\omega_j) + i\chi''(\omega_j)$ via $P(\omega) = \epsilon_0\chi E$. Accordingly, the real and imaginary parts of χ can be calculated as

$$\chi'(\omega_j) = \frac{N}{\epsilon_0 E_j} d_{3j}\mathrm{Re}(\rho_{3j}) \tag{3.2}$$

$$\chi''(\omega_j) = \frac{N}{\epsilon_0 E_j} d_{3j}\mathrm{Im}(\rho_{3j})\,, \qquad j = 1, 2\,, \tag{3.3}$$

and the index of refraction $n = n' + i\,n''$ can be inferred via $n' - 1 \approx \frac{1}{2}\chi'$ and $n'' \approx \frac{1}{2}\chi''$.

For an optically thin vapour the transmission signal of the bichromatic light field is determined

from the indices of refraction $n_j = n'_j + i\,n''_j$ at the two optical transitions $j \to 3$:

$$\begin{aligned} E &= \sum_{j=1,2} E_j e^{i(n_j k_j l - \omega_j t)} + c.c. \\ &= \sum_{j=1,2} E_j e^{-i\omega_j t} e^{-\delta_j - i\phi_j} + c.c. \\ &\approx \sum_{j=1,2} E_j e^{-i\omega_j t}(1 - \delta_j - i\phi_j) + c.c. \end{aligned} \tag{3.4}$$

with

$$\delta_j = k_j l\, n''_j \tag{3.5}$$

$$\phi_j = -k_j l\, n'_j. \tag{3.6}$$

Due to the non-linearity of the interaction process each n_j depends on the interaction with both light fields. As it will be shown in chapter 5.2.1, the use of frequency modulation techniques allows to determine both δ_j and ϕ_j from the signal recorded with a single photodiode behind the medium.

Doppler distribution So far, the calculation has been valid for an atom at rest or with purely transverse velocity only. As all the experiments described in this thesis were carried out in thermal atomic vapour it is necessary to take the atomic velocity distribution into account. In the rest frame of an atom travelling with velocity $\vec{v}$ the laser frequencies appear Doppler-shifted according to

$$\omega_j \mapsto \omega_j - \vec{k_j} \cdot \vec{v}, \qquad j = 1, 2, \qquad \text{hence} \tag{3.7}$$

$$\delta_L \mapsto \delta_L - \omega_1 \frac{v}{c} \tag{3.8}$$

$$\delta_R \mapsto \delta_R - (\omega_2 - \omega_1)\frac{v}{c}, \tag{3.9}$$

where v should always refer to the velocity component along $\vec{k}$ only. Since dark resonance preparation is essentially a two-photon process, for copropagating laser beams Doppler broadening of the dark resonance is expected on the scale of the laser difference frequency at 9.2 GHz, whereas the optical transition directly suffers from the Doppler broadening at the optical frequencies. As usual, Doppler shifts were taken into account in that the function of interest is integrated over the Maxwellian Doppler profile $f_D(v)$ with the thermal velocity distribution of the atoms included via

$$n''(\delta_L, \delta_R) \mapsto \int f_D(v) n''(\delta_L - \omega_1 v/c, \delta_R - (\omega_2 - \omega_1)v/c) dv\,, \tag{3.10}$$

and similarly for n'. As the contrast of the dark resonance decreases with increasing optical detuning δ_L the Doppler integration tends to wash out line shifts and asymmetries since the main contributions arise from atoms with $\delta_L \approx 0$. However, residual shifts and line shape asymmetries can readily be detected in the experiments.

Atomic trajectories In principle, another aspect to bear in mind are atomic trajectories. Atoms travelling through the beam experience different intensities over the Gaussian beam profile. They might enter the interaction region at a certain time t_1, then travel inside the beam and finally leave at some time t_2. Minute modeling of this behaviour would include time dependent solutions of eq. (2.10) integrated over all possible atomic trajectories. The situation is slightly less complicated for atomic beam experiments where time dependence can be studied from the fluorescence emitted along the beam path [KOR97]. However, in all theoretical considerations presented here a simpler view was adopted in that a rectangular beam profile with an effective diameter d was assumed. d was determined such that both the maximum intensity and the total power were the same for the Gaussian and the rectangular beam profile. No attention was paid to atomic trajectories or non-stationary contributions of the density matrix, either. Although for typical beam diameters of $d = 0.7\,\mathrm{cm}$ and thermal velocities the estimated average interaction time of $\tau_{\mathrm{int}} \approx 35\,\mu\mathrm{s}$ is much longer than the natural lifetime $\tau \approx 30\,\mathrm{ns}$ of the excited state, this simplification does not necessarily yield a complete description of the phenomena observed. For instance, in a configuration where time-of-flight effects are not negligible, i.e., small laser beam diameter and low intensity, it is not obvious, to what extent stationary solutions are still adequate. In fact, THOMAS *et al.* [THO80] predicted a characteristic change in CPT line shape in the limit where the dark resonance linewidth is completely dominated by time-of-flight broadening. For some extreme choice of experimental parameters this effect could actually be observed in the experiments presented in chapter 5.2.2. But for all the other experimental investigations the conditions were such that time-of-flight effects could well be neglected. Finally, no attention was paid to propagation dynamics along the laser beam path through the cell. Although propagation effects under the influence of coherent population trapping can exhibit a number of other phenomena as discussed, e.g., in [GRO94], those were neglected here because of considerably lower optical densities.

Buffer gas For low intensity and small laser beam diameter time-of-flight broadening gives a large contribution towards the CPT linewidth. In order to reduce this influence a number of well-established techniques might be used that increase the effective interaction time between the atom and the light fields. The trivial method would consist in simply increasing the laser beam diameter which is of course not very handy for improvements of several orders of magnitude and would require rather high laser power to maintain intensity. Optical Ramsey excitation in an atomic beam is a well-known technique to overcome these difficulties, and linewidths of 1.3 kHz could be observed in a CPT experiment with 30 cm separation between the Ramsey zones [THO82].

But the observation of extremely small linewidths is by no means restricted to atomic beam experiments. In a gas cell of dilute cesium vapour depolarization of the atoms is mainly caused by wall collisions. Thus in optical pumping experiments various types of special wall coatings have been used for many years [HAP72]. The coatings usually consist of highly unpolarizable organic materials such as paraffin or polysilanes [SWE88] and the dominant effect is a reduction of the average dwell time of the atoms on the wall. In an uncoated cell the atoms do not directly

bounce off the walls but stick to the wall for time intervals during which polarization dependent interaction with the wall takes place. Hence a reduction of the average sticking time brings about a tremendous increase in the average number of wall collisions possible before the ground state coherence of the atom is destroyed. If the cell is fully illuminated by the laser beams this technique reduces time-of-flight broadening. For the experiments of this thesis a buffer gas technique was chosen, and adding several mbars of an inert buffer gas (here: neon) to the cesium vapour has two favourable effects:

First of all it efficiently reduces time-of-flight broadening because the free motion of cesium atoms through the interaction region is impeded by frequent collisions with buffer gas atoms. More details will be given in chapter 5.3, but the important points to note here are the following:

For typical buffer gas pressures of several tens of mbars ground state relaxation due to collisional cesium-neon interaction is still negligible. In contrast, strong broadening of the optical transitions is present even for buffer gas pressures as low as a few mbars. Experimentally, for the cesium-neon combination linewidths $\gamma_{\text{broadening}}$ and shifts γ_{shift} for the D_2 transitions were determined as

$$\begin{aligned} \gamma_{\text{broadening}} &\approx +8.6 \frac{\text{MHz}}{\text{mbar}} \cdot p_{\text{Ne}}\,[\text{mbar}] \quad \text{(FWHM)} \\ \gamma_{\text{shift}} &\approx -3.5 \frac{\text{MHz}}{\text{mbar}} \cdot p_{\text{Ne}}\,[\text{mbar}] \end{aligned} \tag{3.11}$$

(see [ALL82]). Hence for typical neon pressures the linewidth of the optical transition is of the same order of magnitude as both the excited state hyperfine splitting and the Doppler width. This will have important consequences for the multilevel model to be developed.

The second point about the buffer gas influence has to do with Doppler broadening directly. The Doppler effect at the laser difference frequency of 9.2 GHz still restricts the minimum linewidth obtainable in thermal vapour even in the limit of extremely large beam diameters when time-of-flight broadening is negligible.. Whereas a simple estimate of the Doppler width at a 9.2 GHz resonance frequency yielded about 9.9 kHz for cesium atoms at room temperature [SCH95], a more realistic approach indicates that the expected broadening effect might well be much lower. For instance, assuming negligible other broadening effects ($\gamma_{12} = \Gamma_{12} = 0$) and performing the Doppler integration for $\text{Im}(\rho_{32})$ according to eq. (2.13) the low-intensity limit yields dark resonance linewidths of several hundred Hz only. This is due to the fact that the contrast of the dark resonance decreases for increasing optical detuning. Hence the contribution of atoms exactly on resonance with the first laser appears with higher weight than the Doppler-shifted contributions such that on the whole Doppler broadening of the dark resonance remains below the simple estimate.

In the presence of the buffer gas, however, residual Doppler broadening is expected to be completely negligible due to Lamb-Dicke narrowing: If the mean free path λ_m of a radiation-emitting atom is much shorter than the radiation wavelength λ (in the so-called Lamb-Dicke regime), Doppler broadening gets suppressed [DIC53, VAN89]. In the case of the dark resonance the relevant wavelength is $\lambda = 3.26\,\text{cm}$ corresponding to the 9.2 GHz difference frequency whereas the

mean free path of cesium atoms in the presence of neon at room temperature can be gathered from the experimentally determined diffusion constant D_0 [BEV71] and the mean relative velocity between Cs and Ne atoms $\bar{v}$ as $\lambda_m = 3D/\bar{v} \approx 70\,\mu\text{m} \cdot \text{mbar}/p$. Accordingly, the Lamb-Dicke effect is expected to set in already at very low buffer gas pressure. This clearly constitutes an advantage with respect to the coated cell technique, because the need to reach the Lamb-Dicke regime would result in severe restrictions concerning the cell dimension. For further discussion see chapter 5.2.3.

Collisional relaxation In order to estimate the influence of various collisional processes on ground state relaxation one calculates the relaxation rate γ_{relax} from the corresponding cross section σ, the relative velocity $\bar{v}$ and the number density N as

$$\gamma_{\text{relax}} = N\bar{v}\sigma\,. \tag{3.12}$$

Whereas spin exchange and spin relaxation cross sections for cesium-neon collisions are of the order of $10^{-24}\,\text{cm}^2$ (see chapter 5.3.2 and [BEV71, WAL97]), those for collisions between cesium atoms at room temperature are reported as $\sigma_{\text{SE}} = (2.18 \pm 0.12) \cdot 10^{-14}\,\text{cm}^2$ for spin exchange [BEV71], and $\sigma_{\text{SR}} = 2.03 \cdot 10^{-16}\,\text{cm}^2$ for spin relaxation [BHA80]. For a cesium vapour pressure of $10^{-6}\,\text{mbar}$ this yields $\gamma_{\text{Cs-Cs}} \approx 6\,\text{Hz}$, which is negligible only in the absence of buffer gas. However, comparison with eq. (5.22) and fig. 5.20 shows that for intermediate buffer gas pressures $\gamma_{\text{Cs-Cs}}$ should contribute towards the dark resonance linewidth by more than 10 %. For further discussion see chapter 5.3.2.

3.2 Zeeman splitting

The application of an external magnetic field along a certain direction destroys the isotropy of the atomic system under consideration and thus the degeneracy with respect to the angular momentum z-components. As all of the external magnetic fields considered below are sufficiently weak and therefore do not affect the finestructure coupling one only has to consider the Hamiltonian H describing the atomic hyperfine structure interaction in the presence of an external magnetic field with flux density $\vec{B}$:

$$H_{\text{hfs}} = \frac{A}{2}\vec{I}\cdot\vec{J} + \frac{g_J\mu_B}{\hbar}\vec{J}\cdot\vec{B} + \frac{g_I\mu_B}{\hbar}\vec{I}\cdot\vec{B} \tag{3.13}$$

where for cesium $I = 7/2$, $A = h\Delta_{\text{hfs}}/(I+\frac{1}{2}) = h \cdot 9.192631770\,\text{GHz}/4$, $g_J = 2.0025402$, and $g_I = -0.39885395 \cdot 10^{-3}$ [WHI73]. For $F = I \pm 1/2$ the energies of the new eigenstates shift according to the Breit-Rabi formula:

$$E(\pm, m_F) = -\frac{A}{4} + m_F\mu_B g_I B \pm \frac{A(I+1/2)}{2}\sqrt{1 + \frac{4m_F}{2I+1}x + x^2} \tag{3.14}$$

where $x = (g_J - g_I)\mu_B B/A(I + 1/2)$, so that for cesium $x = 3.0496 \cdot B/\mathrm{T}$.

In all of the following the applied magnetic fields are assumed weak enough such that (F, m_F) practically remain good quantum numbers for both the ground and the excited states. Hence in total there are 16 non-degenerate ground state and 32 excited state levels involved in dark state preparation on the D_2 line and the simple concept of a three-level Λ-system is definitely no longer valid. In fact, the experiment shows that the dark resonance splits into several Zeeman components, both the number and the relative strength of which depend on light polarizations and magnetic field direction. Fig. 3.2(a) shows an example of a dark resonance split into seven Zeeman components (in a longitudinal field and with $\sigma^+\sigma^+$ laser polarizations). Fig. 3.2(b) illustrates the respective Zeeman levels and one-photon transitions involved where for simplicity only one set of excited states has been included. From the Breit-Rabi formula the position of the dark resonances can be derived as the frequency difference Δf between the two Zeeman levels involved:

$$\Delta f(m_3, m_4) = a(m_4 - m_3) + \frac{\Delta_{\mathrm{hfs}}}{2}\left(\sqrt{1 + \frac{m_4}{2}x + x^2} + \sqrt{1 + \frac{m_3}{2}x + x^2}\right) \tag{3.15}$$

where $a = g_I\mu_B B/h$, and m_F implies (F, m_F). In the linear Zeeman regime ($x \ll 1$) the dark resonance labelled $n = m_4 + m_3$ shifts with a rate

$$\xi = \frac{\mu_B}{8h}B\big(g_J(m_3 + m_4) + g_I(7m_4 - 9m_3)\big) \approx 3.51\,\mathrm{kHz}/\mu\mathrm{T} \cdot n\,. \tag{3.16}$$

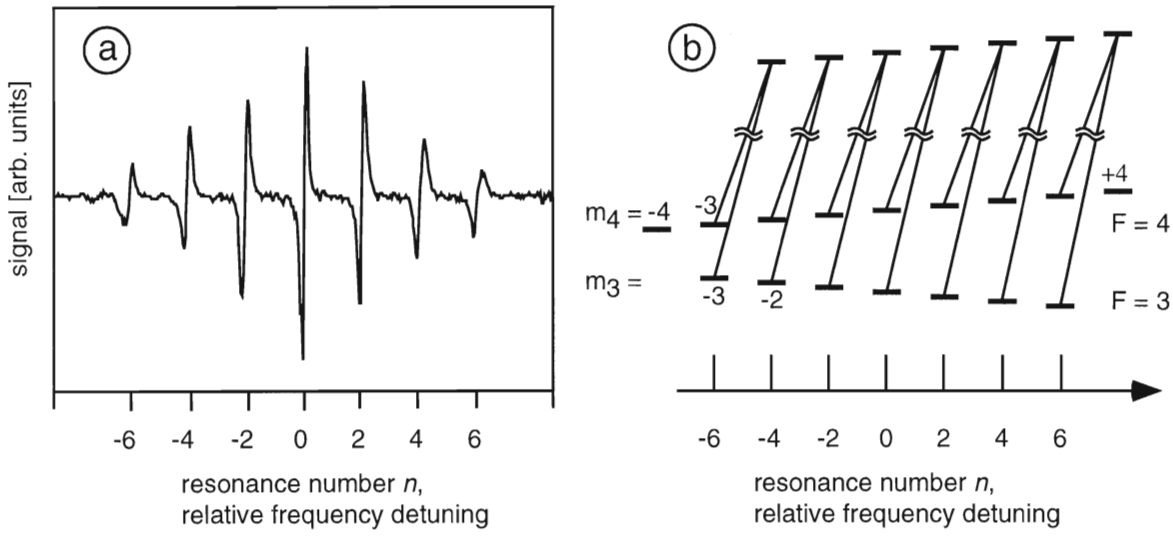

Figure 3.2: *Example of Zeeman split dark resonances in a longitudinal field ($\sigma^+\sigma^+$ laser polarizations). Both an experimentally recorded spectrum (a) (where the line shapes appear dispersive due to the lock-in technique used) and a sketch of the respective Zeeman levels involved (b) are shown, where for simplicity only one excited state multiplet is included.*

Hence the dominant contribution towards dark resonance Zeeman shifts can be characterized by n. With n fixed, the contributions for different possible values of $\Delta m = m_4 - m_3$ are

determined by laser polarizations and selection rules. Fig. 3.3 illustrates the coupling of pairs of Zeeman levels for equal n and $\Delta m = 0, \pm 2$. For dipole transitions with two photons involved the maximum value of Δm is 2. If it is assumed that dark states are prepared only between pairs of Zeeman levels the simplified situation depicted in fig. 3.3 together with eq. (3.15) would predict a dark resonance line (for fixed n) split into three components due to the purely nuclear contributions for different Δm (also see section 5.1.4). However, for arbitrary laser polarizations and magnetic field directions it is by far not obvious how various Zeeman levels are coupled for different Δm and what their final contribution towards the dark resonance measurement signal actually is. This will be the main concern of the next section.

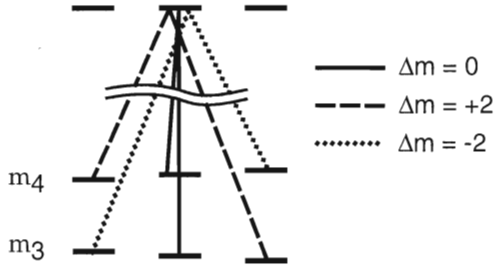

Figure 3.3: *Possible couplings between Zeeman levels for fixed* $n = m_4 + m_3$ *but different* $\Delta m = m_4 - m_3$

3.3 Multilevel theory of Zeeman-split CPT resonances

3.3.1 Basic ideas of the model

In principle the behaviour of a system consisting of a bichromatic light field interacting with a multilevel atom (48 levels in the case of the cesium D_2 transition) could be described completely by the corresponding density matrix equations. However, in the face of the number of levels involved the rather awkward determination of numerical solutions of such a system does not promise to yield considerable physical insight. Multilevel systems have been tackled by several authors, e.g., see [TAI96, KAN96, LIN96], and [ARI96A] for references. But usually the main concern of those authors is the theory of stationary states in degenerate multilevel systems, whereas the situation to be described here consists of a multilevel system whose degeneracy is partially lifted due to the presence of a small magnetic field. None of the contributions cited above yields a method to directly model the experimentally recorded variety of selection rules and line strengths attributed to the existence of a Zeeman multiplet of dark states. Therefore, a rather straightforward model has been developed the main concern of which was the understanding of geometry dependence in the experiment. Some of the underlying assumptions of the

model started off as hypotheses and did not result from rigorously proven theoretical considerations. However, detailed agreement with the experimental results strongly suggests the validity of the physically intuitive assumptions made.

The main idea of the model is to decompose the multilevel system into effective Λ-subsystems which are regarded as completely independent. Each subsystem consists of one Zeeman level from each of the two ground state F-multiplets such that $\Delta m \leq 2$, and any excited state which can simultaneously couple to both ground states. A particular example of such a decomposition is illustrated in fig. 3.4.

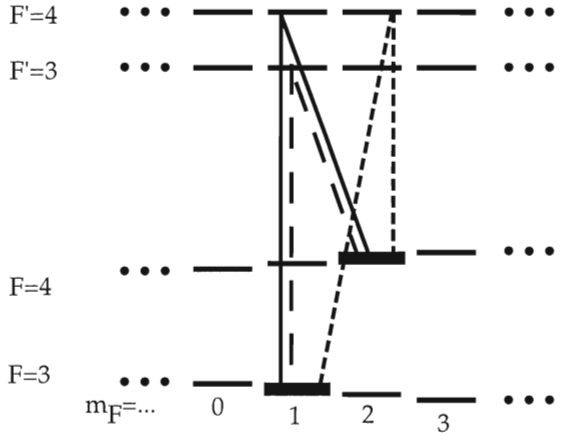

Figure 3.4: *Example for the decomposition of the multilevel system into a sum of 3-level systems. The pair of ground states ($|3, 1\rangle$, $|4, 2\rangle$) can be part of up to four 3-level subsystems, depending on which of the four excited states $|3, 1\rangle$, $|3, 2\rangle$, $|4, 1\rangle$, $|4, 2\rangle$ are coupled simultaneously to the pair of ground states ($|3, 1\rangle$, $|4, 2\rangle$). This is determined by the one-photon selection rules for the actual laser polarizations and magnetic field direction.*

For a given Raman detuning δ_R complying with the resonance condition imposed by the Breit-Rabi formula only resonant subsystems are considered. Even if there are several resonant subsystems which cannot be resolved due to homogeneous (e.g., saturation) and inhomogeneous broadening (e.g., due to field inhomogeneities) those are still treated independently. These assumptions might be characterized as the lowest-order contribution in a perturbation expansion with respect to the number of photons involved. In particular, this excludes Zeeman coherences induced by more than two photons. Furthermore, it is always assumed that the magnetic field, although strong enough to lift the Zeeman degeneracy, does leave (F, m_F) as good quantum numbers for all ground states. Together with the restriction to Raman resonance only, it follows that within the limits of the model no superposition states involving more than just one Zeeman level of the same multiplet have to be taken into account. Hence in this picture no interference effects arising from ground state levels shared among various effective Λ-subsystems have to be paid attention to. Then the relative strength of any Zeeman component in the dark resonance spectrum reflects the relative strength of the corresponding resonant Λ-subsystem. Presuming equal population in all ground state Zeeman levels (for optical pumping see section 5.7) the rel-

ative strength of a Λ-subsystem is given by the coupling strength for the stimulated two-photon transition between the two ground state Zeeman levels $|F_i, m_i\rangle$, $|F_f, m_f\rangle$ involved. In the lowest-order approximation this coupling strength is calculated as the square of the transition amplitude $A_\Lambda(m_i, m_f)$ in second order perturbation theory, which naturally implies a summation over all polarizations present in the light field and all possible excited state contributions:

$$S_{\mathrm{rel}}(m_i, m_f) = |A_\Lambda(m_i, m_f)|^2 \propto |\langle \psi_f\, F_f\, m_f | \mathcal{O}_\Lambda | \psi_i\, F_i\, m_i \rangle|^2 , \tag{3.17}$$

where ψ is a shorthand for all other quantum numbers characterizing the respective atomic state. The effective two-photon operator $\mathcal{O}_\Lambda$ describes a process where one photon is absorbed from one of the light beams and a second one emitted into the other light beam. For low enough laser power any saturation and optical pumping effects are neglected such that absolute laser intensities affect all Λ-subsystems in the same way and can be omitted as mere proportionality factors.

Under these assumptions the maximum number of dark resonance Zeeman components can be inferred from eq. (3.15). If the experimental resolution is not high enough to resolve contributions which only differ in their nuclear spin dependence (as it might be the case, e.g., for the system shown in fig. 3.3) the coupling strengths for the respective pairs of ground state Zeeman levels have to be added.

Before going into any details of the calculation some of the underlying assumptions have to be discussed.

1. In order for the coupling strengths to be the crucial parameters any Zeeman optical pumping has to be negligible so that all populations are equal at first. For low enough intensities this condition is well fulfilled, as it will be demonstrated from the detailed agreement of the model with the experimental results. Optical pumping itself was not investigated in detail, but a few considerations are given in section 5.7.

2. As the $F' = 2$ and $F' = 5$ excited states cannot contribute towards dark state preparation their presence can be viewed as loss channels out of the dark states via resonant one-photon absorption. Since the coupling strengths for these transitions depend on m_F the steady state population balance between various dark states might be expected to change. Recently, it was found theoretically that population losses and transit-time effects in a multilevel system considerably influence the dark resonance linewidth and contrast [Ren98]. But the regime under study was completely different from the situation encountered here because the authors assumed degenerate ground states and high intensities (several times the optical saturation intensity) such that optical pumping between Zeeman sublevels was dominant. In contrast, the experiments described in chapter 5 show that for the low intensities used this depopulation pumping can be neglected. Therefore this effect is completely ignored here.

3. As explained in detail in [COH92] dark state preparation can also be viewed as an interference effect between different channels of scattering events all transferring an atom from an initial state $|i\rangle$ to a final state $|f\rangle$. Hence in the unsaturated case it appears quite natural to characterize dark resonances by their respective coupling strengths. Furthermore, experimental evidence is given that the contrast of the dark resonance increases with intensity, i.e., Rabi frequency [ARI96A]. Since the latter also contains the transition matrix elements between the levels involved the above assumption again appears reasonable. However, although it has not been possible to rigorously prove the validity of this assumption, very good agreement with the experimental results seems to justify it.

3.3.2 Transition strengths

In all of the following the quantization axis will be chosen along the magnetic field direction. Accordingly, in order to account for a rotation of the field direction one has to transform the laser polarizations into the new reference frame. $|\psi F m_F\rangle$ is chosen as a suitable basis, where $|\psi\rangle$ denotes $|\tilde{n}LSJ\rangle$ with the principle quantum number $\tilde{n}$ while L, S, J are those of the orbital, spin, and total electronic angular momentum.

In second order perturbation theory with all non-resonant processes neglected the two-photon transition amplitude between an initial state $|i\rangle$ and a final state $|f\rangle$ can be derived as [LOU83]:

$$A_\Lambda \propto \sum_s \frac{\langle f|\,\vec{d}\cdot\vec{E}_2^*\,|s\rangle\,\langle s|\,\vec{d}\cdot\vec{E}_1\,|i\rangle}{\omega_1 - \omega_{si} + 2\pi i\gamma_s/2}\,. \tag{3.18}$$

Here $\vec{d} = -e\vec{r}$ is the electric dipole operator, $\vec{r}$ the position vector of the valence electron, $|s\rangle$ are all possible intermediate excited states, ω_1 is the frequency of the light field $\vec{E}_1$, ω_{si} the frequency difference between states $|s\rangle$ and $|i\rangle$, and γ_s the decay rate of state $|s\rangle$. Hence, for the cesium D_2 transitions this reads: $|i\rangle = |6S_{1/2}, F = 4, m_4\rangle$, $|f\rangle = |6S_{1/2}, F = 3, m_3\rangle$, and $|s\rangle = |6P_{3/2}, F_s, m_s\rangle$.

Since the components of any cartesian vector can uniquely be identified with the components of a spherical tensor of rank 1 it is most convenient to directly express all vectors in the spherical tensor basis $\{e_1, e_0, e_{-1}\}$. This will greatly simplify the calculations exploiting symmetry relations and tensor algebra.

The position vector $\vec{r}$ can be decomposed into its components r_1, r_{-1}, r_0, where the former two correspond to circular polarizations for the light propagation direction along the quantization axis, and the latter to linear polarization along this z-axis. With the spherical tensor components

a_p, b_q of the two light fields $\vec{E}_1$, $\vec{E}_2^*$, eq. (3.18) can be written as

$$\begin{aligned} A_\Lambda &\propto \sum_s \sum_{p,q} (-1)^{p+q} a_{-p} b_{-q} \frac{\langle f| r_p |s\rangle \langle s| r_q |i\rangle}{\omega_1 - \omega_{si} + 2\pi i \gamma_s/2} \\ &\propto \sum_{K=0}^{2} \sum_{Q=-K}^{K} (-1)^Q a_{-Q}^{(K)} \langle f| R_Q^{(K)} |i\rangle \\ &\propto \langle f| \mathcal{O}_\Lambda |i\rangle , \end{aligned} \tag{3.19}$$

where $\mathcal{O}_\Lambda$ is the effective two-photon operator and

$$a_Q^{(K)} = \sum_{p,q} \langle 1\, p\, 1\, q | K\, Q\rangle a_p b_q \tag{3.20}$$

$$R_Q^{(K)} = \sum_s \sum_{p,q} \langle 1\, p\, 1\, q | K\, Q\rangle \, r_p |s\rangle \langle s| r_q \, / N(\psi, F_s) \tag{3.21}$$

$$N(\psi, F_s) = \omega_1 - \omega_{si} + 2\pi i \gamma_s/2 \, . \tag{3.22}$$

For a detailed derivation see [WYN98B, WYN99A]. Application of the Wigner-Eckart theorem to $\langle f| R_Q^{(K)} |i\rangle$ allows to split off the Q dependence:

$$A_\Lambda \propto (-1)^{F_f - m_f} \sum_{K,Q} (-1)^Q a_{-Q}^{(K)} \begin{pmatrix} F_f & K & F_i \\ -m_f & Q & m_i \end{pmatrix} \mathcal{M}^{(K)} . \tag{3.23}$$

The important point to note here is that A_Λ has been decomposed into purely geometry-dependent contributions $a_Q^{(K)}$ and the $3j$-symbol on the one hand and on the other hand the geometry-independent term $\mathcal{M}^{(K)}$ containing atomic properties only. Hence any change in geometry can be accounted for by a rotation of the polarization tensor whereas all the remaining formula remains the same. This applies not only to polarizations but also to changes of the magnetic field direction. If an external magnetic field is not along the laser propagation direction $\hat{e}_z$, all one has to do is to transform the input polarizations into a coordinate system with $\hat{e}_{z'}$ along $\vec{B}$. By definition, for spherical tensors this is effected by the rotation matrices $D_{Q\,Q'}^{(K)}$:

$$\tilde{a}_{Q'}^{(K)} = \sum_Q a_Q^{(K)} D_{Q\,Q'}^{(K)} \, . \tag{3.24}$$

Since the product state of two tensors of rank 1, as given by the two photons, can be decomposed into irreducible tensor contributions of rank $K = 0, 1, 2$, there are only those multipolarities to be found in the above expression. Furthermore, scalar coupling ($K = 0$) is not possible between two states of different angular momentum $F_f \neq F_i$, as it is the case here. Therefore in principle only vector ($K = 1$) and quadrupole ($K = 2$) coupling can contribute such that for a given pair of initial and final states (m_i, m_f) the transition amplitude reads (the $3j$-symbol vanishes unless

$Q = m_f - m_i$):

$$A_\Lambda \propto \left[a^{(1)}_{m_i - m_f} \begin{pmatrix} F_f & 1 & F_i \\ -m_f & m_f - m_i & m_i \end{pmatrix} \mathcal{M}^{(1)} + a^{(2)}_{m_i - m_f} \begin{pmatrix} F_f & 2 & F_i \\ -m_f & m_f - m_i & m_i \end{pmatrix} \mathcal{M}^{(2)} \right] . \tag{3.25}$$

This tensor decomposition was done on the analogy of the treatment of two-photon absorption by CAGNAC *et al.* [CAG73] for $\omega_1 = \omega_2$, HERRMANN *et al.* [HER86] for $\omega_1 \neq \omega_2$, BONIN AND MCILRATH [BON84] for the study of selection rules for two-photon absorption. YURATICH AND HANNA [YUR76] found a general expression for multiphoton processes of arbitrary order, based on symmetry arguments, and discussed Raman transitions as a special case.

Finally, the multipole amplitude $\mathcal{M}^{(K)}$ can be calculated as

$$\mathcal{M}^{(K)} = (-1)^{F_i - F_f + K} \sqrt{2K+1} \times \sum_{\psi, F_s} (-1)^{2F_s} \begin{Bmatrix} F_f & K & F_i \\ 1 & F_s & 1 \end{Bmatrix} \langle F_f || r || F_s \rangle \langle F_s || r || F_i \rangle / N(\psi, F_s) . \tag{3.26}$$

While details of the derivation of $\mathcal{M}^{(K)}$ are again given in [WYN98A, WYN98B, WYN99A] it is important to discuss the treatment of the intermediate excited states in more detail.

The simplicity of the above formulae mainly results from the approximation of Zeeman degeneracy in the excited state. In eq. (3.19) the energy of the Zeeman levels only enters via the energy denominator $N(\psi, F_s) = \omega_1 - \omega_{si} + 2\pi i \gamma_s / 2$ where it gives a negligible contribution as long as the Zeeman splitting is small with respect to the excited state relaxation rate γ_s. Even in the case without buffer gas this is a very good approximation since in the experiments Zeeman shifts were usually of the order of several tens of kHz whereas $\gamma_s \approx 5\,\text{MHz}$. Therefore in the calculation of $\mathcal{M}^{(K)}$ the summation over the excited state z-components basically reduces to a sum over products of $3j$-symbols which greatly simplifies the formulae.

In contrast, the summation over the excited state F-components offers a straightforward method to account for the influence of an additional buffer gas. $\mathcal{M}^{(K)}$ can be written as the product of a term $\mathcal{V}(K, F_s)$ depending on the total angular momentum quantum number F_s of the excited state and a term $\mathcal{U}(K)$ containing F_s-independent terms only:

$$\mathcal{M}^{(K)} = \mathcal{U}(K) \sum_{\psi, F_s} \mathcal{V}(K, F_s) \tag{3.27}$$

with

$$\begin{aligned}
\mathcal{U}(K) &= (-1)^{I+L_f+S_f+J_s+L_s+S_s}(2J_s+1)\sqrt{(2K+1)} \\
&\quad \times\sqrt{(2F_f+1)(2F_i+1)(2J_f+1)(2J_i+1)} \\
&\quad \times \begin{Bmatrix} L_f & J_f & S_f \\ J_s & L_s & 1 \end{Bmatrix} \begin{Bmatrix} L_s & J_s & S_s \\ J_i & L_i & 1 \end{Bmatrix} \langle L_f||r||L_s\rangle\langle L_s||r||L_i\rangle \qquad (3.28) \\
\mathcal{V}(K,F_s) &= (-1)^{F_i+F_s+F_f+I+J_i+J_s+J_f+K} \\
&\quad \times \begin{Bmatrix} F_f & F_s & 1 \\ 1 & K & F_i \end{Bmatrix} \begin{Bmatrix} I & F_s & J_s \\ 1 & J_f & F_f \end{Bmatrix} \\
&\quad \times \begin{Bmatrix} F_i & F_s & 1 \\ J_s & J_i & I \end{Bmatrix} \frac{1}{N(\psi,F_s)} \\
&= \mathcal{W}(K,F_s)\,/N(\psi,F_s)\,. \qquad (3.29)
\end{aligned}$$

As discussed in chapter 5.5 the contrast of the dark resonance is strongly reduced if the optical detuning becomes comparable to the excited state relaxation rate. In this respect the situations encountered in vapour cells with or without buffer gas are crucially different. In a pure cesium vapour cell at room temperature the Doppler width of the D_2 line is 370 MHz which is comparable to the hyperfine splittings in the $6P_{3/2}$ state but considerably larger than the natural linewidth $\gamma_s \approx 5\,\mathrm{MHz}$ (Fig. 3.1). Hence for laser frequencies within the Doppler-broadened absorption profile two different velocity classes are resonant with the transitions $|i\rangle \rightarrow |s\rangle$ for $F_s = 3$ and for $F_s = 4$. These classes give the dominant contribution of level F_s to the dark resonance line strength. For each individual atom only one F_s-level will effectively enter into S_{rel} because the states $|s\rangle$ have a frequency difference much larger than γ_s. So instead of a summation over all excited states for each atom one has to sum over all atoms which independently interact with either the $F_s = 3$ or the $F_s = 4$ excited state.

In the presence of a buffer gas, however, γ_s can be of the same order or even much larger than the hyperfine splittings. Thus for each atom both F_s levels must be included into the summation over excited states. Therefore, apart from using the appropriate value of γ_s, the model accounts for the buffer gas by performing the summation over all possible excited states for transition *rates* (no buffer gas):

$$S_{\mathrm{rel}}^{\text{no buffer gas}} \propto \sum_{F_s} \left| \sum_{K,Q} (-1)^Q a_{-Q}^{(K)} \begin{pmatrix} F_f & K & F_i \\ -m_f & Q & m_i \end{pmatrix} \times \mathcal{U}(K)\mathcal{V}(K,F_s) \right|^2 \qquad (3.30)$$

or transition *amplitudes* (for sufficiently high buffer gas pressure):

$$S_{\mathrm{rel}}^{\text{buffer gas}} \propto \left| \sum_{F_s} \sum_{K,Q} (-1)^Q a_{-Q}^{(K)} \begin{pmatrix} F_f & K & F_i \\ -m_f & Q & m_i \end{pmatrix} \times \mathcal{U}(K)\mathcal{V}(K,F_s) \right|^2 . \qquad (3.31)$$

When the summation is over amplitudes (eq. (3.31)), interference effects can play an important role. In fact, the model shows that at sufficiently high buffer gas pressure, i.e., large γ_s, the

$K = 2$ contributions cancel: in a buffer gas no quadrupole coupling is possible. This can be seen in the following way: With $\delta_i = \omega_1 - \omega_{si}(F_s = F_i)$ and $\delta_f = \omega_1 - \omega_{si}(F_s = F_f)$ the summation over the two possible values of F_s can be written as

$$\sum_{F_s} \mathcal{V}(K, F_s) \approx \mathcal{W}(K, F_i) \cdot \frac{\delta_i - i\gamma_s/2}{\delta_i^2 + \gamma_s^2/4} + \mathcal{W}(K, F_f) \cdot \frac{\delta_f - i\gamma_s/2}{\delta_f^2 + \gamma_s^2/4} \,. \tag{3.32}$$

For large γ_s the terms δ_i^2 and δ_f^2 in the denominators quickly become negligible:

$$\sum_{F_s} \mathcal{V}(K, F_s) = \frac{4}{\gamma_s^2}\left[\delta_i \mathcal{W}(K, F_i) + \delta_f \mathcal{W}(K, F_f)\right] - i\frac{2}{\gamma_s}\left[\mathcal{W}(K, F_i) + \mathcal{W}(K, F_f)\right] \,. \tag{3.33}$$

After some angular momentum algebra one finds that the imaginary part vanishes for $K = 2$ (for details see [WYN98B]) so that the transition amplitude scales like γ_s^{-2} and the line strength like γ_s^{-4}. In contrast, for $K = 1$ the imaginary part does not vanish but in general dominates because of its γ_s^{-1} dependence for the amplitude and γ_s^{-2} for the rate. Therefore the $K = 2$ contribution to the transition amplitude decreases with increasing γ_s and becomes negligible, for example, above a few tens of mbar of neon in cesium vapour. A similar argument was given by HAPPER AND MATHUR [HAP67] for the case of one-photon optical pumping of atoms with an excited state hyperfine splitting smaller than the Doppler broadening.

In the high buffer gas limit, i.e., if the dominant contribution towards the resonance denominator $N(\psi, F_s)$ stems from γ_s, N becomes effectively independent of F_s and can be omitted as an overall proportionality factor. Then the expression for $\sum_{\psi,F_s} \mathcal{V}(K, F_s)$ in eq. (3.27) can be evaluated analytically to give:

$$\sum_{F_s} \mathcal{V}(K, F_s) = \begin{Bmatrix} J_i & K & J_f \\ F_f & I & F_i \end{Bmatrix} \begin{Bmatrix} J_i & K & J_f \\ 1 & J_s & 1 \end{Bmatrix} \cdot \frac{1}{N(\psi)} . \tag{3.34}$$

The limit of high buffer gas pressure can also be understood from a slightly different point of view. If the excited state hyperfine structure is almost completely disturbed by collisions between cesium and buffer gas atoms F is obviously not a good quantum number any more. Hence the excited state under consideration here is simply $|6P_{3/2}\rangle$. Starting from eq. (3.19) the coupling strengths between the pairs of ground state levels $(|i\rangle, |f\rangle)$ can be calculated in the same manner as before except for the actual formulae for the intermediate excited states. Instead of using excited states $|s\rangle = |nLSJFm_F\rangle$ now these states must be labeled $|s\rangle = |nLSIJm_Im_J\rangle$. As (F, m_F) is still treated as a good quantum number in the ground state it is convenient to choose the (F, m_F) basis for all states. Hence the excited state reads:

$$|s\rangle = \sum_{F_s, m_s} \langle F_s m_s |\, I\, m_I\, J\, m_J \,\rangle\, |F_s m_s\rangle \,. \tag{3.35}$$

The relevant part $\langle j|\, \widetilde{R}_Q^K\, |i\rangle$ of the transition matrix element $\langle j|\, R_Q^K\, |i\rangle$ containing the atomic quantities is given by:

$$\langle j|\, \widetilde{R}_Q^K\, |i\rangle = \sum_s \langle f|\, r_p\, |s\rangle\, \langle s|\, r_q\, |i\rangle\, \frac{1}{N(s, \psi)} \tag{3.36}$$

which in the case of high buffer gas pressure gave:

$$\langle j|\,\widetilde{R}_Q^K\,|i\rangle = \frac{1}{N(\psi)} \sum_{F_s,m_s} \langle F_f m_f|\,r_p\,|F_s m_s\rangle\,\langle F_s m_s|\,r_q\,|F_i m_i\,.\rangle \tag{3.37}$$

On the other hand, under the assumption that $N(\psi)$ is independent of m_I, m_J, inserting the expression for the excited state $P_{3/2}$ into eq. (3.36) and exploiting the closure relation for the Clebsch-Gordan coefficients yields:

$$\begin{aligned}
\langle j|\,\widetilde{R}_Q^K\,|i\rangle &= \sum_{m_I,m_J} \sum_{F_s,m_s} \sum_{F_s',m_s'} \langle F_f m_f|\,r_p\,|F_s m_s\rangle\,\langle F_s' m_s'|\,r_q\,|F_i m_i\rangle \\
&\quad \times \langle I\ m_I\ J\ m_J \mid F_s\ m_s\rangle\,\langle I\ m_I\ J\ m_J \mid F_s'\ m_s'\rangle\,\frac{1}{N(\psi)} \\
&= \sum_{F_s,m_s} \sum_{F_s'} \langle F_f m_f|\,r_p\,|F_s m_s\rangle\,\langle F_s' m_s|\,r_q\,|F_i m_i\rangle\,\frac{1}{N(\psi)} \\
&\quad \times \sum_{m_I,m_J} \langle I\ m_I\ J\ m_J \mid F_s\ m_s\rangle\,\langle I\ m_I\ J\ m_J \mid F_s'\ m_s\rangle \\
&= \frac{1}{N(\psi)} \sum_{F_s,m_s} \langle F_f m_f|\,r_p\,|F_s m_s\rangle\,\langle F_s m_s|\,r_q\,|F_i m_i\rangle
\end{aligned} \tag{3.38}$$

which is identical to eq. (3.37). Of course this is what must be expected since in both cases the summation over excited states only involves atomic properties without any other parameter being dependent on the summation index. Hence after performing the sum the result must be independent of these states.

3.4 AC-Stark shift

3.4.1 AC-Stark shift in pure cesium vapour

In the low intensity limit it is sufficient for many purposes to treat the atom-light field interaction as if the light field simply probed the unperturbed atomic transitions. However, for a more detailed description one has to consider the new eigenstates of the complete atom-field interaction Hamiltonian (dressed atom approach) such that the energies of the formerly unperturbed atomic levels are shifted (AC-Stark shift or light shift) where the shift depends on both light intensity and detuning.

In the case of the dark resonance the concept of an AC-Stark shift might appear paradox since the dark state does not couple to the light fields and thus cannot be perturbed. However, the model leading to equation (2.6) is far too simple because it does not include relaxation. A more careful analysis shows that the 'darkness' of coherent population trapping crucially depends

on relaxation. The description of coherent population trapping in the coupled/noncoupled state basis gives a rather straightforward explanation of this phenomenon because after suitable simplifications the population in these two states is coupled by the dephasing rate Γ_{12} [ARI96A].

In the model described in this work relaxations only enter via phenomenologically introduced decay rates for spontaneous emission, collisions etc. Other relaxation mechanisms become apparent from a quantum mechanical treatment of the light field. For instance, it has been found in a theoretical approach extending beyond the rotating wave approximation that the 'darkness' is fundamentally limited by four-photon processes resulting from the interaction with the vacuum field [GRI98].

The calculations described here for the treatment of AC-Stark shifts will also be compared with experimental results for saturation broadening and dark resonance line shapes in chapter 5.

The treatment of the AC-Stark shift closely follows the theoretical considerations developed so far. Since the multilevel model decomposing the total system into effective three-level systems produces excellent agreement with the experimental results it appears reasonable enough to continue with such a model. For experimental reasons it is convenient to only consider the $n = 0$ dark resonance component for $\sigma^+\sigma^+$ polarizations in a longitudinal magnetic field. Then the two relevant three-level systems to be taken into account are $(|S_{1/2}, F = 4, m_F = 0\rangle,\ |S_{1/2}, F = 3, m_F = 0\rangle,\ |P_{3/2}, F' = 3, m_{F'} = 1\rangle)$ and $(|S_{1/2}, F = 4, m_F = 0\rangle,\ |S_{1/2}, F = 3, m_F = 0\rangle,\ |P_{3/2}, F' = 4, m_{F'} = 1\rangle)$. According to section 3.3.2 it is possible to consider the two excited state contributions independently, i.e., to add the contributions of the two Λ-systems incoherently. The influence of the $P_{3/2}, F' = 2, 5$ excited states mainly consists in an additional contribution towards the ground state dephasing rate Γ_{12} via off-resonant one-photon absorption from the ground state. This is paid attention to in the model in that the value inserted for Γ_{12} corresponds to the experimentally found linewidth in the low intensity limit: $\Gamma_{12} = 2\pi \cdot 4.2\,\mathrm{kHz}$. Since Γ_{12} is an effective dephasing rate that comprises residual Doppler broadening at 9.2 GHz, time-of-flight broadening etc., nothing is really known about the ratio Γ_{12}/γ_{12}.

From eq. (3.10) one numerically calculates the Doppler-integrated dark resonance line profiles $n''(F' = 3)$, $n''(F' = 4)$ for the two Λ-systems. With respect to the presence of two excited states the optical detuning $\tilde{\delta_L}$ will be defined as the detuning of the laser frequency from the $3, 4$ cross-over transition in the following. Finally, the two resulting line shape contributions are added to produce the total signal n'':

$$n'' = n''(F' = 3, \delta_R, \tilde{\delta_L} + 100.75\,\mathrm{MHz}) + n''(F' = 4, \delta_R, \tilde{\delta_L} - 100.75\,\mathrm{MHz})\,. \tag{3.39}$$

The dark resonance position, defined as the minimum of this absorption profile, can then be determined numerically, both as a function of intensity and of the optical detuning. In order to compare the resulting dependencies with the experimental data it is essential to insert correct values for decay rates and Rabi frequencies taking into account angular momentum couplings. As derived in appendix D decay rates, with $\gamma_0 = \gamma_1 + \gamma_2 = 2\pi \cdot 5.3\mathrm{MHz}$, have to be scaled as

follows:

$$\begin{aligned} \gamma_1/\gamma_2 &= 7/5 \qquad \text{for } F' = 4 \\ \gamma_1/\gamma_2 &= 1/3 \qquad \text{for } F' = 3\,, \end{aligned} \tag{3.40}$$

whereas a similar treatment of the Rabi frequencies leads to

$$g_i^2 = (2F_i+1)(2F'+1) \begin{pmatrix} F' & 1 & F_i \\ -1 & 1 & 0 \end{pmatrix}^2 \begin{Bmatrix} J' & F' & 7/2 \\ F_i & J_i & 1 \end{Bmatrix}^2 G(I_i) \tag{3.41}$$

$$= W_i(F') \cdot G(I_i)\,, \tag{3.42}$$

with $G(I_i)$ as given in eq. D.7 and

$$W_1(F'=3) = 1/96,\ W_1(F'=4) = 7/96,\ W_2(F'=3) = 3/32,\ \text{and } W_2(F'=4) = 25/672\,. \tag{3.43}$$

3.4.2 AC-Stark shift in the presence of buffer gas

In order to model dark state preparation in the presence of buffer gas several additional aspects have to be considered. For typical buffer gas pressures collisional dephasing and relaxation mainly affect the optical transitions. But the influence of collisions between cesium and buffer gas atoms on dark state preparation goes beyond merely line broadening effects. The influence of velocity-changing collisions on the dark resonance was discussed by ARIMONDO [ARI96B]. Another important aspect is the complex interplay between the Doppler effect and line-narrowing due to the Lamb-Dicke effect. For direct microwave transitions and arbitrary buffer gas pressures this was examined by GALATRY [GAL61]. His approach is general enough to be applied to any process involving ground state coherences. Still, one cannot expect the dark resonance to exhibit the very same behaviour as the direct microwave transition because dark state preparation necessarily involves the optical transitions which are affected differently by buffer gas collisions. First of all, for typical buffer gas pressures the Lamb-Dicke regime is reached for the microwave transitions but not for the optical ones. Furthermore, according to [ARI96B] collisional broadening of the optical transitions also entails a reduced pumping rate into the dark state, hence decreased contrast of the CPT resonance. Since a detailed theoretical analysis taking all these aspects into account is not yet available, the main concern of this section is to find a simplified model which should be as independent as possible of a detailed description of the cesium-buffer gas interaction. Comparison with the experiment in section 5.2.3 will show to what extent the model is adequate.

Starting from the insight gained at the end of section 3.3.2, namely that in the limit of high buffer gas pressure the multilevel model is consistent with the assumption of a $P_{3/2}$ excited state, this idea should be pursued a bit further. Instead of calculating the incoherent sum of the two upper state contributions as in the preceding section one only has to evaluate the three-level

system consisting of the two ground states $|6S_{1/2}, F = 4, m_4\rangle$, $|6S_{1/2}, F = 3, m_3\rangle$ and the excited state $|6P_{3/2}, m_J\rangle$ with decay rates and Rabi frequencies adequately adjusted.

Choosing the $\{|F, m_F\rangle\}$ basis the excited state reads:

$$|P_{3/2} I' J' m_{I'} m_{J'}\rangle = \sum_{F', m_{F'}} \langle F' \; m_{F'} \mid I' \; J' \; m_{I'} \; m_{J'}\rangle \, |F', m_{F'}\rangle \,, \tag{3.44}$$

and taking into account that the dipole operator does not couple to the nuclear spin the Rabi frequencies can be calculated as:

$$g_i^2 = G(I_i) \cdot 0.1667 \,. \tag{3.45}$$

The decay rates simply scale with the degeneracy of the two ground state hyperfine components:

$$\frac{\gamma_1}{\gamma_2} = \frac{2F_1 + 1}{2F_2 + 1} = \frac{9}{7} \,, \tag{3.46}$$

and for a given buffer gas pressure the total decay rate $\gamma_0 = \gamma_1 + \gamma_2$ can be calculated from eq. (3.11). Since a detailed and thorough analysis of decay and dephasing rates on the optical transitions due to buffer gas collisions could not be found in the literature it is assumed that $\gamma_i = \Gamma_i$ for all collisionally broadened transitions.

Two different approaches, which might be considered as the two possible extremes, are used to treat Lamb-Dicke narrowing. On the one hand, dark resonance line shapes were calculated in that the effect was ignored completely:

$$n''(\delta_L, \delta_R) \mapsto \int f_D(v) n''(P_{3/2}, \delta_L - \omega_1 v/c, \delta_R - (\omega_2 - \omega_1)\frac{v}{c}) dv \,. \tag{3.47}$$

On the other hand, the Doppler shift of the frequency difference was ignored completely, i.e., eq. (3.9) was omitted and eq. (3.10) was replaced by:

$$n''(\delta_L, \delta_R) \mapsto \int f_D(v) n''(P_{3/2}, \delta_L - \omega_1 v/c, \delta_R) dv \,, \tag{3.48}$$

Note that in the case of high buffer gas pressure the optical detuning δ_L is again defined according to eq. (2.9) and fig. 2.1, where the excited state $|3\rangle$ is given by the centre of gravity of the excited state hyperfine multiplet which corresponds to the position of the $P_{3/2}$ state in the hypothetical absence of the hyperfine splitting.

4 Experimental realizations

4.1 Coherently coupled bichromatic fields

As discussed in chapter 2.1 the preparation of CPT resonances requires a coherent bichromatic light field. On the cesium D_2 line coherent coupling of light fields with a 9.2 GHz frequency separation has to be achieved, which is an experimentally non-trivial task. One might think of various methods to produce such a field: Modulation techniques might provide the most straightforward methods. Acousto-optical (AOM) or electro-optical modulators (EOM) inserted into the beam path of a single-frequency laser create frequency sidebands at the modulation frequency with fixed phase relation to the carrier. Omitting all but the two desired frequencies (e.g., with the help of the transmission through a Fabry-Perot interferometer or simply neglecting all other sidebands if they are off-resonant enough) one ends up with the coherent bichromatic field. Although AOMs are routinely used in experiments on sodium ($f_{\mathrm{mod}} = 1.77\,\mathrm{GHz}$, $\lambda = 589\,\mathrm{nm}$), e.g., for the demonstration of the application of CPT resonances as an atomic frequency standard [HEM83], for modulation frequencies as high as 9.2 GHz it is extremely hard to achieve sufficient modulation efficiency. Despite their availability at this modulation frequency the problem with EOMs mainly lies in the high r. f. driving power needed, which leads to thermal stability problems if constant modulation efficiency is required. Therefore, the only modulation technique actually employed here was a direct modulation of the laser injection current. In order to end up with sufficient power in the sidebands special laser diodes, so-called VCSEL (**V**ertical-**C**avity **S**urface-**E**mitting **L**asers), with high intrinsic modulation bandwidth had to be used. The respective experimental set-up will be presented in section 4.3.2.

The most versatile method, i.e., with complete freedom of choice concerning polarization, direction, diameter and intensity of the two frequency components, is to employ two independent lasers and electronically phase-lock them onto each other. The major part of the experimental results stems from measurements with phase-locked lasers, and the following section will be dedicated to the respective set-up.

4.2 Phase-locked diode lasers

4.2.1 Diode lasers

At a wavelength of 850 nm commercially available edge-emitting laser diodes based on AlGaAs structures provide narrowband and reliable sources of laser radiation and have become important tools for precision spectroscopy. The set-up used here basically follows the concepts reviewed in [WIE91, MAC92]. The extremely divergent laser beam emanating from a commercial laser diode

mounted in a SOT-148 package is collimated by an achromatic lens. Both optical and electrical feedback is used to tailor the laser output. Optical feedback from an external grating in Littrow configuration allowed to improve single-mode operation of the diode and to actively control the output frequency of the laser via the tilt angle of the grating. A standard temperature stabilization scheme was used where a Peltier element controlled by an electronic servo loop stabilized the diode temperature to within about 1 mK. The short-time stability of the laser frequency (i.e., for averaging times of about a second) of such a system lies in the range of several hundred kHz whereas over longer time intervals the system still shows frequency drifts and jumps due to external acoustic or thermal noise. Hence, in order to further increase the long-term stability of the laser another standard technique was employed in that the laser frequency was locked to an external reference frequency via a slow servo loop. This reference could be obtained from a simple absorption signal in an auxiliary Cs cell or from Doppler-free saturation spectroscopy resonances which provide an even steeper frequency discriminator. In both cases the servo loop controlled the tilt angle of the grating via a voltage applied to a piezo element.

4.2.2 Optical phase-lock

The general idea of phase-locking is the stabilization of the relative phase between a master and a slave oscillator via an electronic servo loop. Many details on implementation and techniques are given, e.g., in [GAR79]. Phase-locking for optical frequencies was first demonstrated more than 30 years ago [ENL65] and has found applications, for instance, in optical frequency multiplication chains [TEL90, PRE95]. The particular scheme employed here is sketched in fig. 4.1.

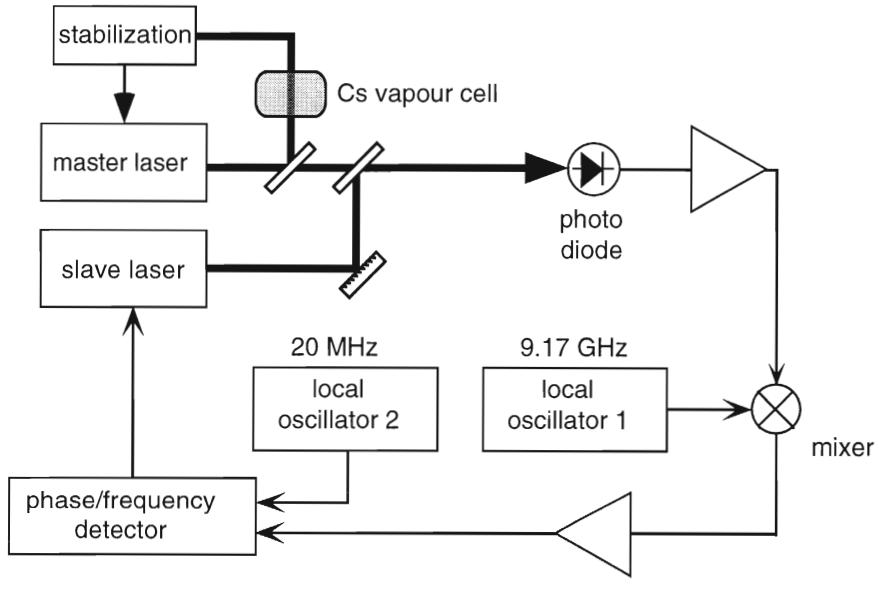

Figure 4.1: *Experimental set-up of the optical phase-lock at 9.2 GHz difference frequency*

The master laser is usually stabilized to an absorption signal of the transition involving the

$F = 4$ ground state hyperfine component. The injection current and grating tilt angle of the slave laser are chosen such that its frequency roughly corresponds to the Doppler-broadened transition from the $F = 3$ ground state, as monitored with the help of an auxiliary Cs cell. The two laser beams are superposed, and a certain fraction of the overall power is focused onto a fast photodiode (Antel Optronics AR-S2) which allows to detect the beat note at 9.2 GHz whereas higher frequency contributions are averaged out:

$$\begin{aligned} S_{9\mathrm{GHz}} &\propto \langle |E_1 \sin(\omega_1 t + \varphi_1(t)) + E_2 \sin(\omega_2 t + \varphi_2(t))|^2 \rangle_t \\ &\propto E_1 E_2 \cos(\Delta\omega t + \Delta\varphi(t)) \end{aligned} \tag{4.1}$$

with $\Delta\omega = \omega_2 - \omega_1$, $\Delta\varphi(t) = \varphi_1(t) - \varphi_2(t)$. After suitable amplification this signal is compared to a 9.172 GHz frequency from a stable reference source (the so-called first local oscillator LO1). In a second mixing stage the resulting signal at 20 MHz frequency

$$S_{20\mathrm{MHz}} \propto \sin((\Delta\omega - \omega_{LO1})t + \Delta\varphi(t) - \varphi_{LO1}) \tag{4.2}$$

is fed into a digital phase detector. This device compares the phase of the signal with that of yet another stable reference frequency at 20 MHz (LO2). Hence for $\Delta\omega - \omega_{LO1} - \omega_{LO2} = 0$ the error signal finally obtained is

$$S \propto \sin(\Delta\varphi(t) - (\varphi_{LO1} + \varphi_{LO2})) \tag{4.3}$$

which for small phase excursions is proportional to the excursion. In general, the second mixing stage could be performed by just another mixer simply providing an output signal proportional to the overall difference phase. But in that case phase excursions of more than $\pi/2$ would cause the servo loop to drop out of lock. Oscillation cycles would be lost until the loop relocks again, probably at a different phase due to the periodicity of the signal. The use of such an analogue phase detector has been proved possible but the loop was not stable enough, especially for grating stabilized diode lasers with rather broad linewidths. In contrast, the digital phase detector used here, whose design follows the set-up presented by PREVEDELLI *et al.* [PRE95], consists of digital counters keeping track of the number of oscillation cycles of both the beat signal and the second local oscillator. This allows the slave to remain locked without any cycle slips even for phase excursions as large as $\pm 31\pi$. Hence under realistic laboratory conditions a much more stable device results. Details on the particular implementation of the phase detector are given in [BRA96]. Finally, a passive loop filter provides an additional phase shift of the signal in order to compensate delays in the electronic circuitry and the phase of the laser's transfer function. In order not to diminish the loop bandwidth by a slow response of the slave laser the main portion of the error signal is applied directly to the laser via its injection current. Long-term drifts are compensated by a second, much slower loop where, after integration, the error signal is fed to the grating piezo element. Typically loop bandwidths of more than 2 MHz could thus be obtained.

Fig. 4.2 shows the beat note power spectral density of two phase-locked lasers from which the average residual phase excursion ϕ_{rms} can be determined. This phase excursion is related to the

relative power η contained in the carrier via $\eta = \exp(-\phi_{\mathrm{rms}}^2)$ [HAG79]. With $\eta = 99.4\%$ given by the relative area under the carrier a residual phase excursion of only $\phi_{\mathrm{rms}} = 4°$ results.

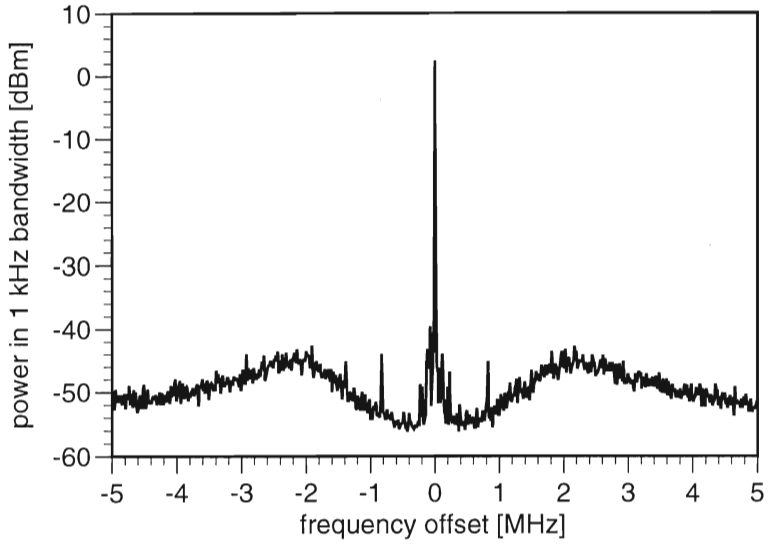

Figure 4.2: *Power spectral density of the 9.2 GHz beat note between phase-locked diode lasers. From the relative area under the central peak a residual phase excursion of about 4° was determined.*

To record a dark resonance spectrum the slave frequency was stepped across the resonance via the frequency of the second local oscillator. In order to exclude relative drifts between the reference frequencies all active frequency components were stabilized to the same 10 MHz reference frequency.

4.2.3 Experimental set-up

Fig. 4.3 sketches the set-up for the CPT experiments using phase-locked lasers. Faraday isolators with an extinction coefficient of 60 dB are used to eliminate unwanted feedback into the laser diodes. Perfect spatial mode matching of the two laser beams is not only needed for a good beat note independent of spatial variations over the area of the photodiode but also for the suppression of residual Doppler broadening of the dark resonance due to non-parallel alignment of the two laser beams. For slightly misaligned beams residual Doppler-broadening would broaden the line by several hundred kHz/mrad [SCH95]. Therefore a stretch of single-mode optical fibre serves as a mode filter for the bichromatic field. Of course, using this technique pointing instabilities of the laser beams, e.g., arising from thermal drifts or acoustic vibrations of the mirrors used throughout the whole set-up, translate into intensity fluctuations behind the fibre via fluctuations of the fibre coupling efficiency. Spatial mode matching on the fast photodiode is similarly affected by acoustic noise. In fact, the set-up showed considerable sensitivity not only to the draught of the air conditioning system and any movement in the room but also to low-voice speech. Accordingly, the stability of both the phase-locked loop and the intensity

behind the fibre could be increased enormously when the whole set-up was completely covered in a plastic film construction.

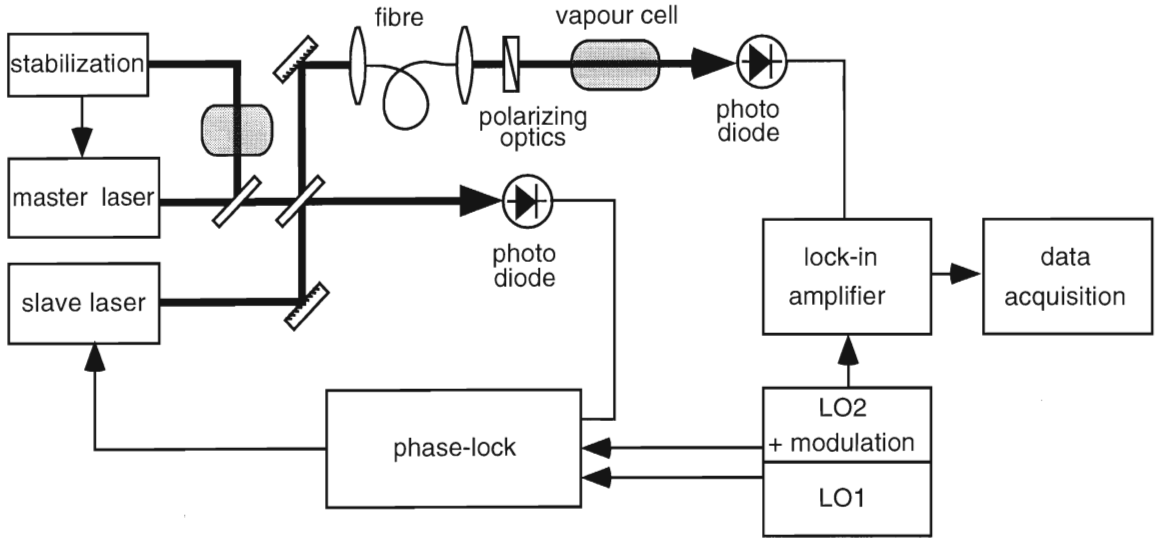

Figure 4.3: *Experimental set-up for dark state preparation in thermal cesium vapour with phase-locked lasers*

The use of a single-mode but non-polarization-preserving optical fibre allowed to independently control the polarizations of the two lasers by quarter- and half-wave plates inserted into the respective beam paths. However, for both polarizations chosen equal — as it was usually the case — the respective polarization optics was placed directly in front of the Cs cell in order to minimize depolarization effects of mirrors, attenuators etc. Furthermore, a two-lens telescope could be employed to change the beam diameter. The Cs cell itself was placed inside three mutually orthogonal current coils to compensate the geostatic magnetic field and to apply a field of controlled strength and direction. Finally, the actual measurement signal was the transmission signal behind the Cs cell as recorded by a photodiode. For precision magnetometry experiments the cell could be placed into a double layer μ-metal shielding with an estimated shielding factor of about 10^3. Some experiments required the application of particularly uniform fields. Thus a special arrangement of current coils was used, tailored in order to provide less than 0.1 % deviation over the interaction volume.

The Cs gas cells were cylindrical with typical diameters and lengths of 2 cm. A drop of metallic Cs inside the cell provided about $1.6 \cdot 10^{-6}$ mbar Cs vapour pressure at room temperature which is enough in order to obtain sufficient absorption signal without the need of further heating of the cell. For investigations of CPT properties as a function of buffer gas pressure special cells closed off by a vacuum tap could repeatedly be filled with different buffer gas pressures. Some sealed-off cells with a fixed amount of buffer gas were available as well.

Due to the thermal movement of the Cs atoms and the additional hyperfine components $F' = 2, 5$ in the excited state the strength of the dark resonance is relatively weak - as compared to the background of inhomogeneously broadened one-photon absorption. Thus, in order to increase

the signal-to-noise ratio for the dark resonance, frequency modulation techniques (FM) were employed [TAK75, BJO83, LEN84, GEH85]. The modulation signal, typically with a modulation frequency of 1 kHz and a phase modulation index of $M = 1$, was applied to the slave laser via the respective modulation of the 20 MHz reference frequency. Subsequently the transmission signal was demodulated in a lock-in amplifier. Since for diode lasers the linewidth enhancement factor α is different from zero, frequency modulation always entails a small modulation of the amplitude (AM) as well. A fit to the experimental data typically yielded an AM contribution of at most a few percent. For details on frequency modulation and line shape retrieval see appendix A. Another very handy feature of the frequency modulation technique is that the use of a dual-phase lock-in amplifier allows to determine both the absorption and the dispersion of the medium — at least up to a constant factor. Getting the complete information from a single transmission measurement is definitely much easier than, e.g., recording dispersion spectra in a balanced Mach-Zehnder interferometer [SCH95]. However, the latter method also yielded absolute values.

If not stated otherwise the frequency of the master laser was stabilized near the 3, 4 crossover resonance of the $F = 4$ transition whereas the slave laser was stepped across the resonance via computer control of the second local oscillator frequency. Both the in-phase and quadrature component of the spectra demodulated by the lock-in amplifier were recorded simultaneously.

4.3 Frequency-modulated laser

In order to employ direct laser injection current modulation with sufficient efficiency at 9.2 GHz, laser diodes with as high an intrinsic modulation bandwidth as possible have to be sought. Usually, efficient sideband creation is possible for frequencies up to the laser relaxation oscillation frequency which in the case of edge-emitting laser diodes usually is a few GHz. Despite this constraint injection current modulation at 4.6 GHz was shown to be efficient enough to use the first order sideband on either side of the carrier for a magneto-optical trap [MYA93] or a CPT experiment in a cesium atomic beam [HEM93]. Since optical feedback from an external cavity is used in most of the set-ups involving edge-emitting laser diodes the overall modulation efficiency could be enhanced considerably if the free spectral range of the external cavity was carefully matched to the desired modulation frequency [MYA93].

In principle such a set-up would be feasible for dark state preparation as well, nevertheless imposing a limit on the buffer gas pressure to be used: With both first order sidebands resonant with one of the hyperfine transitions each the strong carrier frequency, which typically contains more than 60 % of the total power, is detuned by 4.6 GHz from either resonance. For typical neon pressures of several tens of mbar pressure broadening of the optical linewidth reaches hundreds of MHz such that the carrier detuning corresponds to only a few homogeneous linewidths. Hence unwanted background absorption or interference with the sideband dark state preparation might well be present. Another aspect which does not speak in favour of the 4.6 GHz modulation

technique is that in some cases (e.g., in the configuration for precision magnetometry proposed by FLEISCHHAUER and SCULLY [FLE94]) higher total intensities are desired. For fixed modulation efficiency this would necessitate higher total power thus again increasing the possibly detrimental influence of the carrier. For these reasons, after having demonstrated the feasibility of dark state preparation with 4.6 GHz sidebands, only 9.2 GHz modulation techniques were employed here.

4.3.1 Vertical-cavity surface-emitting lasers (VCSEL)

Recent advances in semiconductor processing techniques have led to the development of the so-called VCSEL (**V**ertical-**C**avity **S**urface-**E**mitting **L**asers). Although mainly aimed at the telecommunications market the high modulation bandwidth of VCSELs also lends them to dark state preparation especially since they are available at the required wavelengths for both the cesium and rubidium D_2-lines.

The main feature of the VCSEL is its extremely short resonator. Whereas in conventional edge-emitting diodes the resonator length is typically a few hundred μm, it is only about $1 - 5\,\mu$m for the VCSEL. In order nevertheless to achieve photon densities high enough to facilitate laser operation the active region must be surrounded by high reflectivity mirrors that consist of distributed Bragg reflector layers with reflectivities higher than 99 %. The free spectral range of the extremely short optical resonator thus established is so large that typically only one longitudinal cavity mode lies within the gain profile of the medium. Hence the VCSEL intrinsically operates in a single longitudinal mode, without the need for external mode selection components [JUN97, CHA98]. Furthermore, high photon density in connection with a small active volume and small electrical capacity also leads to high modulation bandwidths which can even exceed 10 GHz [KIN98]. Fig. 4.4 compares a VCSEL structure with that of a conventional edge-emitting laser diode.

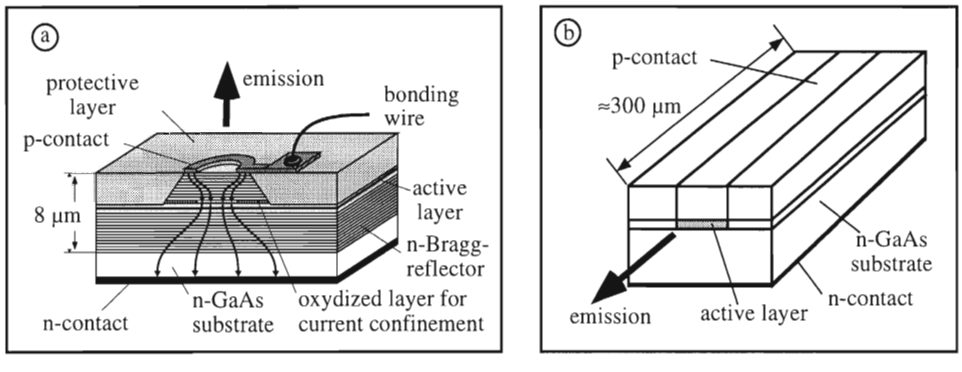

Figure 4.4: *Typical structures of (a) a VCSEL and (b) a conventional edge-emitting laser diode.*

As its name already suggests, the layer structure of the device is grown parallel to the wafer surface and the laser radiation is emitted through the top or bottom reflectors, i.e., perpendicularly to the wafer. Hence large arrays of VCSELs, one next to the other, can easily be

grown, integrated, tested and operated without the need to cleave the wafer. Apart from the mere ease of fabrication this opens up many opportunities for applications, e.g., in connection with fibre optics. Since the area from which the laser irradiation emanates can be made considerably larger than for edge-emitting type diodes the diffraction-limited beam divergence is typically smaller. Furthermore, the high reflectivity mirrors reduce the sensitivity of the VCSEL to spurious external optical feedback, although for practical purposes a Faraday isolator is still used.

The laser linewidth is typically of the order of a few tens of MHz which is roughly one order of magnitude larger than for edge-emitting diodes.

The VCSEL used in the experiments here was a prototype provided by the group of Prof. Ebeling from the University of Ulm. Its bottom Bragg reflector is made of 30.5 n-type silicon doped AlAs/$Al_{0.2}Ga_{0.8}As$ layer pairs. The central region is one wavelength thick and contains three 8 nm thick GaAs quantum wells embedded in $Al_{0.5}Ga_{0.5}As$ spacer layers in order to provide efficient carrier confinement. The p-type top Bragg reflector consists of 26 carbon doped $Al_{0.2}Ga_{0.8}As/Al_{0.9}Ga_{0.1}As$ layer pairs. An extra 30 nm AlAs layer, selectively oxidized for current confinement after wet chemical mesa etching [JAE97, JUN97], is inserted in the lowest top mirror layer. The oxidation procedure step not only reduces the threshold current but also helps to ensure single transverse mode operation.

4.3.2 Experimental set-up

The VCSEL was mounted in a brass housing with an SMA connector for the current supply. A bias-T was used to combine the DC current supply with the GHz modulation current. The output laser beam was shaped with the help of an achromatic collimating lens and temperature control of the VCSEL was accomplished similarly to the set-up described in section 4.2.1.

Exploiting both the temperature and injection current dependence the VCSEL wavelength could easily be tuned to the desired value. Again similarly to the conventional set-up the wavelength was determined from the transmission signal in an auxiliary cesium cell. A similar slow feedback loop was used to stabilize the VCSEL frequency to the Doppler-broadened transmission signal, in this case applying the error signal to the laser injection current.

Fixed output frequency necessitates higher injection current if the temperature is lowered, therefore the VCSEL output power available at the desired wavelength could be optimized in that the VCSEL was held at a temperature as low as possible. Since the laser diode housing was not air-tight, condensation of atmospheric humidity restricted the accessible temperature range to above 13° C. Varying the laser injection current at low frequencies via the DC current control allowed to easily scan the laser frequency over the two 9.2 GHz-split hyperfine components with a detuning rate estimated as 300 GHz/mA. In contrast, using the conventional set-up it was extremely difficult to scan the laser over such a large frequency range without mode-hops.

Hence the use of the VCSEL also opens up the possibility to easily study dark resonances for much larger optical detunings. The modulation bandwidth of the VCSEL used was typically specified as large as 10 GHz [KIN98] thus principally allowing very efficient creation of 9.2 GHz sidebands. However, considerable reduction of the overall modulation efficiency can arise from impedance mismatching in the VCSEL connections. As the VCSEL current is very low (about 2 mA) in comparison with the edge-emitting diodes used in the conventional set-up, the VCSEL frequency shows a much higher sensitivity to the ever present current noise component at the 50 Hz power line frequency. Comparison of the resulting frequency excursions with a Doppler-broadened cesium absorption line allowed to estimate its amplitude to about 50 MHz which is of the same order of magnitude as the fast intrinsic VCSEL linewidth. Recent modifications of the experimental set-up include the use of a battery-powered VCSEL supply thus reducing the slow laser frequency fluctuations to about 20 MHz. For a more detailed discussion see [AFF99].

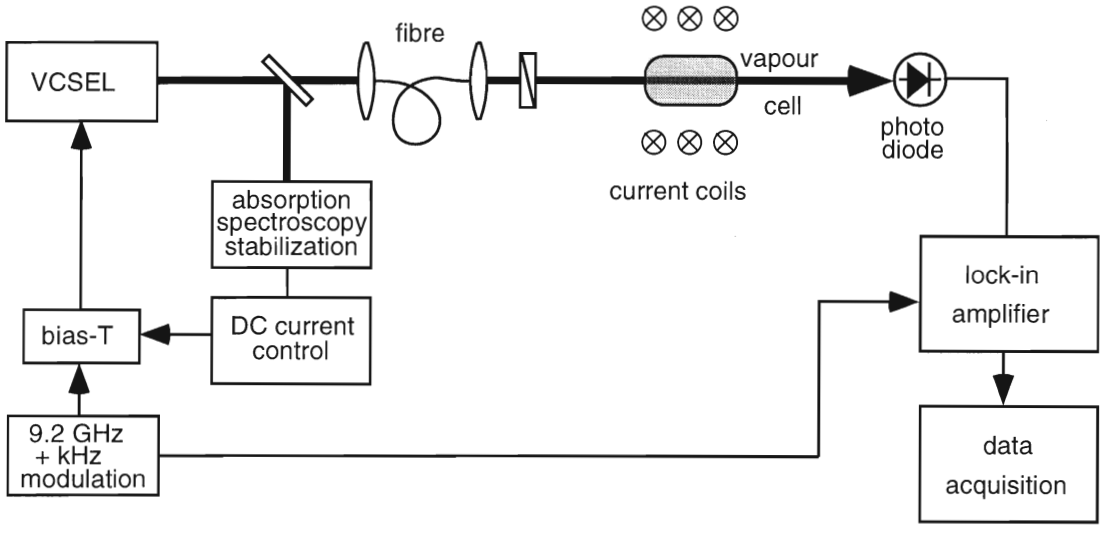

Figure 4.5: *Experimental set-up for the observation of dark resonances using a frequency-modulated VCSEL*

Fig. 4.5 sketches the set-up for the dark state experiment with a VCSEL which is both compact and mechanically robust, as compared with the set-up depicted in fig. 4.3. Normally one would refrain from the use of the optical fibre because modulations of the coupling efficiency due to mechanical vibrations of the optical components are translated into intensity fluctuations behind the fibre. Due to geometrical constraints the beam of the VCSEL prototype behind the collimating lens was not a pure TEM_{00} mode but showed some diffraction pattern. For dark state preparation this might lead to unwanted effects. In the case of an unbuffered cell the effective laser beam width as seen by the atom will be given by the width of one intensity fringe only thus increasing time-of-flight broadening even more. Since it is also rather difficult to give an estimate of the mean intensity without a detailed knowledge of the beam profile the single mode fibre was used as a mode filter for the laser beam. The resulting Gaussian laser profile had a diameter of 1.56 mm and typically a power of 40 μW available for the experiment. The corresponding maximum intensity of about 1 mW/cm^2 is comparable to the respective optical

two-level saturation intensity. If compared to the phase-lock set-up the lower total power of the VCSEL can lead to a poorer S/N ratio on the detector.

Frequency modulation spectroscopy with lock-in detection was employed as in the other experimental situation. This resulted in a double modulation technique where the VCSEL carrier frequency was modulated by the respective GHz frequency which was itself frequency-modulated in the kHz range. Details on the expected lock-in line shapes are given in appendix A. Usually the carrier frequency was stabilized to the $F = 4$ Doppler-broadened absorption spectrum from the auxiliary cesium cell and the +1st GHz modulation sideband was stepped across the dark resonance.

4.3.3 Characterization of the VCSEL

A more detailed characterization of the VCSEL is needed if this set-up is to be used for precision spectroscopy of CPT resonances. Subtle details of the dark resonance such as the AC-Stark shift and the line shape critically depend on both the total power and the relative powers of the bichromatic light field. Hence one has to scrutinize the modulation behaviour in the GHz range not only of the isolated VCSEL but of the whole set-up which could well be different because of impedance mismatching. The second point of interest is the linewidth of the VCSEL output which is expected to be much larger than for an edge-emitting laser diode.

VCSEL linewidth A standard method to measure a laser linewidth consists in self-heterodyne measurements [SCH96] where the coherence time is determined with the help of a sufficiently long delay line. However, another approach was followed here because of its experimental ease and availability: Saturation spectroscopy offers a rather simple method to obtain fairly narrow Doppler-free resonance lines where for low enough intensities the linewidth approaches the natural linewidth of the transition under investigation (which in the case of the cesium D_2 line is 5.3 MHz). If the linewidth of the atomic transition is considerably narrower than the bandwidth of the light source the minimum linewidth of the saturation spectra measured roughly corresponds to the latter.

In order to record saturation spectra with the VCSEL a standard saturation spectroscopy set-up as sketched in fig. 4.6 was used. A detailed account of saturation spectroscopy on the cesium D_2 line can be found, e.g., in [SCH94, SCH95]. Due to the large inherent bandwidth of the VCSEL it was not possible to resolve the double structure of the saturation dip denoted (c) in the experimental spectrum in fig. 4.7 where the two peaks are separated by only 26 MHz. Subtracting the Doppler background from the measured curves and fitting Lorentzian line shapes to the three most pronounced peaks yields a full width at half maximum $\Delta f_{\mathrm{exp}} = (55 \pm 4)$ MHz for each saturation peak [AFF99].

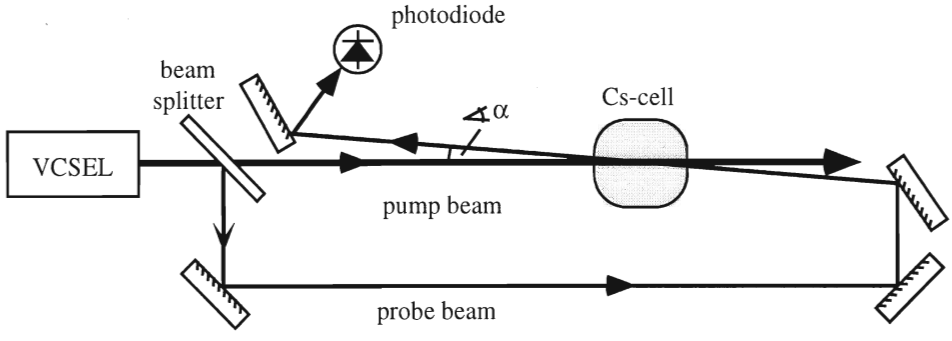

Figure 4.6: *Experimental set-up for saturation spectroscopy measurements using a VCSEL. The misalignment of the pump and probe beams is not to scale; the residual angle was about* 0.5°.

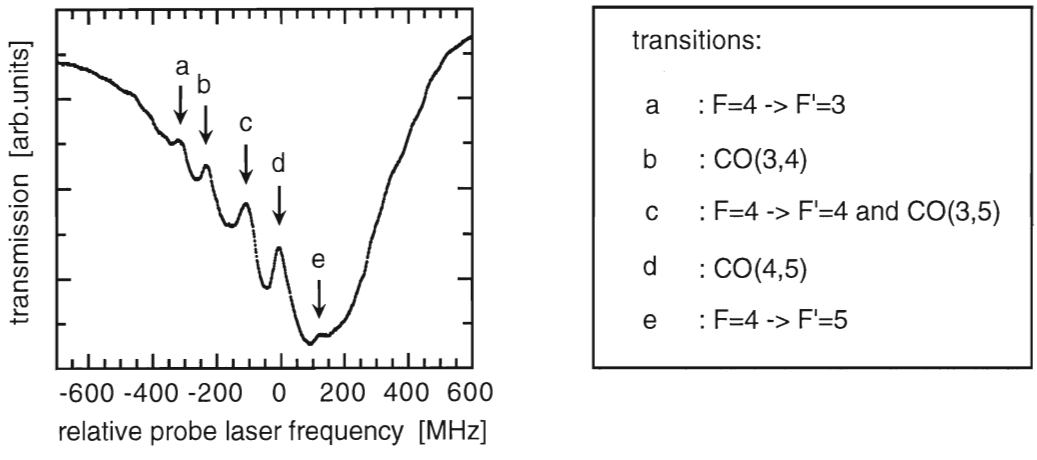

Figure 4.7: *Typical saturated absorption spectrum of the cesium* $6S_{1/2}, F = 4 \rightarrow P_{3/2}, F' = 3, 4, 5$ *transition obtained with a VCSEL. Due to the large inherent bandwidth of the VCSEL the two peaks in (c) spaced by only* 26 *MHz cannot be resolved.*

An analysis of broadening mechanisms described in [AFF99] shows that only residual Doppler-broadening from misalignment of the pump and probe beams and saturation broadening noticeably contributed towards the total linewidth measured. These contributions could be estimated as $\Delta f_\alpha = 1.2\,\text{MHz}$ and $\Delta f_{\text{sat}} = 5.7\,\text{MHz}$ respectively. The experimentally measured line shape can be described as a convolution of all line shape contributions and under the simplifying assumption of Lorentzian line shapes the total linewidth Δ_{exp} is given by the sum of all contributions. Hence the laser linewidth Δ_L can be estimated as $\Delta_L \approx \Delta f_{\text{exp}} - \Delta f_\alpha - \Delta f_{\text{sat}} \approx (48 \pm 4)\,\text{MHz}$. It is instructive to compare this result with an estimate of the minimum laser linewidth Δf_{ST} due to spontaneous emission as given by the Schawlow-Townes formula [YAR91]:

$$\Delta f_{ST} = \pi h f_L \frac{(\Delta f_{\text{res}})^2}{P}(1 + \alpha^2)\,. \tag{4.4}$$

With the laser emission frequency $f_L = 350\,\text{THz}$, the resonator width $\Delta f_{\text{res}} = c(1 - R)/(2\pi nLR) \approx 34\,\text{GHz}$ (length $L = 1.2\,\mu\text{m}$, mirror reflectivity $R = 0.997$), the α-factor $\alpha = 2.6$ [EBE97] and an output power $P = 500\,\mu\text{W}$ one gets $\Delta f_{ST} \approx 13\,\text{MHz}$ which is about a factor

of four below the value of Δf_{exp} obtained above. But this discrepancy can be understood at least qualitatively since the experimentally measured linewidth not only includes the quantum limited laser linewidth but also the influence of slowly varying noise components of the injection current arising, e.g., from power line interferences at 50 Hz. The large VCSEL linewidth might be responsible for the fact that in unbuffered cells the dark resonance contrast is extremely low because only a fraction of the laser power lies within the optical transition linewidth. Hence large improvements can be expected from a better VCSEL current stabilization in the future.

VCSEL injection current modulation The output frequency of diode lasers can easily be modulated via the injection current. For modulation frequencies above several MHz the temperature response of the diode can be neglected and the modulation behaviour is governed by the carrier density only. On the one hand, modulation of the injection current directly causes a modulation of the carrier density, hence the emission wavelength, via the refractive index and the optical length of the resonator. On the other hand, the carrier density also influences the electron-hole recombination rate and thus the optical output power via the number of photons present in the resonator. Therefore injection current modulation always entails both frequency and amplitude modulation of the laser emission.

In the standard approach a rate equation model of the carrier and photon density is used to calculate the frequency and output power response to the applied modulation [YAR91]. In a simplified version the model leads to a driven damped harmonic oscillator equation with a resonance frequency ω_R (also called relaxation frequency) at

$$\omega_R \simeq \sqrt{\frac{Bq_0}{t_c}} \tag{4.5}$$

where B is the amplification coefficient, q_0 the equilibrium photon density and t_c the photon lifetime in the resonator. In [AFF99] estimates for B, q_0 and t_c are discussed for both VCSEL and typical edge-emitting diode lasers. Although the photon lifetime

$$t_c = \frac{n}{c}(\alpha - \frac{1}{L}\ln R)^{-1} \tag{4.6}$$

(with refractive index n, loss per length α, resonator length L and mirror reflectivity R) decreases for shorter resonators, t_c is roughly the same for both the VCSEL and edge-emitting diodes because of higher mirror reflectivities for the VCSEL. In contrast, due to the high reflectivity and the small gain volume, the photon density is larger for the VCSEL such that the relaxation frequencies for output powers of 1 mW can be estimated as $\omega_R \approx 3.4\,\mathrm{GHz}$ and $\omega_R \approx 7\,\mathrm{GHz}$ for the edge-emitting laser and VCSEL, respectively.

The experimental characterization of the VCSEL modulation efficiency requires a spectrometer determining the relative strengths of the modulation sidebands. In principle this could be accomplished by a scanning Fabry-Perot interferometer or by registering the beat note of the modulated VCSEL impinging on a fast photodiode with subsequent detection at the modulation

frequency in a spectrum analyser. However, because of the experimental simplicity in the face of the large VCSEL linewidth and low total power, the procedure chosen was to retreat to a spectrometer based on cesium absorption spectroscopy again. For a given modulation frequency in the GHz range (input power +1 dBm) the VCSEL frequency was scanned via the DC current supply at a low repetition rate such that the absorption spectrum obtained in a cesium vapour cell (typical length 2 cm) could be recorded with a storage oscilloscope. The frequency width of the scan was chosen large enough to include both the carrier and all visible sideband contributions for the two 9.2 GHz spaced components of the D_2 line. Typical spectra recorded for modulation frequencies of $\omega_{\mathrm{mod}} = 2.5\,\mathrm{GHz}$, and $\omega_{\mathrm{mod}} = 7\,\mathrm{GHz}$, respectively, are shown in fig. 4.8. Whereas for $\omega_{\mathrm{mod}} = 2.5\,\mathrm{GHz}$ sidebands up to third order are visible the modulation efficiency decreases for higher frequencies such that only first order sidebands remain discernible. Furthermore, in the former spectrum the influence of amplitude modulation becomes obvious from the asymmetry of the sidebands of the same order but opposite sign.

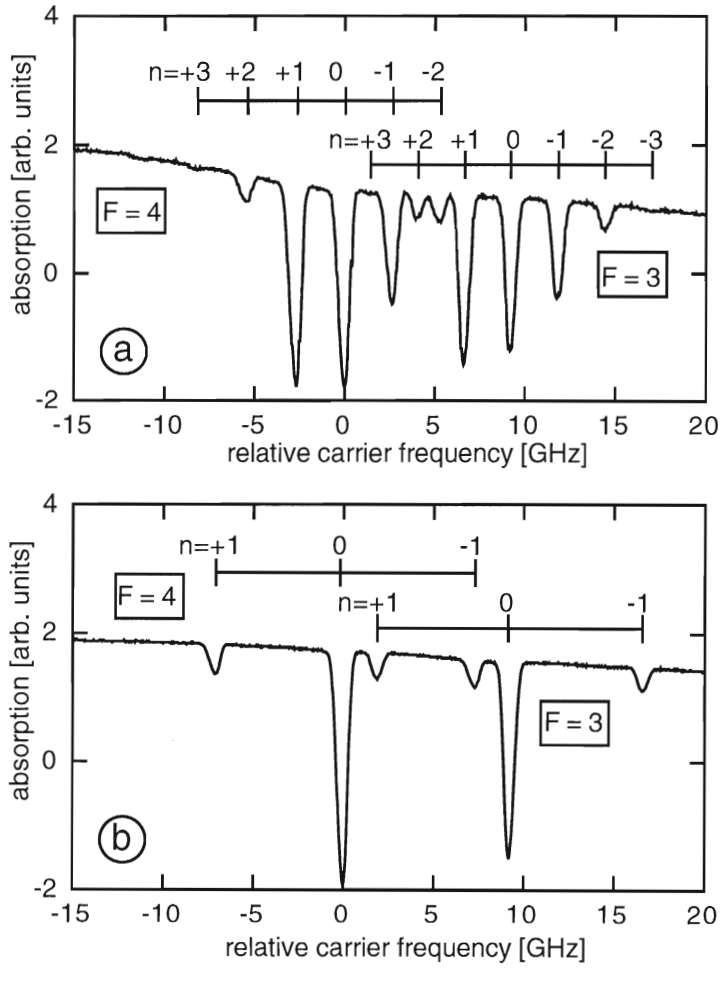

Figure 4.8: *Absorption spectra of the two* 9.2 GHz *spaced components of the cesium* D_2 *line with a VCSEL modulated at (a)* $\omega_{\mathrm{mod}} = 2.5\,\mathrm{GHz}$ *and (b)* $\omega_{\mathrm{mod}} = 7\,\mathrm{GHz}$. *The sideband order is denoted n. As the modulation efficiency decreases for increasing modulation frequency only first order sidebands remain visible for the higher modulation frequency.*

Under the given experimental conditions of an optically thin vapour and negligible saturation the measured strength of each absorption peak is proportional to the power contained in the respective frequency component, such that the relative absorption peak height can be taken as a measure of the relative frequency component strength. Hence the relative strengths of all peaks (taking into account the sloping background due to the laser power increasing with the laser current) could be determined as a function of modulation frequency.

Since the VCSEL α-factor is typically of the order of 3 one expects both amplitude and frequency modulation if the VCSEL injection current is modulated in the GHz range. According to the derivation given in appendix C the relative strength S_n of the n-th sideband is given by:

$$S_n = \frac{J_n^2(M)(1 + 2n\frac{R}{M}\sin(\psi) + n^2\frac{R^2}{M^2}) - \frac{R^2}{2}J_{n-1}J_{n+1}(1 + \cos(2\psi))}{1 + \frac{R^2}{2}} \tag{4.7}$$

where M is the phase modulation index, R the amplitude modulation index, ψ the phase shift between frequency and amplitude modulation, and $J_n(M)$ denotes the n-th Bessel-function of M. S_n was normalized to a total line strength of unity.

For each modulation frequency R, M, ψ were obtained from a fit of the sideband strengths given by eq. (4.7) to the experimentally determined values. Obviously, with this method the modulation efficiency at 9.2 GHz can only be determined from an interpolation because two first order sideband contributions coincide with the carrier of the other D_2 line component and thus cannot be resolved. Similar arguments hold true for $\omega_{\mathrm{mod}} = 3\,\mathrm{GHz}$ and $\omega_{\mathrm{mod}} = 4.5\,\mathrm{GHz}$.

For modulation frequencies above 6.5 GHz the amplitude modulation contribution becomes too small for a reasonable fit of R and ψ. Hence for higher frequencies pure frequency modulation is assumed: $R = 0$, $\psi = 0$ and eq. (4.7) reduces to $S_n = J_n(M)^2$.

With the fitted values for M the frequency excursion $\Delta\omega = \omega_{\mathrm{mod}} \cdot M$ was calculated and the resulting frequency dependence of $\Delta\omega$ is depicted in fig. 4.9.

$\Delta\omega$ clearly shows the expected resonant behaviour. Using the formula for the amplitude $A(\omega)$ of a driven damped harmonic oscillator

$$A(\omega) = \frac{A_0}{\sqrt{(\omega^2 - \omega_R^2)^2 + \gamma^2\omega^2}} \tag{4.8}$$

a fitted value of $\omega_R = (6.8 \pm 0.2)\,\mathrm{GHz}$ was obtained which is of the same order of magnitude as expected. Still, it has to be kept in mind that in the experiment described above only the modulation response of the complete VCSEL system was determined instead of the response of the bare VCSEL. This included losses and impedance mismatching effects in the connectors or the VCSEL housing but gives the relevant information needed for precision spectroscopy.

Moreover, the simple formula for $A(\omega)$ also yields an estimate of the modulation bandwidth $\Delta\omega_{1/2}$ of the system, defined as the modulation frequency for which the modulation efficiency

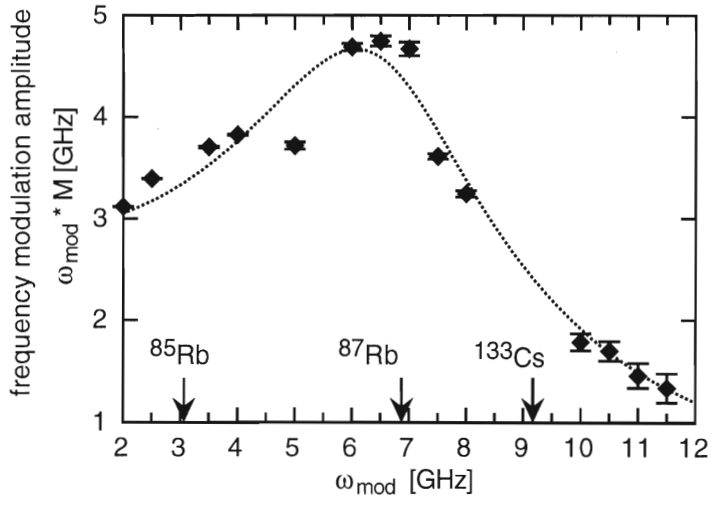

Figure 4.9: *VCSEL frequency modulation amplitude* $\Delta\omega = \omega_{\mathrm{mod}} * M$ *as a function of the modulation frequency* ω_{mod}. *The resonant behaviour allows to estimate the relaxation frequency* $\omega_R \approx 6.5$ *GHz. Arrows indicate the ground state hyperfine splitting of Cs,* ^{85}*Rb and* ^{87}*Rb.*

has dropped to half the value at $\omega = 0$. The result is $\Delta\omega_{1/2} \approx 10.2\,\mathrm{GHz}$ which again is of the same order of magnitude as expected [EBE97].

Further details and a comparison with the modulation response of a conventional edge-emitting diode laser can be found in [AFF99].

Interpolation of M to the modulation frequency $\omega_{\mathrm{mod}} = 9.2\,\mathrm{GHz}$ yields $M_{9\mathrm{GHz}} = 0.26$, corresponding to a power fraction contained in the first order sideband of about 1.7 %. This value will be used for the theoretical calculations presented in chapter 5.

5 Experimental characterization of CPT resonances

In order to exploit an experimental phenomenon for precision measurements a detailed understanding of the phenomenon itself is a prerequisite. Optimization would further include the enhancement of favourable features and, if possible, the suppression of influences which might falsify the measurements.

The main application envisioned for CPT resonances consists in measuring extremely small magnetic fields via the Zeeman shift of the resonance line thus employing the resonance line as a frequency discriminator. In such a measurement system the dark resonance absorption or dispersion signal would be monitored for a suitably chosen but fixed Raman detuning δ_R of the lasers. Then any line shift of the dark resonance manifests itself in a change of the recorded measurement signal, as illustrated in fig. 5.1. The main concern of this chapter is to report the first detailed experimental characterization of the dark resonance with respect to this application.

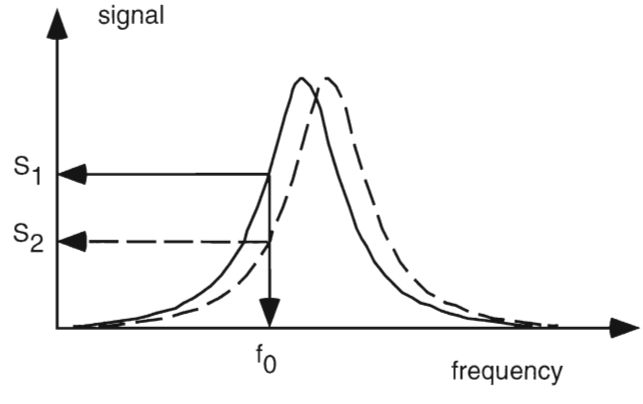

Figure 5.1: *Principal idea of precision measurements with resonant features: for fixed driving frequency f_0 line shifts cause changes in the corresponding measurement signals from S_1 to S_2.*

The main phenomenon to be investigated is the dark resonance response to an external static magnetic field. For a given pair of ground state Zeeman levels the corresponding dark resonance Zeeman shift can directly be taken from the Breit-Rabi formula, whereas the number and relative strengths of the Zeeman components present for a given experimental situation is not at all obvious. Nonetheless, excellent agreement between the multilevel-theory developed in section 3.3 and the experimental evidence given in section 5.1 will show that all Zeeman line shifts and splittings are well understood.

Based on this knowledge, an important step towards optimization of the system consists of the reduction of the experimentally recorded linewidth because the steepness of the resonance line

is a crucial parameter. In the experiments described here this was done with the help of the buffer gas technique, as explained in section 5.3.

Coming back to the use of CPT resonances as frequency discriminators: in order to attribute a change in signal to the underlying effect of interest any other influences on the measurement signal have to be excluded or at least understood so that they can be corrected for. To begin with, this includes any effect which also shifts the dark resonance line. Therefore several frequency shifting influences such as AC-Stark shifts and buffer gas induced shifts will be discussed.

But there are also other categories of systematic influences which can change the relevant measurement signal of a frequency discriminator, e.g., changes in the overall line height and in linewidth arising from the dark resonance dependence on intensity, as examined in section 5.6. Changes in line shape can have a similar effect, therefore they are discussed in section 5.2.

Detailed understanding of external influences on the CPT resonance also helps to find the best operating conditions for a CPT-based magnetometer. The set of parameters to be optimized with respect to the signal-to-noise ratio (S/N), the susceptibility to fluctuations etc., would contain, for instance, both total and relative laser intensities, optical detuning from one-photon resonance, buffer gas pressure etc. Although the current status of the experiment is still far from a refined implementation of the device, some interesting correlations between various influences are readily found.

Although the presence of a buffer gas allows for very small linewidths it also constitutes a source of frequency shift and reduces the S/N ratio due to a decrease of the dark resonance contrast [ARI96B]. A similar argument holds for the laser intensity, because decreasing intensity yields both a narrow line and a reduced AC-Stark shift, but also a worse S/N ratio.

For the experimental study of the influence of parameters other than a magnetic field, one can reduce the influence of shifts and line broadening from magnetic field inhomogeneities if in a small longitudinal magnetic field (typically few tens of μT) $\sigma^+\sigma^+$ laser polarizations are used and only the $0-0$ component is considered. It corresponds to the coherence between the $|S_{1/2}, F=4, m_F=0\rangle$ and $|S_{1/2}, F=3, m_F=0\rangle$ levels and is shifted by magnetic fields merely in second order. This particular experimental configuration will be referred to as the standard configuration throughout this chapter. Yet, other dark resonance components might show deviations — however minute — from the behaviour of the $0-0$ component because of different Clebsch-Gordan coefficients. Therefore, for ultimate accuracy it will be necessary to scrutinize the behaviour of those components in an extremely homogeneous magnetic field which was not available at the time these experiments were performed.

5.1 Multilevel effects

This section compares the predictions of the multilevel-model developed in chapter 3.3 with the experimentally recorded Zeeman split dark resonance spectra in terms of their dependence on polarization and magnetic field direction. The first sections might be summarized as 'low resolution effects' whereas in sections 5.1.4, 5.1.5 more subtle effects are discussed which demanded much higher homogeneity of the applied magnetic field.

The dependence of the relative line strengths on magnetic field direction is illustrated in Fig. 5.2 with a series of spectra recorded with identical circular laser polarizations in a cell with 87 mbar of neon as a buffer gas. β denotes the angle between the laser propagation and the magnetic field direction. When β is increased the seven even-numbered resonances seen at low β gradually vanish while the eight odd-numbered resonances continually grow until, for β approaching 90°, they alone make up the spectrum.

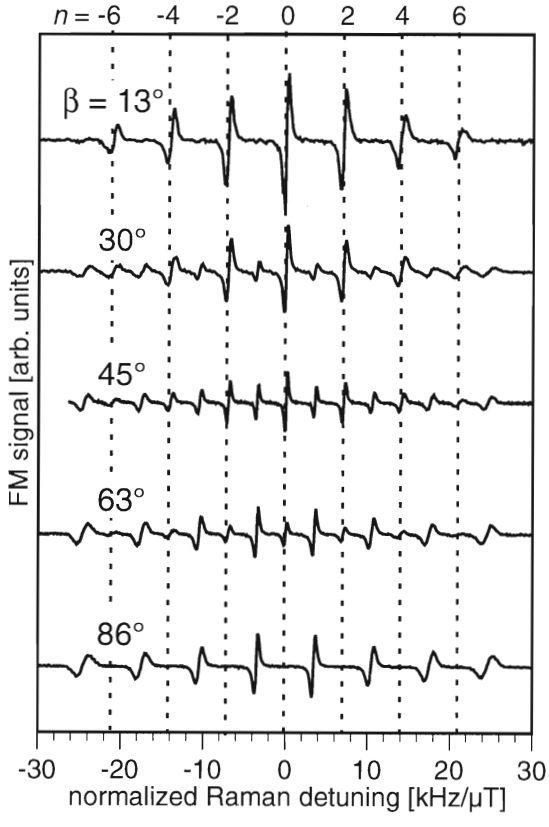

Figure 5.2: *Dark resonance spectra for $\sigma^+\sigma^+$ excitation and different angles β between laser beam and external magnetic field ($B \approx 10\,\mu$T, 87 mbar Ne buffer gas). The dispersive line shapes are due to the lock-in detection.*

The effect of the inhomogeneity of the magnetic field within the interaction region becomes clearly visible from the fact that the linewidth of the dark resonance Zeeman components increases with $|n| = |m_3 + m_4|$. In an inhomogeneous field every atom, confined within its own

small region in space due to the extremely slow diffusion in the atmosphere of high buffer gas pressure, experiences a different magnetic field strength. That is to say the dark resonance positions differ from one atom to the next such that the sum over all atoms renders a broadened line. Since the resonance position is proportional to n this line broadening effect is worse for larger $|n|$. Therefore, in order nevertheless to compare relative line strengths one has to consider the areas under the respective lines instead of their peak heights. Hence the evaluation of the raw spectra in Fig. 5.2 consists of a first integration to retrieve absorptive line shapes, followed by a second integration to determine the area under each peak. Finally the relative line strengths were normalized to unit total area for every complete spectrum. The results can be used to check two different predictions of the model: the angular dependence of the fraction of overall line strength contained in the even- and odd-numbered peaks, respectively, and the relative strength of different peaks for a fixed β.

Total line strengths As indicated before, a rotation of the magnetic field direction by β around the y axis can be accounted for by a rotation of the polarization tensor components $a_Q^{(K)}$. This is accomplished with the help of eq. (3.24).

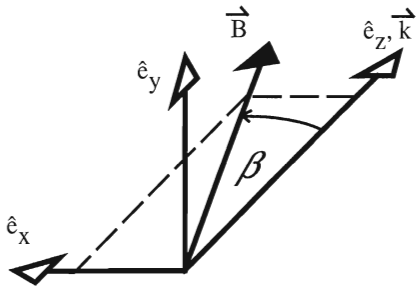

Figure 5.3: *The magnetic field is rotated against the light propagation directions by an angle* β

In the experimental situation depicted in fig. 5.2 both light beams are σ^+ polarized with respect to their propagation direction $\hat{e}_z$ along the quantization axis ($\beta = 0$). For arbitrary values of β the polarization tensor components are

$$\begin{aligned}
\tilde{a}_2^{(2)} &= -\tfrac{1}{4}\sin^2\beta & & \\
\tilde{a}_1^{(2)} &= -\tfrac{1}{4}\sin 2\beta & \tilde{a}_1^{(1)} &= -\tfrac{1}{2}\sin\beta \\
\tilde{a}_0^{(2)} &= \tfrac{1}{\sqrt{6}}(\tfrac{3}{2}\sin^2\beta - 1) & \tilde{a}_0^{(1)} &= -\tfrac{1}{\sqrt{2}}\cos\beta \\
\tilde{a}_{-1}^{(2)} &= \tfrac{1}{4}\sin 2\beta & \tilde{a}_{-1}^{(1)} &= \tfrac{1}{2}\sin\beta \\
\tilde{a}_{-2}^{(2)} &= -\tfrac{1}{4}\sin^2\beta &
\end{aligned} \quad . \tag{5.1}$$

For $\beta = 0°$ only the $Q = 0$ components $a_0^{(2)}, a_0^{(1)}$ do not vanish so that only the seven even-numbered peaks are allowed; this is approximately the situation depicted in the uppermost spectrum of fig. 5.2a. For $\beta = 90°$ the components $\tilde{a}_0^{(2)}, \tilde{a}_{\pm 2}^{(2)}, \tilde{a}_{\pm 1}^{(1)}$ do not vanish. But since in the

limit of high buffer gas pressure the $K = 2$ contribution practically vanishes only components with $|Q| = 1$ remain such that only the eight odd-numbered peaks are present in the spectrum. Thus in the high buffer gas pressure limit the coupling strength as a function of magnetic field direction reduces to:

$$S_{\text{rel}}^{\text{buffer gas}} \propto |A_\Lambda(K=1)|^2 \propto \cos^2\beta \qquad \text{for } Q = 0 \tag{5.2}$$

$$S_{\text{rel}}^{\text{buffer gas}} \propto |A_\Lambda(K=1)|^2 \propto \sin^2\beta \qquad \text{for } Q = \pm 1\,. \tag{5.3}$$

For a comparison of the experimental data with this result the sum S_{even} of the strengths S_{2i} of the seven even-numbered resonances and the sum S_{odd} of the eight odd-numbered resonances S_{2i+1} were normalized to the total strength $S = S_{\text{even}} + S_{\text{odd}}$ (squares and circles in Fig. 5.4). There is quantitative agreement with the expected $\sin^2$ and $\cos^2$ dependence on β which is indicated by the solid line. The systematic deviation apparently present (the circles are mostly too high whereas the squares are too low) might be due to a spurious magnetic field component in the y direction or imperfect polarizations.

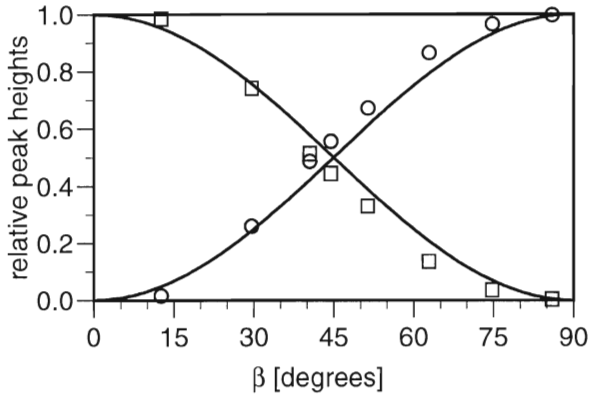

Figure 5.4: *Measured resonance strengths for the 7 'longitudinal' peaks (squares) and the 8 'transverse' peaks (circles), cf. fig. 5.2, normalized to the total strength of all resonances. The solid lines correspond to* $\cos^2(\beta)$ *and* $\sin^2(\beta)$.

5.1.1 Relative line strengths

Fig. 5.5 shows the relative line strengths of the Zeeman components present for specific magnetic field directions for the same experimental situation as in the preceding paragraph. Columns represent the line strengths determined from the area under each experimental peak. The theoretical values were obtained by inserting the rotated tensor components $\tilde{a}_Q^{(K)}$ into the expression for the transition rate in eq. (3.31). Subsequently the coupling strengths were normalized to a total line strength of unity. Solid circles give the calculated results in the high buffer gas limit which can hardly be distinguished from the exact calculation indicated as a dashed line for

$\beta = 45°$. The value $\Gamma_s = 2\pi \cdot 300\,\mathrm{MHz}$ was estimated from a fit of a Voigt profile to a Doppler broadened absorption line in the presence of this buffer gas pressure. A comparison of the line strengths as depicted in fig. 5.5 with the raw spectra again illustrates the line broadening due to field inhomogeneities. For $\beta = 86°$ the outermost lines are the strongest components (columns in fig. 5.5) although in fig. 5.2 they appear with the smallest peak height.

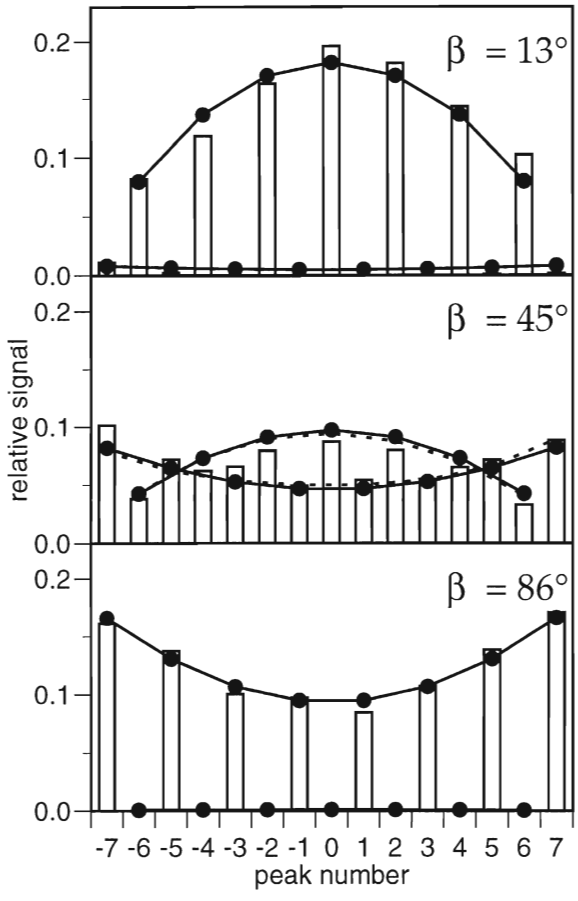

Figure 5.5: *Comparison of measured (columns) and calculated (dots) resonance strengths for selected spectra of fig. 5.2. The dashed lines for $\beta = 45°$ correspond to a complete calculation using eq.* (3.27) *with $\Gamma_s = 2\pi \cdot 300\,\mathrm{MHz}$ while for the dots (connected by solid lines) eq.* (3.34)*, i.e., the limit of high buffer gas pressure, was used.*

5.1.2 Change of multipolarity

In all of the spectra presented so far equal circular polarizations were used. As discussed in chapter 4.2.3 the polarization was produced with the help of a polarizer in front of a quarter wave plate inserted in the laser beam path. Depending on the angle φ between the optic axis of the quarter wave plate and the linear input polarization an output polarization with a certain ellipticity is produced. When φ is gradually changed from 0° to 45° the corresponding output

polarization is transformed from linear to circular. With the notations used in fig. 5.6a the laser polarizations as a function of φ can be expressed in the following way:

$$\begin{aligned}\vec{E}_1 &= E_{10}(\cos\varphi \cdot \hat{e}_x + i \sin\varphi \cdot \hat{e}_y) \\ &= E_{10}\big((\cos\varphi - \sin\varphi) \cdot \hat{e}_x - \sqrt{2}\sin\varphi \cdot \sigma^+\big)\end{aligned} \tag{5.4}$$

and similarly for $\vec{E}_2^*$, resulting in the following $a_Q^{(K)}$:

$$\begin{array}{ll} \tilde{a}_2^{(2)} = \frac{1}{2}\cos 2\varphi & \\ \tilde{a}_1^{(2)} = 0 & \tilde{a}_1^{(1)} = 0 \\ \tilde{a}_0^{(2)} = -\frac{1}{\sqrt{6}} & \tilde{a}_0^{(1)} = \frac{1}{\sqrt{2}}\sin 2\varphi \\ \tilde{a}_{-1}^{(2)} = 0 & \tilde{a}_{-1}^{(1)} = 0 \\ \tilde{a}_{-2}^{(2)} = \frac{1}{2}\cos 2\varphi & \end{array} \quad . \tag{5.5}$$

Hence for $\varphi = 0$ one anticipates zero line strength for high buffer gas pressures (i.e., negligible contribution of $K = 2$) which should gradually increase as a function of reduced buffer gas pressure. In the high buffer gas limit the line strength is anticipated to depend on φ like $\sin^2(2\varphi)$. For the experimental proof three different sealed cells containing 0, 13 and 87 mbars of neon, respectively, were used and dark resonance spectra were recorded as a function of the rotation angle φ of the quarter wave plate. Fig. 5.6 then shows the line strength normalized to unity at $\varphi = 45°$ as a function of φ. The solid lines result from a numerical fit to a $x + (1-x)\sin^2(2\varphi)$ dependence which yields $x = (0.45, 0.095, 0.036)$ for buffer gas pressures of $(0, 13, 87)$ mbar. This clearly indicates the gradual change in multipolarity due to increasing γ_s.

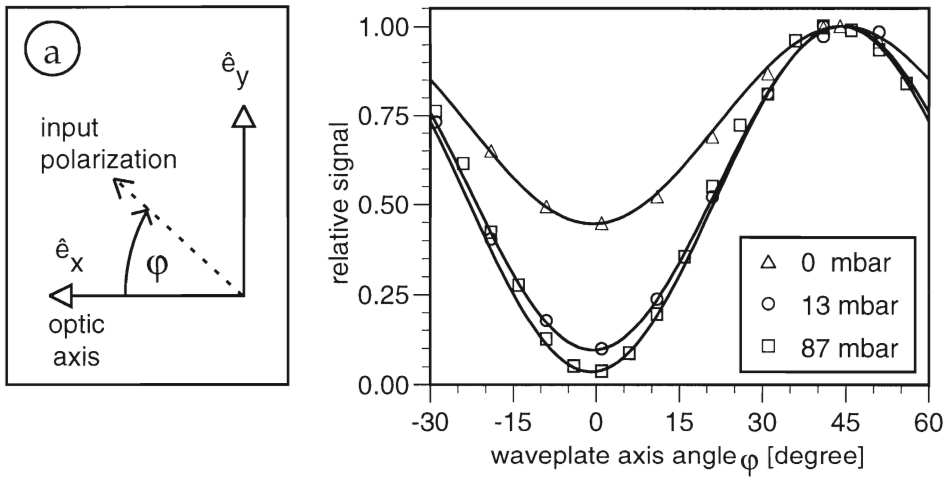

Figure 5.6: *Dependence of resonance strength on laser polarization in zero magnetic field for different neon pressures. $\varphi = 45°$: circular, $\varphi = 0°$: linear polarization. The solid line is a numerical fit with a $\sin^2(2\varphi)$ dependence on top of a constant offset.*

5.1.3 Polarization dependence in pure cesium vapour

The same procedure as in section 5.1.1 could be applied to a series of measurements which had been recorded by O. Schmidt [SCH95] several years before. Fig. 5.7 shows Zeeman split dark resonance spectra for various polarizations, recorded in pure cesium vapour and in the presence of a longitudinal magnetic field. As in this case saturation broadening of the lines is considerably larger than the broadening due to field inhomogeneities the experimental spectra can directly be compared to the theoretical line strengths calculated from equations (3.30) and indicated by crosses in the plots. The overall agreement is again very good, minor discrepancies might be due to imperfect polarizations. From the experimental side this is a problem commonly encountered with quarter wave plates which usually produce the correct polarizations only to within a few percent at best. But the presence of unwanted polarization components leads to additional contributions to the line strengths, which again depend on m_F.

Whereas the spectra on the left-hand side of fig. 5.7 correspond to pure $K = 2$ coupling the ones on the right involve both $K = 1$ and $K = 2$ couplings. Therefore the former will hardly be visible in buffered cells whereas the polarization configurations on the right would lead to well visible spectra in buffered cells as well. However, due to the different formulae used for the unbuffered cell (see eqs. (3.31), (3.30)) the relative line strengths considerably differ from those obtained from a buffered cell. For instance, compare the spectra for $\sigma^+\sigma^+$ polarizations in fig. 5.7 and fig. 5.5.

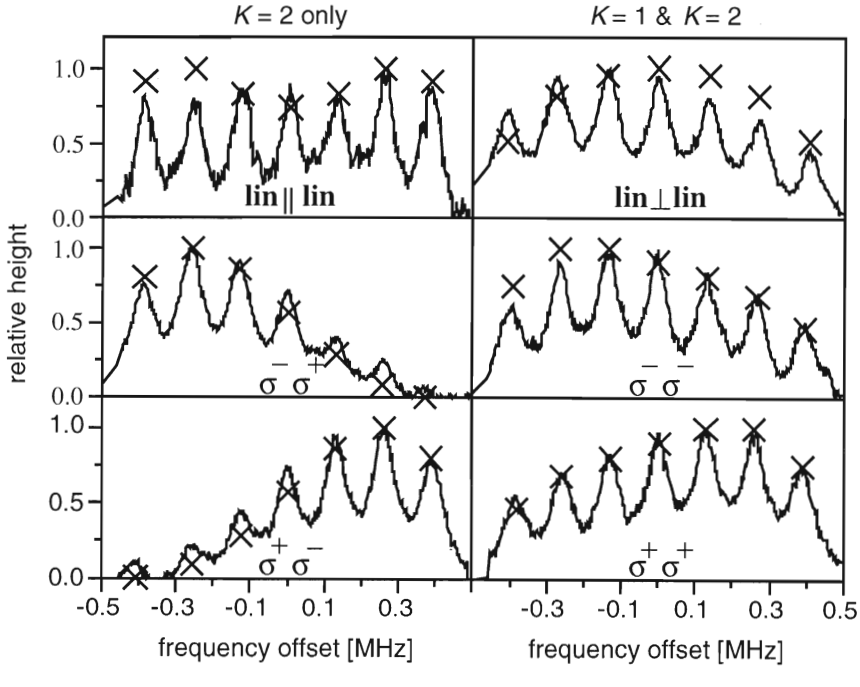

Figure 5.7: *Polarization dependence of line strengths in a cesium cell without buffer gas (crosses: calculated values). The highest peak in each spectrum was normalized to unity (experimental data taken from* [SCH95]*).*

5.1.4 Line splitting due to the nuclear contribution

As it was demonstrated in the preceding section, for $\sigma^+\sigma^+$ polarizations in a transverse magnetic field eight Zeeman split dark resonance peaks were recorded. From the Breit-Rabi formula the position of these peaks labeled n (with $n = m_3 + m_4$) was derived as (see eq. (3.16)):

$$\xi \approx \frac{\mu_B}{8h} B\big(g_J(m_3 + m_4) + g_I(7m_4 - 9m_3)\big) \qquad \text{(in the linear Zeeman case).} \tag{5.6}$$

Hence for fixed peak number n one still has to distinguish between the possible values of $\Delta m = m_4 - m_3$.

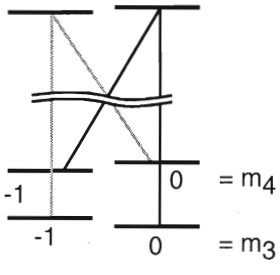

Figure 5.8: *For $\sigma^+\sigma^+$ polarizations in a transverse magnetic field: possible couplings between two Zeeman levels for the same n but different Δm.*

A typical level configuration is sketched in fig. 5.8. Using a buffer gas cell, according to eq. (5.1) for $\sigma^+\sigma^+$ polarizations in a transverse magnetic field the non-zero components of the polarization tensor a_Q^K are $\tilde{a}_1^{(1)} = -1/2$ and $\tilde{a}_{-1}^{(1)} = 1/2$. Then for given n the relevant part of eq. (3.23) reduces to:

$$\begin{aligned} A_\Lambda &\propto \left| \begin{pmatrix} F_f & 1 & F_i \\ -(n+1)/2 & +1 & (n-1)/2 \end{pmatrix} \right|^2 \quad \text{for} \quad \Delta\mathrm{m} = +1\,, \\ A_\Lambda &\propto \left| \begin{pmatrix} F_f & 1 & F_i \\ -(n-1)/2 & -1 & (n+1)/2 \end{pmatrix} \right|^2 \quad \text{for} \quad \Delta\mathrm{m} = -1\,. \end{aligned} \tag{5.7}$$

Thus under suitable experimental conditions one expects to resolve the two components making up the odd-numbered peaks which — according to eq. (5.6) — are separated by the purely nuclear contribution only. From eq. (5.7) the relative heights of the double peaks are anticipated as:

$$\begin{aligned} 5:3 \quad & \text{for the } n = 1 \text{ peak} \\ 5:1 \quad & \text{for the } n = 3 \text{ peak} \\ 21:1 \quad & \text{for the } n = 5 \text{ peak} \end{aligned} \tag{5.8}$$

whereas the $n = 7$ peak does not split since one of the $3j$ symbols vanishes.

From eq. (5.6) the shift rate of the nuclear contribution can be inferred as $S_{\text{nuclear}} = 11.16\,\text{Hz}/\mu\text{T}$ such that some severe conditions are imposed on an experiment aimed to resolve these double peaks. The detection of peaks with rather low overall line strengths and in part even considerably different heights (for $n = 2, 3$) necessitates sufficient optical power from the bichromatic field. But this in turn causes saturation broadening of all dark resonance lines. Hence in order to overcome this problem, too, the magnetic field has to be strong enough which on the other hand again causes considerable line broadening due to field inhomogeneities. Therefore one has to apply magnetic fields that are extremely homogeneous over the interaction region in the cesium cell. Experimentally this was accomplished by special pairs of tapered current coils both for longitudinal and transverse fields positioned inside a triple layer μ-metal shielding. Since it usually takes at least a few minutes to record a whole dark resonance spectrum effective line broadening does not only arise from spatial field inhomogeneities but also from temporal variations of the coils' supply current. In total, the relative field homogeneity reached over the interaction region could be estimated as $6 \cdot 10^{-4}$ [KNA99]. Apart from line broadening due to current fluctuations line shifts might arise from current drifts due to thermal resistivity changes along the wires. To estimate the order of magnitude of this effect one can consider a typical situation with $I = 3\,\text{A}$ producing a flux density of $B = 0.26\,\text{mT/A} \cdot 3\,\text{A} = 0.78\,\text{mT}$. Then the $n = 5$ peak will be shifted by about 16 MHz while the double peaks should be separated by about 10 kHz. If one assumes 0.1% relative current stability the peak position can jitter by 16 kHz which is of the same order of magnitude as the splitting to be observed. Hence the use of an active current stabilization scheme would be the appropriate measure to be taken if one desired to exploit this splitting for precision measurements, e.g., the determination of g-factor ratios. Nevertheless, it was possible to demonstrate the splitting even without such a device. In contrast to the experiments described so far in this chapter, the VCSEL set-up was used.

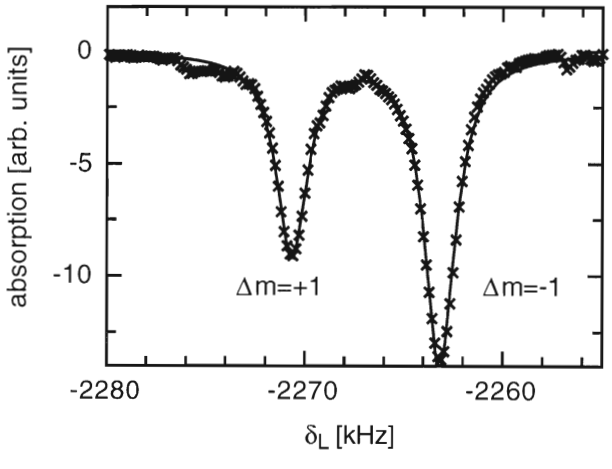

Figure 5.9: *Deconvoluted line shape of the $n = -1$ peak for $\sigma^+\sigma^+$ polarizations in a transverse magnetic field. Due to the nuclear contribution the two peaks corresponding to the two Λ-systems of fig. 5.8 with $\Delta m = +1$ and $\Delta m = -1$, respectively, are completely resolved. The solid line represents fitted Lorentzian profiles.*

Fig. 5.9 shows the deconvoluted line shape for the $n = -1$ peak obtained in a cell containing 200 mbar of neon and in a field of 0.68 mT flux density, where the peak is completely split into the $\Delta m = +1$ and $\Delta m = -1$ components.

From fig. 5.10 which shows the calculated relative peak heights of the two components for all possible values of n it becomes obvious that for equal absolute values of n but opposite sign the ratio of the relative strengths is inverted. This effect could also be proved experimentally, as demonstrated in fig. 5.11.

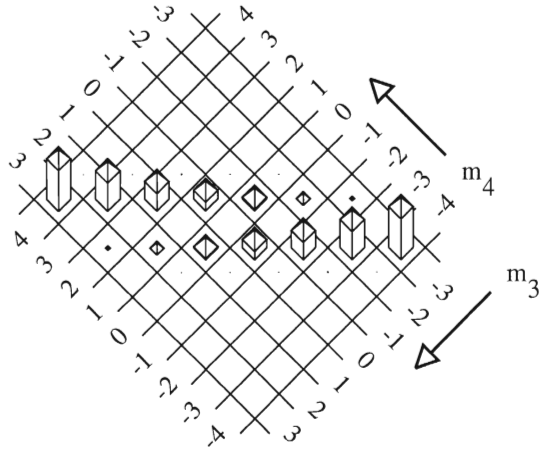

Figure 5.10: *Calculated relative peak heights for $\sigma^+\sigma^+$ polarizations in a transverse magnetic field as a function of the magnetic quantum number of each possible pair of ground states involved.*

From a fit with Lorentzian line profiles one obtains for the relative line strengths of fig. 5.11:

$$\begin{aligned}
\frac{S_{\mathrm{rel}}(n=+1,\Delta m=+1)}{S_{\mathrm{rel}}(n=+1,\Delta m=-1)} &= 0.59 \quad \pm 0.01 \\
\frac{S_{\mathrm{rel}}(n=-1,\Delta m=-1)}{S_{\mathrm{rel}}(n=-1,\Delta m=+1)} &= 0.62 \quad \pm 0.01 \\
\frac{S_{\mathrm{rel}}(n=+3,\Delta m=-1)}{S_{\mathrm{rel}}(n=+3,\Delta m=+1)} &= 5.7 \quad \pm 0.2 \\
\frac{S_{\mathrm{rel}}(n=-3,\Delta m=+1)}{S_{\mathrm{rel}}(n=-3,\Delta m=-1)} &= 5.0 \quad \pm 0.1\,, \qquad (5.9)
\end{aligned}$$

which is roughly in agreement with the anticipation of eq. 5.7. Note that due to residual magnetic field inhomogeneities the $n = \pm 3$ peaks are considerably broader than the $n = \pm 1$ peaks.

5.1.5 Line splitting due to $K = 2$ contributions

Consider the situation illustrated in fig. 5.12: the lasers have equal linear polarizations and the purely transverse magnetic field is oriented perpendicular to the laser polarizations. For this

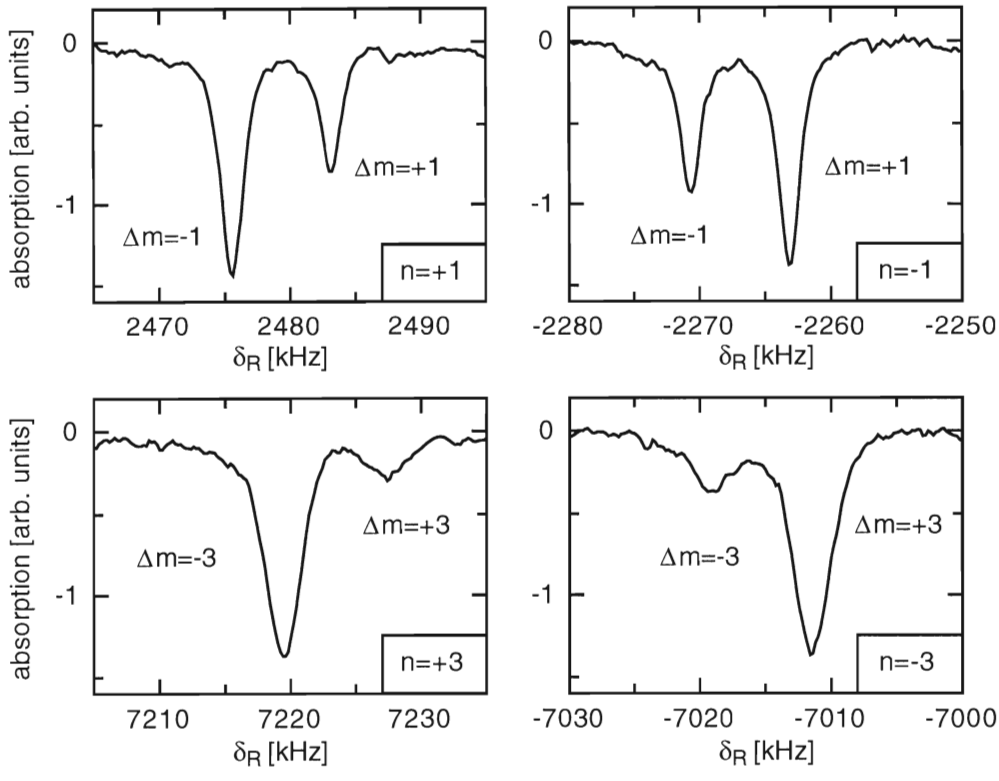

Figure 5.11: *Deconvoluted line shapes of the $n = \pm 1$ and $n = \pm 3$ peaks under the same experimental conditions as in fig. 5.9. The lines split in two components with relative line strengths according to eq.* (5.7).

configuration the model predicts that the $n = 0$ peak consists of two $K = 2$ contributions of equal strength with $\Delta m = \pm 2$. The two corresponding Λ-systems are illustrated in fig. 5.12 as well.

The $K = 2$ contribution connects the pairs of ground state levels ($|F = 4, m_F = -1\rangle$, $|F = 3, m_F = 1\rangle$) and ($|F = 4, m_F = 1\rangle$, $|F = 3, m_F = -1\rangle$) which are shifted by twice the nuclear contribution of $\mu_B g_I B/2h$ from each other. Because of the smallness of the expected splitting again special attention was paid to the homogeneity of the applied magnetic field. Due to the large VCSEL linewidth dark resonances with good signal-to-noise ratio at low intensities cannot be obtained in unbuffered cells with the VCSEL set-up. But on the other hand, the presence of buffer gas suppresses the $K = 2$ contribution. Hence with the VCSEL set-up one has to use a buffer gas pressure high enough to obtain a reasonable S/N ratio but low enough not to suppress the $K = 2$ contribution completely. Fig. 5.13 shows the expected splitting in a deconvoluted spectrum which was obtained in a cell containing 9.9 mbar of neon and a transverse field of about 650 μT.

Since the S/N was very poor for those 'forbidden' resonances long averaging times were needed (1 s per measurement point, and the curve in fig. 5.13 consists of an average over 20 spectra). Therefore the influence of line broadening due to current drifts is not negligible and the spectrum

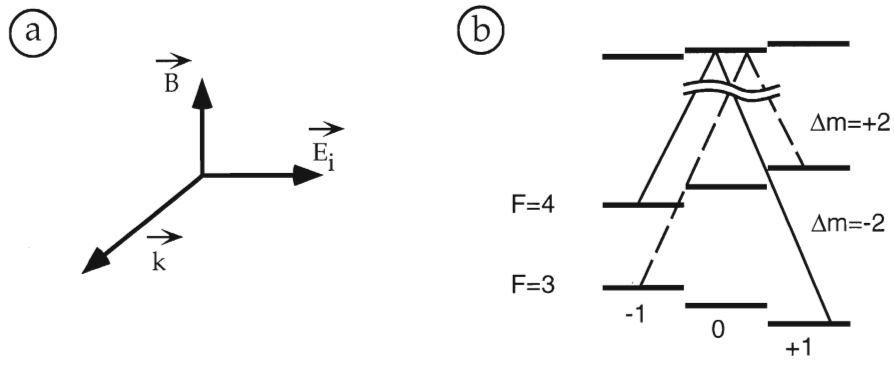

Figure 5.12: *(a) Geometrical configuration for the observation of dark resonances split according to $K = 2$ contributions only and (b) the respective Λ-systems involved.*

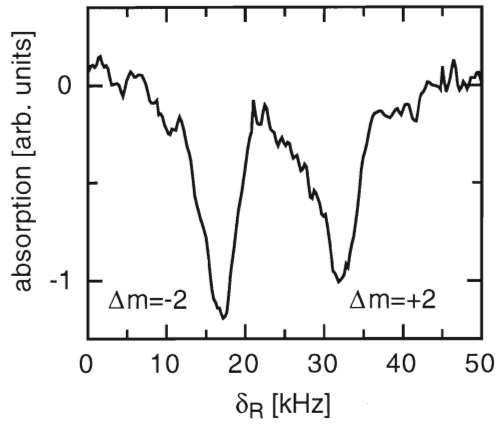

Figure 5.13: *Deconvoluted dark resonance line shape split due to contributions of multipolarity $K = 2$, where the geometrical configuration and ground state levels involved are those of fig. 5.12.*

of fig. 5.13 appears very broad. Drifts might also be responsible for the line shape distortions visible. The peak strengths, determined from the area under the respective curves, are equal to each other to within a few percent, which is again in agreement with the prediction of the model. Although the S/N ratio is rather poor in this experimental configuration, $\Delta m = 2$ coherences might be advantageous for precision magnetometry experiments because the corresponding Zeeman splitting increases with Δm.

5.1.6 Comparison with microwave transitions

As the main mechanism in coherent population trapping is the creation of ground state coherence one can compare the results obtained above with other configurations based on the creation of the same ground state coherences. Obviously the simplest example is the direct radiative transition between the two hyperfine-split ground states at 9.2 GHz microwave frequency. Because of parity

conservation the lowest allowed order is a magnetic dipole transition. With the polarization of the magnetic field expressed in spherical tensor components: $\vec{H} = \sum_q b_q \vec{e_q}$, the transition amplitude A between two Zeeman components $|F_i\ m_i\rangle$ and $|F_f\ m_f\rangle$ is given by:

$$\begin{aligned} A &\propto \langle F_f\ m_f|\,\vec{\mu}\cdot\vec{H}\,|F_i\ m_i\rangle \\ &\propto \sum_q (-1)^q b_{-q}\,\langle F_f\ m_f|\,l_q\,|F_i\ m_i\rangle \\ &\propto \mathcal{M}^{(\mathrm{M1})} \sum_q b_{-q} \begin{pmatrix} F_f & 1 & F_i \\ -m_f & q & m_i \end{pmatrix} \end{aligned} \tag{5.10}$$

with an amplitude

$$\mathcal{M}^{(\mathrm{M1})} = (-1)^{F_i+F_f+I+J+1-m_i} \sqrt{(2F_i+1)(2F_f+1)} \begin{Bmatrix} I & F_f & J \\ F_i & I & 1 \end{Bmatrix} \langle J\|I\|J\rangle \tag{5.11}$$

independent of geometry. This amplitude A can be compared with the respective transition amplitude A_Λ as calculated in section 3.3.2:

$$A_\Lambda \propto \sum_{K,Q} (-1)^Q a^K_{-Q} \begin{pmatrix} F_f & K & F_i \\ -m_f & Q & m_i \end{pmatrix} \mathcal{M}^{(K)}. \tag{5.12}$$

Hence, if only $K = 1$ coupling is possible for dark resonance preparation one can find a combination of microwave polarization and static magnetic field direction such that $b_{-q} = a^1_{-Q}$ for all contributions in the sum. This is based on the fact that the product of two spherical tensor operators of rank k_1, k_2 can uniquely be decomposed into the direct sum of its irreducible components, i.e., tensor operators of rank $|k_1 - k_2|...k_1 + k_2$. For $K = 1$ the components a^1_{-Q} form a basis set of the irreducible subspace such that any arbitrary polarization can be synthesized. Now, if both multipole amplitudes $\mathcal{M}^{(\mathrm{M1})}$ and $\mathcal{M}^{(1)}$ do not vanish one can arrive at the same spectrum, i.e., identical relative strengths of the various Zeeman components involved, for both the direct microwave transitions and the dark resonance.

However, in general the dark resonance spectrum looks different due to the interference between contributions of different multipolarity. In microwave spectroscopy higher order multipole transitions can be realized via multi-photon transitions, i.e., in the case under investigation here one would have to compare the dark resonance $K = 2$ coupling to the respective two-microwave-photon transition at $\frac{1}{2}\cdot 9.2\,\mathrm{GHz}$. But since the two-photon transition occurs at half the frequency the respective absorption line appears at a completely different position in the overall spectrum. Another difference lies, of course, in the fact that in dark resonance preparation certain multipolarity contributions can be manipulated with the help of upper state properties which is not possible for direct microwave transitions, either.

Finally, in thermal equilibrium the population difference between the two cesium hyperfine components practically vanishes such that for microwave transitions the net effect of stimulated emission and absorption is almost zero. Hence in order to achieve higher signal strengths redistribution of population — typically via optical pumping — is necessary. But then the relative line

strength of the Zeeman components is dominated by the interplay of optical pumping processes and does not necessarily correspond to the bare coupling strengths any more.

5.2 Line shapes

5.2.1 Line shape retrieval

All of the experimental spectra were recorded with the help of frequency modulation techniques (FM). Frequency-modulation spectroscopy is based on the phase-sensitive detection of a signal modulated at frequency ω_m. In the experiment this was accomplished by frequency-modulation of the second light field (i.e., either the slave laser or the modulation sideband, depending on which experimental set-up was used) and subsequent detection of the measurement signal with a dual-phase lock-in amplifier. For a detailed account on the use of FM-techniques in absorption spectroscopy see, for instance, [TAK75, BJO83, LEN84, GEH85]. High sensitivity of this method stems from the fact that fluctuations, e.g., in intensity, at frequencies other than ω_m are averaged out and the influence of $1/f$ noise can be reduced by choosing high enough modulation frequencies ω_m. Furthermore, for negligible additional amplitude modulation (AM), a frequency sweep of the laser results in non-vanishing signal contributions only within the narrow frequency interval where the amplitude and phase of the light are modified by the absorptive and dispersive properties of the medium under study. Even if small residual AM is present, as it is the case for current-modulated diode lasers, there is still a fairly good suppression of backgrounds that vary only slowly with frequency. Moreover, phase sensitive detection allows to determine both the absorptive and the dispersive properties of the medium simply from the transmission signal.

In order to explain the line shapes recorded by the lock-in amplifier one starts from the incident electrical field E oscillating at frequency ω_0 which is frequency- and amplitude-modulated at frequency ω_m, with phase modulation index M and amplitude modulation index R:

$$E = \frac{E_0}{2}\left(1 + R\sin(\omega_m t + \psi)\right) e^{i(\omega_0 t + M\sin(\omega_m t))} + c.c. \tag{5.13}$$

If the lock-in amplifier reference signal is given by $\sin(\omega_m t + \varphi)$, the two lock-in output signals X, Y are then given by:

$$X = \eta e^{-2\delta_0(\omega)}\left[S(\omega)\cos\varphi - C(\omega)\sin\varphi\right] \tag{5.14}$$

$$Y = \eta e^{-2\delta_0(\omega)}\left[S(\omega)\sin\varphi + C(\omega)\cos\varphi\right] \tag{5.15}$$

where η is a proportionality constant that includes laser intensity, detector sensitivity, and the electronic gain factor of the lock-in amplifier. For correctly chosen φ the signals X, Y are simply proportional to S, C. If a signal independent of φ is to be gained one can choose $R = \sqrt{X^2 + Y^2}$.

For the in-phase and quadrature components S, C one finds under suitable approximations:

$$\begin{aligned} S(\omega) = \quad & J_0(M)J_1(M)\big(\phi_{+1} + \phi_{-1} - 2\phi_0\big) \\ + \quad & J_1(M)J_2(M)\big(\phi_{+2} + \phi_{-2} - \phi_{+1} - \phi_{-1}\big) \\ + \quad & \frac{1}{2}RJ_0^2(M)\Big(-\big[\phi_{-1} - \phi_{+1}\big]\sin\psi + \big[2 + 2\delta_0 - \delta_{+1} - \delta_{-1}\big]\cos\psi\Big) \\ + \quad & \frac{1}{2}RJ_1^2(M)\Big(-\big[\phi_{-2} - \phi_{+2}\big]\sin\psi + \big[4 + 6\delta_0 - 2\delta_{+1} - 2\delta_{-1} - \delta_{+2} - \delta_{-2}\big]\cos\psi\Big) \end{aligned} \tag{5.16}$$

$$\begin{aligned} C(\omega_0) = \quad & J_0(M)J_1(M)\big(\delta_{-1} - \delta_{+1}\big) \\ + \quad & J_1(M)J_2(M)\big(\delta_{-2} - \delta_{+2} + \delta_{-1} - \delta_{+1}\big) \\ + \quad & \frac{1}{2}RJ_0^2(M)\Big(\big[2 + 2\delta_0 - \delta_{+1} - \delta_{-1}\big]\sin\psi + \big[\phi_{-1} - \phi_{+1}\big]\cos\psi\Big) \\ + \quad & \frac{1}{2}RJ_1^2(M)\Big(\big[4 + 6\delta_0 - 2\delta_{+1} - 2\delta_{-1} - \delta_{+2} - \delta_{-2}\big]\sin\psi + \big[\phi_{-2} - \phi_{+2}\big]\cos\psi\Big)\,. \end{aligned} \tag{5.17}$$

Here $J_k(M)$ denotes the kth Bessel function of M, and $(\delta_{\pm k},\ -\phi_{\pm k})$ are the absorptive and dispersive parts of the medium refractive index evaluated at frequencies $\omega_0 \pm k\omega_m$. For details of the derivation and some peculiarities concerning double-modulation techniques for the VCSEL experiments see appendix A.

Typical modulation frequencies used in the experiments were $\omega_m = 1\,\mathrm{kHz}$ for the phase-lock set-up and $\omega_m = 7.32\,\mathrm{kHz}$ for the VCSEL set-up, whereas the phase-modulation index was usually chosen as $M = 1$.

However, as evidenced in eqs. (5.16), (5.17), in FM-spectroscopy the underlying dark resonance line shapes do not directly become obvious from the experimental data. But for the evaluation of some of the experiments described in this chapter it is essential to have line shape information, for instance, for the determination of line positions and linewidths. Therefore two different procedures were used for line shape retrieval: fitting of a line shape model to the experimental spectra and a direct deconvolution algorithm. Both of these methods are necessary if a wide variety of dark resonance spectra recorded under very different conditions are to be studied because of the inherent limitations of the two procedures.

Fit If a particular line shape of the dark resonance is assumed, the parameters of this model can be adjusted for best fit to the experimental data. In order to derive suitable fit functions from eqs. (5.14), (5.15) the general expressions for both the absorptive and the dispersive parts of the refractive index have to be known. Simple analytical formulae exist under the assumption of Lorentzian profiles which in many cases also yields good agreement with the experimental data. For larger optical detunings δ_L, however, the line shapes show considerable asymmetries and thus strong deviations from simple Lorentzians. As indicated in eqs. (2.15), (2.16), in this case a reasonable approach towards the absorptive line profile is given by the sum of an absorptive and a dispersive Lorentzian profile, still with the advantage of simple expressions for the dispersive part as well. But in contrast to eqs. (2.15), (2.16), slightly different line positions

and linewidths of the two contributions had to be admitted in order to reach good agreement with the experimental spectra. This might well be accounted for by the Doppler distribution mainly influencing the term depending on δ_L. Other line shapes, such as Voigt, Gaussian or exponential profiles, are more difficult to treat with this method because the corresponding dispersive parts are not known analytically.

Numerical deconvolution For the dark resonance spectra which do not agree with any reasonable parametrized line shapes a direct numerical deconvolution algorithm was devised. The procedure is based on the fact that the signals X, Y are recorded as a set of n discrete measurements (X_i, Y_i) , $i = 1...n$. Hence eqs. 5.16, 5.17 result in a system of $2n$ linear equations which can be solved for (δ_i, ϕ_i). Details on this procedure and its limitations are given in [WYN99B] and appendix A.2. Thus it becomes possible to retrieve the underlying line shapes from the measured FM-spectra without the need to make any line shape assumptions. Unfortunately, this method does not yield reasonable results if the inevitable experimental noise gets too large. This is particularly critical if the modulation frequency ω_m is much smaller than the spectral width of the feature detected so that the sideband structure of the spectrum is completely unresolved. Still, in the limit of very small ω_m the deconvolution actually reduces to a single (for δ_i) or a double integration (for ϕ_i).

5.2.2 Line shapes in pure cesium vapour

The thermal Doppler velocity distribution tends to wash out line shape asymmetries. Nonetheless, they do remain discernible, and some dependencies of the dark resonance line shapes on beam diameter, intensity and optical detuning can readily be studied.

According to eqs. (2.15), (2.16), for $\delta_L = 0$ and a three-level atom at rest, one expects the dark resonance line shape to be Lorentzian. Despite the more complicated cesium level scheme and the Doppler distribution in the thermal vapour the resulting line shapes remain Lorentzian to a good approximation, if δ_L roughly corresponds to the 3, 4 cross-over transition, i.e., for $\tilde{\delta}_L \approx 0$, and if the beam diameter is large enough for time-of-flight broadening to be negligible.

On the other hand, when time-of-flight becomes the dominant broadening mechanism, the dark resonance line shape ceases to be Lorentzian. In [THO80] both the line shape and the width of a dark resonance dominated by time-of-flight broadening are calculated in third-order perturbation theory for copropagating laser fields and Gaussian beam profiles. For negligible Doppler broadening of the difference frequency they find exponential line shapes $\propto \exp(-|\delta_R/(\gamma_{\mathrm{CPT}}/2\ln 2)|)$ where the full width at half maximum γ_{CPT} (in Hz) for a beam diameter d (corresponding to the $1/e$ diameter of the Gaussian intensity profile) is given by

$$\gamma_{\mathrm{CPT}} = \frac{\ln 2}{\pi^2}\sqrt{\frac{kT}{m}}\frac{1}{d}\,. \tag{5.18}$$

Fig. 5.14 shows different dark resonance line shapes (standard configuration) recorded with two different laser beam diameters: $d_1 = 0.36\,\text{mm}$ for figures (a) and (b), and $d_2 = 1.05\,\text{mm}$ for figures (c) and (d). The relative intensity between master and slave laser was always 3 : 2 whereas the total intensity was roughly the same for figures (a) and (c) ($0.05\,\text{mW/cm}^2$), and figures (b) and (d) ($1.3\,\text{mW/cm}^2$ and $1.2\,\text{mW/cm}^2$ respectively). From the experimental spectra the line shapes were retrieved with the help of the numerical inversion procedure.

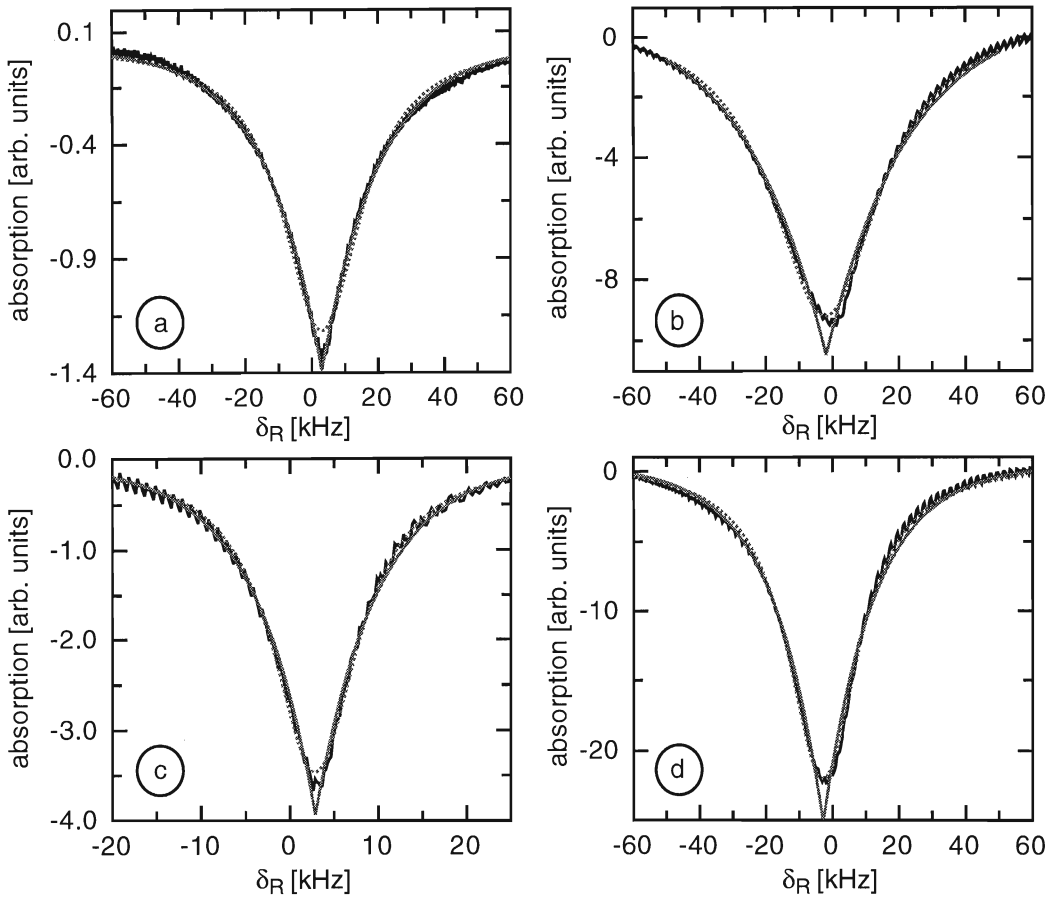

Figure 5.14: *Deconvoluted dark resonance line shapes for two different laser beam diameters d and total intensities I: (a)* $d_1 = 0.36\,\text{cm}$, $I_1 = 0.05\,\text{mW/cm}^2$, *(b)* $d_1 = 0.36\,\text{cm}$, $I_2 = 1.3\,\text{mW/cm}^2$, *(c)* $d_2 = 1.05\,\text{cm}$, $I_1 = 0.05\,\text{mW/cm}^2$, *(d)* $d_2 = 1.05\,\text{cm}$, $I_2 = 1.2\,\text{mW/cm}^2$. *The grey lines depict numerical fits under the assumption of Lorentzian profiles (dotted lines) or exponential profiles (solid line). Also note the different horizontal scales.*

In both figures the grey lines represent a numerical fit assuming Lorentzian line shapes (dotted lines) and exponential line shapes (solid lines), respectively. For low intensity and small beam diameter, i.e., dominant time-of-flight broadening (figure (a)), the dark resonance line shape shows good agreement with the exponential line profile. But as soon as saturation broadening becomes more dominant, either by increasing the beam diameter or the intensity, the line shape approaches a Lorentzian profile, as shown in figures (b) - (d). For high intensity and large beam

diameter the line shape agrees well with the Lorentzian line profile (figure (d)). For a better illustration of the change in line shape fig. 5.15 depicts the two extreme cases of figs. 5.14(a) and (d) with larger resolution around the line centre. Due to its transient nature time-of-flight broadening clearly goes beyond the theoretical model of chapter 3 based on steady-state solutions for single atoms. The lineshapes measured correspond to a steady state of the whole ensemble for which the above description does not have to be appropriate any more. In fact, dark resonance line shapes calculated according to eq. (3.10) show excellent agreement with the assumption of a Lorentzian profile.

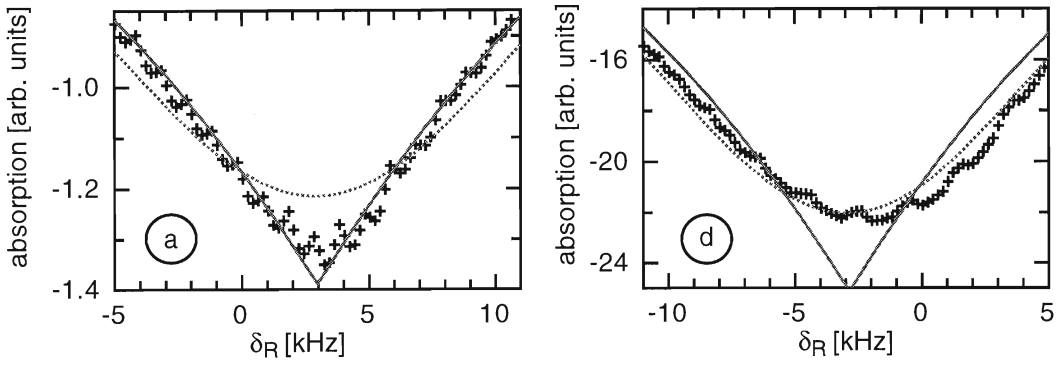

Figure 5.15: *With a better resolution around the line centre the change in line shape between figs. 5.14(a) and (d) becomes more apparent. Note that the small wiggles in the experimental curves are artifacts due to the numerical deconvolution algorithm.*

5.2.3 Line shapes in the presence of buffer gas

Using the VCSEL set-up with the standard configuration and a cesium cell containing 71 mbar of neon, the dark resonance was recorded as a function of the optical detuning of the carrier for three different overall laser intensities. In all of these measurements the relative intensity within the bichromatic field remained the same, as given by the VCSEL modulation efficiency at 9 GHz: $I_{\omega_0 \pm 9\,\mathrm{GHz}}/I_{\omega_0} \approx 1.5\%$. For carrier frequencies within the Doppler-broadened absorption profile the carrier frequency could be stabilized to various frequency positions, and its frequency was determined from the calibrated absorption signal from an auxiliary cesium cell. For frequencies well outside the absorption line in pure cesium the carrier frequency was determined from a calibration of the laser injection current as the VCSEL output frequency tunes linearly with the injection current.

Since the resulting spectra showed considerable deviations from Lorentzian profiles the numerical inversion procedure was employed in order to retrieve the underlying line shapes from the FM spectra recorded. Fig. 5.16 depicts a series of dark resonance line shapes obtained for different optical detunings δ_L and a total intensity of $0.97\,\mathrm{mW/cm^2}$. According to eq. (3.11), for a neon pressure of 71 mbar the optical transition is shifted by about $-250\,\mathrm{MHz}$ and broadened to about

610 MHz, i.e., the hyperfine structure of the excited state cannot be resolved anymore. The optical detuning δ_L is defined as in section 3.4.2, i.e., not taking into account the buffer gas shift of the optical transition.

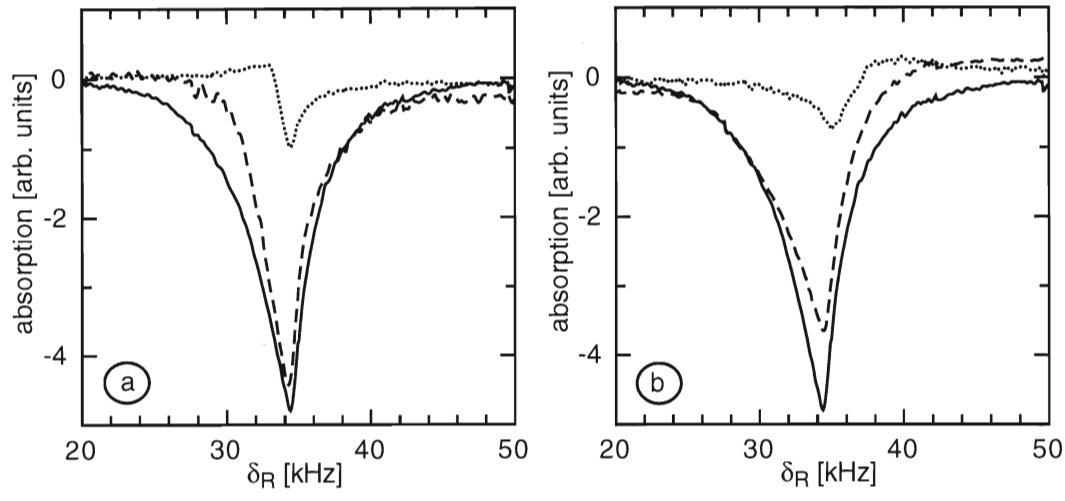

Figure 5.16: *Line shapes of CPT resonances (71 mbar neon, standard configuration, total intensity 0.97 mW/cm^2) for various optical detunings δ_L, retrieved from the measured FM spectra via the numerical inversion procedure: (a) $\delta_L = 0$ (solid line), $\delta_L = -296$ MHz (dashed line), $\delta_L = -780$ MHz (dotted line), (b) $\delta_L = 0$ (solid line), $\delta_L = 134$ MHz (dashed line), $\delta_L = 430$ MHz (dotted line). Obviously the asymmetry of the line shapes follows the optical detuning δ_L: increasing $|\delta_L|$ results in increasing asymmetry while the orientation of the asymmetry is determined by the sign of δ_L.*

For a comparison with theory the dark resonance line shape was calculated according to section 3.4.2. Since a detailed theoretical analysis of the complex interplay between Doppler-broadening and the Lamb-Dicke effect in the presence of buffer gas has not yet been performed for CPT resonances, it is not obvious how to include Doppler-shifts into the model. Therefore fig. 5.17 depicts two opposite approaches. Whereas figs. 5.17(a),(b) were obtained in that the Doppler-integration was applied to the optical frequencies only, figs. 5.17(c), (d) include the complete Doppler-integration. The parameters used in both cases were: intensity $I = 1\,\mathrm{mW/cm^2}$, $\gamma_{12} = \Gamma_{12} = 50\,\mathrm{Hz}$, $\gamma_0 = \gamma_1 + \gamma_2 = 600\,\mathrm{MHz}$, $\Gamma_1 = \Gamma_2 = \gamma_0/2$. The detunings were chosen the same as in the experiment, i.e., for figs. 5.17(a), (b): $\delta_L = 0$ (solid line), $\delta_L = -296\,\mathrm{MHz}$ (dashed line), $\delta_L = -780\,\mathrm{MHz}$ (dotted line), and for figs. 5.17(c), (d): $\delta_L = 0$ (solid line), $\delta_L = 134\,\mathrm{MHz}$ (dashed line), $\delta_L = 430\,\mathrm{MHz}$ (dotted line). In order to reproduce the experimentally recorded linewidth one had to insert an extra factor of 0.5 into the calculation of the squared Rabi frequencies according to eq. (3.45) which is still reasonable in the face of the rough approximation of the laser beam intensity profile. γ_0 is calculated from eq. (3.11) for the neon pressure used in the experiment, and the values for γ_{12}, Γ_{12} roughly correspond to the minimum linewidths reached for this buffer gas pressure. Yet, the choice for these parameter is not critical at all, the calculated line shapes hardly change if γ_{12}, Γ_{12} are set, e.g., equal to zero. Comparison of these calculated line shapes with the experimental ones of fig. 5.16 shows better than purely qualita-

tive agreement. General dependencies on δ_L such as line asymmetries increasing with δ_L or the reversal of the asymmetry with a sign change of δ_L are exhibited already by the most simple approach of an atom at rest (see fig. 2.3). But apart from that, reasonable agreement concerning relative amplitudes and asymmetries is in fact reached for realistic parameters. Nevertheless, more subtle details cannot be reproduced by this simple model, e.g., the experimentally recorded line shapes appear to be less asymmetric than the calculated ones. Furthermore, exact agreement cannot be reached for either treatment of Doppler shifts. For instance, for large δ_L the asymmetries in figs. 5.17(a),(b) are too pronounced whereas figs. 5.17(c), (d) do not correctly account for the reduction of linewidths for increasing δ_L. Apart from the problem with Lamb-Dicke narrowing mentioned above, a more sophisticated model will also have to pay attention to multilevel effects such as spontaneous decay from adjacent Zeeman levels into the system, and to the influence of the large VCSEL linewidth. Using the simple model, the line shape dependence on γ_i, Γ_i, $i = 1, 2$, is not very critical as long as γ_i, Γ_i are not much smaller than the Doppler-width. The agreement only slightly deteriorates if these parameters are changed, e.g., by a factor of 2.

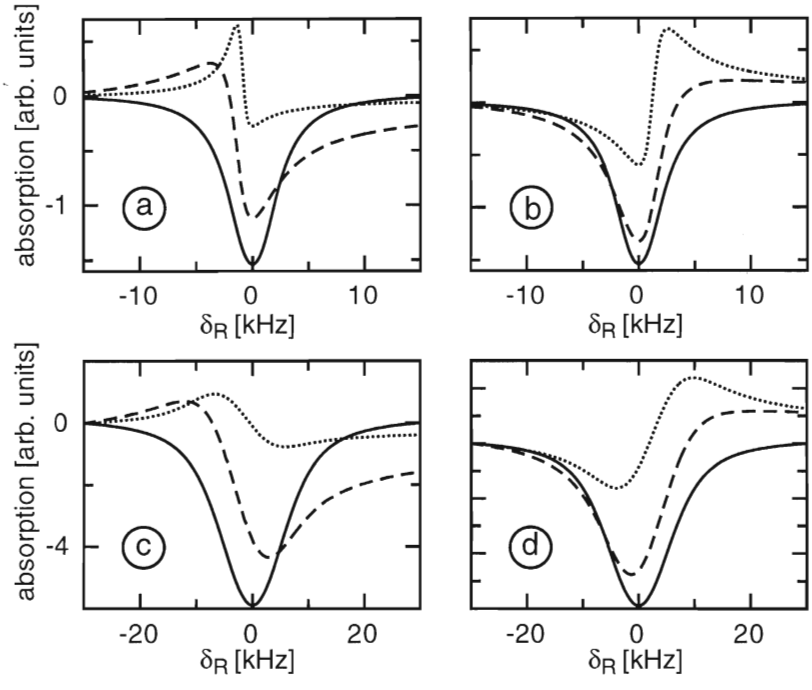

Figure 5.17: *Line shapes of CPT resonances as a function of δ_L calculated according to the model described in section 3.4.2. (a), (b): without Doppler-integration for the 9 GHz difference frequency; (c), (d): with complete Doppler-integration. Parameters correspond to the experimental situation of fig. 5.16.*

For fixed δ_L the line shape asymmetry dependence on the optical relaxation and dephasing rates can only be revealed if γ_i, Γ_i are changed enormously. In principle, the larger γ_i, Γ_i, the less the influence of the Doppler integration on the CPT line shape, because the dark resonance contrast starts getting suppressed only for optical detunings that are of the same order of magnitude as

the optical relaxation rates. Hence, for a given optical detuning the Doppler integration might almost completely wash out line shape asymmetries in pure cesium vapour whereas the line shape asymmetry is well visible in a buffered cell.

CPT line shape asymmetries have been observed before, although with much lower precision and for experimental configurations that were essentially Doppler-free, for instance in an atomic beam experiment [KAI85] or for a single trapped and cooled ion [SIE92].

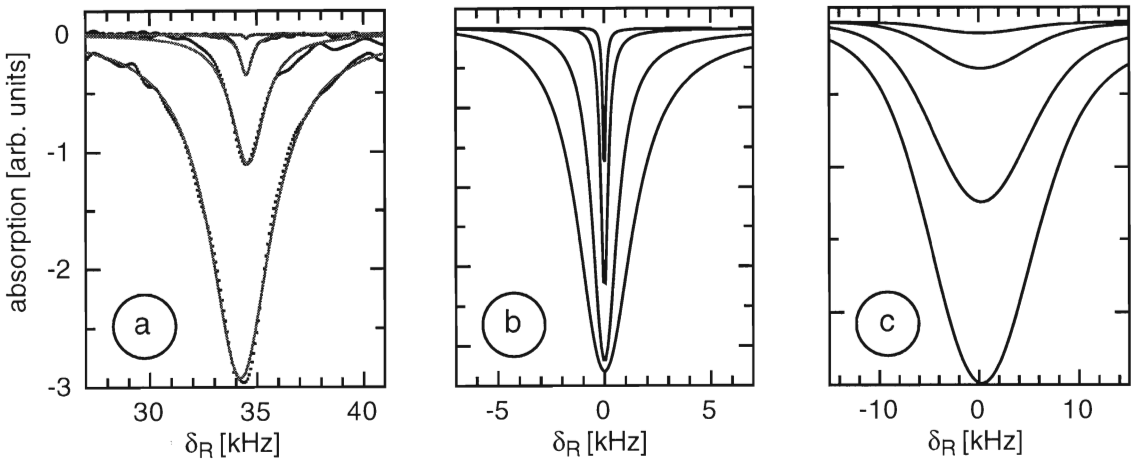

Figure 5.18: *Dark resonance line shapes for various laser intensities (I = (0.97, 0.44, 0.1, 0.023) mW/cm^2):*
(a) Experimentally measured line shapes, optical detuning δ_L=−89 MHz (dots). The grey solid lines represent fitted Lorentzian line profiles which agree well with the experimental line shapes.
(b) Calculated line shapes according to eq. (3.48)*, i.e., neglecting Doppler-broadening of the* 9 *GHz frequency.*
(c) Calculated line shapes according to eq. (3.10)*, i.e., ignoring possible Lamb-Dicke narrowing.*
Parameters used for the line shapes in (b), (c) were: δ_L=−40 MHz, $\gamma_0 = \Gamma_i$ = 600 MHz, $\gamma_{12} = \Gamma_{12}$ = 50 Hz, and an additional factor of 0.5 *for the Rabi frequencies.*

Fig. 5.18(a) depicts a series of dark resonance line shapes as a function of intensity, retrieved from measurements with the modulated VCSEL set-up, the standard configuration, 72 mbar neon, and optical detuning δ_L=−89 MHz. Lorentzian profiles fitted to the experimental data exhibit quite good agreement for all intensities. Hence, at least for this particular value of δ_L, changing the intensity does not result in a change in line shape but only in a decrease in amplitudes and linewidths. Figs. 5.18(b) and (c) show dark resonance line shapes calculated according to eqs. (3.48) and (3.10), respectively. The parameters used correspond to the situation of fig. 5.18(a): δ_L=−40 MHz, $\gamma_0 = \Gamma_i$ = 600 MHz, $\gamma_{12} = \Gamma_{12}$ = 50 Hz, and an additional factor of 0.5 for the Rabi frequencies. Again, according to the discussion above, the choice of parameters is reasonable. The value of δ_L=−40 MHz, chosen in order to account for the slight asymmetry of the line shapes, appears to be consistent with the experimental uncertainty in this value of about 70 MHz. But, from eq. (3.11) one expects the optical resonance to be shifted by about −250 MHz, such that symmetrical line shapes could be expected for $\delta_L \approx -250$ MHz because

in the experiment the value of δ_L is always obtained from the auxiliary cesium cell which does not contain any buffer gas. This discrepancy cannot be explained yet. The agreement between the additional intensity factors of 0.5 needed for both the calculations illustrated in figs. 5.17 and 5.18 again suggests that its origin is systematic, e.g., due to the rough approximation of the laser beam intensity profile (also see the discussion in section 5.6). Comparison of figs. 5.18(b) and (c) leads to a similar conclusion as fig. 5.17 in that different features of the curves are modelled correctly by either treatment of Doppler broadening. Whereas completely ignoring the Doppler broadening at 9.2 GHz yields correct linewidths (fig. 5.18(b)) but wrong relative line strengths as a function of intensity, the situation is reversed in fig. 5.18(c). Completely ignoring the Lamb-Dicke effect yields correct line strengths but hardly any change in linewidth.

5.3 Buffer gas

5.3.1 Time-of-flight broadening

In pure cesium cells for low enough intensity the main broadening mechanism for the dark resonance is time-of-flight broadening. This becomes obvious from fig. 5.19 where for pure cesium vapour the dark resonance linewidth in the limit of zero intensity clearly depends on the laser beam diameter. From a linear regression fit also shown in the figure one obtains the same slope characterizing the saturation broadening behaviour but different minimum linewidths of $\gamma_{\mathrm{CPT}}^{(1)} = (4.9 \pm 0.2)\,\mathrm{kHz}$ and $\gamma_{\mathrm{CPT}}^{(2)} = (2.05 \pm 0.05)\,\mathrm{kHz}$ for beam diameters of $d_1 = 0.36\,\mathrm{cm}$ and $d_2 = 1.05\,\mathrm{cm}$, respectively.

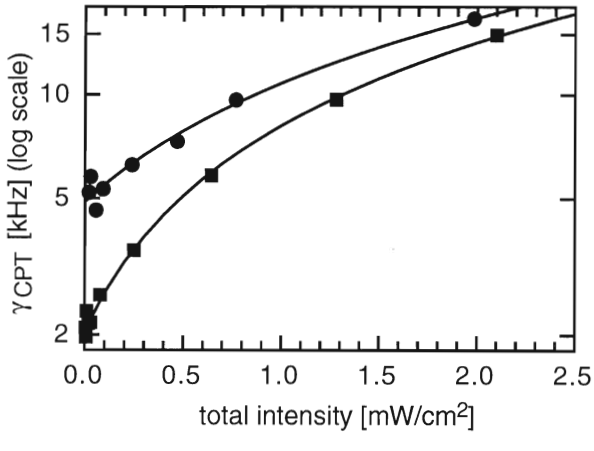

Figure 5.19: *Linewidths of the* $0-0$ *CPT resonance as a function of the total laser intensity for elliptical polarizations and two different beam diameters d:* $d_1 = 0.36\,cm$ *(circles) and* $d_2 = 1.05\,cm$ *(squares). Linear regression fits yield identical slopes but different minimum intensities. Relative laser intensities were* $3:2$.

From eq. (5.18) and for $d \approx 1\,\mathrm{cm}$ one expects a minimum linewidth of about 6 kHz. The discrepancy to the experimental value might originate in the approximations made in [Tho80],

for instance, using third order perturbation theory only, assuming initial conditions of $\rho_{11} = 1$, and neglecting Doppler shifts of the 9.2 GHz difference frequency. Similarly, according to eq. (5.18) one expects $\gamma^{(2)}_{\mathrm{CPT}}/\gamma^{(1)}_{\mathrm{CPT}} = d_1/d_2$, whereas the experimental results give $\gamma^{(2)}_{\mathrm{CPT}}/\gamma^{(1)}_{\mathrm{CPT}} = (0.42 \pm 0.02)$ and $d_1/d_2 = 0.34$.

As discussed in chapter 3.1, in order to both eliminate time-of-flight broadening and to profit from Lamb-Dicke narrowing independent of the vapour cell dimensions a buffer gas technique was chosen for the experiments of this thesis.

5.3.2 CPT in the presence of buffer gas

Buffer gas techniques also originate from the time of early optical pumping experiments: adding several mbar of an inert gas to the cesium vapour strongly impedes the free motion of the cesium atoms due to frequent collisions with the buffer gas atoms. Hence the atomic motion can be described as a diffusion process, and the effective interaction time with the light field is increased by several orders of magnitude.

Although high gas kinetic cross sections are favourable for efficient confinement of the cesium atoms within the lasers beams it has to be taken into account that the collisions do not leave the internal atomic degrees of freedom unperturbed but also give rise to relaxation processes. Many experiments have been performed in connection with optical pumping experiments as discussed in review articles [HAP72, WAL97].

Apparently the dominant collisional relaxation processes can arise from sudden binary collisions. Since these collision occur during time intervals of the order of only 10^{-12} s the influence of external fields or hyperfine interaction on the electronic polarization during the collisional process is negligibly small. Therefore it is predominantly the electronic spin that is disturbed by collisions. For the cesium-neon combination used here it has been shown that transfer between the finestructure doublets $P_{3/2}$ and $P_{1/2}$ does not play an important role such that relaxation mainly occurs within the D_2 level configuration. Excited state depolarization cross sections are found to be of the same order of magnitude as the gas kinetic cross sections or even larger. For the cesium-neon combination experimental values of 29 Å^2 were found for the $P_{3/2}$ state in contrast to about 10^{-7} Å^2 for the ground state ([HAP72] and references therein). Hence on average an atom undergoes 10^7 collisions before its ground state coherence is destroyed.

Many of the basic phenomena experimentally observed in collisional ground state relaxation can be described with the help of the following Hamiltonian:

$$H_{\mathrm{int}} = \hbar\delta A(r)\vec{I}\cdot\vec{J} + \gamma(r)\vec{N}\cdot\vec{J} \tag{5.19}$$

where $\vec{I}$ and $\vec{J}$ are the total nuclear and electronic spins of the cesium atom and $\vec{N}$ is the relative translational angular momentum between the cesium and the neon atom. The first term in eq. (5.19) represents a change in hyperfine coupling due to the presence of the colliding partner.

When the atoms are far apart $\delta A(r)$ basically consists of an attractive electrostatic Van-der-Waals potential. Hence $\delta A(r)$ is negative and the electron tends to be pulled away from the cesium nucleus thus decreasing the strength of the hyperfine interaction. For small interatomic separations the interaction potential is dominated by exchange forces between the valence electrons of the two atoms resulting in repulsive forces, hence positive $\delta A(r)$ and increased hyperfine interaction. In total, a shift of the hyperfine splitting results which is either positive or negative depending on which of the two processes is the dominant one. Whereas for the light noble gas atoms He and Ne the exchange interaction dominates the situation is reversed for the heavier species Ar, Kr and Xe. As the polarizability of the noble gas atoms increases so does the contribution of the Van-der-Waals interaction. Hence the observed pressure shifts of the cesium ground state hyperfine splitting are positive for He and Ne but negative for all of the heavier noble gases [HAP72]. The average pressure shift is given by

$$\delta\nu = \langle\delta A\rangle(I + \frac{1}{2})\frac{\tau_c}{\tau_f} \tag{5.20}$$

where $\langle\delta A\rangle$ denotes the average change in hyperfine interaction during a collision, τ_c the duration of a collision and τ_f is the mean time between collisions. Since τ_f is inversely proportional to the buffer gas pressure one expects linear pressure shifts which is in fact in agreement with experimental results. Even if $\langle\delta A(r)\rangle$ is too small to induce considerable population transfer between the hyperfine states it might nevertheless contribute not only towards pressure shifts but also towards collisional broadening. In this case the broadening would result from different phase shifts experienced by the atoms during a collision, the net effect of which is line broadening.

However, experimental results suggest that the main broadening mechanism stems from the spin-orbit interaction described by the second part of the Hamiltonian in eq. (5.19). The coupling between the electronic and translational angular momenta during the collision causes a very fast polarization randomization of the electron. Inspecting the depolarization cross sections for the noble gases [HAP72] again a tendency becomes apparent: the heavier the atom the larger the cross section because of their increasing polarizability.

As the same ground state levels are involved both in dark state preparation and microwave transitions at 9.2 GHz one expects the dark resonance shift to reproduce former results from microwave experiments.

The linewidth γ_{CPT} of the dark resonance as a function of buffer gas pressure, on the one hand reduced by longer interaction times due to the diffusive motion of the atom, but on the other hand increased by collisional interactions as described above, can be understood with the help of a diffusion equation [VAN89, BRA96], finally yielding the dephasing rate as

$$\Gamma_{12} = \Gamma_{\mathrm{diff}} + \Gamma_{\mathrm{coll}}\,. \tag{5.21}$$

One has $\Gamma_{\mathrm{diff}} \propto D$, where $D = D_0 p_0/p$ is the diffusion constant of ground state cesium atoms in neon at neon pressure p depending on the respective value D_0 at atmospheric pressure p_0. Γ_{coll}

denotes the collisional relaxation rate. If the dominant contribution towards relaxation stems from binary collisions the relaxation rate Γ_{coll} must be proportional to the number of colliding partners, i.e., the number density of buffer gas atoms: $\Gamma_{\text{coll}} = n\sigma_{\text{coll}}\bar{v}$. Under simplifying assumptions and using the experimentally determined values $D_0 = (0.153 \pm 0.014)\,\text{cm}^2/\text{s}$ and $\sigma_{\text{coll}} = (9.27 \pm 0.90) \cdot 10^{-23}\,\text{cm}^2$ [BEV71] (where the latter roughly agrees with the more recent calculations as reviewed in [WAL97]) the expected dependence of the dark resonance FWHM $\gamma_{\text{CPT}} \approx 2\Gamma_{12}$ (eq. (2.20) in the low intensity limit) on the neon pressure p reads:

$$\gamma_{\text{CPT}} = 1.3 \cdot 10^3 \frac{\text{mbar}}{\text{s}} \cdot \frac{1}{p} + 0.4 \cdot \frac{1}{\text{s} \cdot \text{mbar}} \cdot p\,. \tag{5.22}$$

According to section 3.1 the contribution of ground state relaxation and dephasing rates due to Cs-Cs collisions, $\gamma_{\text{Cs-Cs}}$ and $\Gamma_{\text{Cs-Cs}}$ respectively, is also of the order of several Hz and thus not necessarily negligible any more. Since the temperature was always kept constant one basically expects a further offset for γ_{CPT}. A more rigorous treatment would also have to take into account that eq. (2.20) is a rather rough approximation only and that the dark resonance linewidth generally depends in a more complicated manner on both $\gamma_{\text{Cs-Cs}}$ and $\Gamma_{\text{Cs-Cs}}$. For spin exchange processes (SE) the two rates are given by

$$\begin{aligned} \gamma_{\text{Cs-Cs}} &= n\bar{v}\sigma_{\text{SE}} \\ \Gamma_{\text{Cs-Cs}} &= Rn\bar{v}\sigma_{\text{SE}}\,, \end{aligned} \tag{5.23}$$

with $R = (6I + 1)/(8I + 4)$ according to [VAN89]. But due to considerable discrepancies in the literature values for σ_{coll} one cannot expect to discern these additional influences here and therefore only γ_{CPT} according to eq. (5.22) is taken into account.

In total, while for buffer gas pressures in the mbar range Cs-Ne collision hardly broaden the dark resonance line they have a dramatic effect on the optical transition. Estimates of the corresponding broadening and shift rates were given in eq. (3.11).

5.3.3 Experimental results

From the experimentally determined values of cross sections for cesium-noble gas combinations [HAP72] neon appeared as a promising species to be used as a buffer gas with high enough gas kinetic and low enough ground state relaxation cross sections. The experimental study of the dark resonance as a function of neon pressure was performed with the help of a cesium cell sealed by a glass valve. Hence different buffer gas pressures could be realized one after the other. The standard configuration was used, the intensity of the master and slave laser beams was kept at a constant ratio of 3 : 2, and the master laser was stabilized near the 3, 4 crossover transition. For each buffer gas pressure a series of measurements was carried out in that the $0-0$ resonance was recorded as a function of intensity. An FM-AM absorptive Lorentzian profile (see section 5.2.1) was fitted to each spectrum to determine its line centre and width.

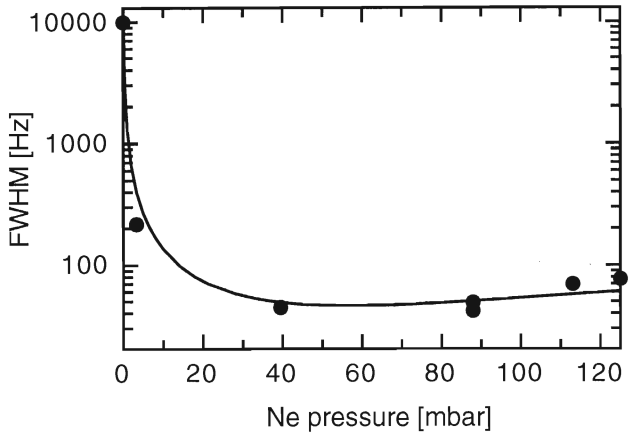

Figure 5.20: *Full width at half maximum of the* $0-0$ *component as a function of neon buffer gas pressure: experimental data (circles) and a zero parameter theoretical curve (solid line).*

In fig. 5.20 the fitted FWHM is plotted against the buffer gas pressure, together with the theoretical curve given in eq. (5.22). For a zero parameter curve the agreement with the experiment is excellent. However, this agreement must not be overestimated because of the uncertainties in the cross section measurements. Since in principle the dark resonance considerably suffers from saturation broadening (see section 5.6) the experimental values present in fig. 5.20 correspond to a total intensity as low as $10\,\mu\mathrm{W/cm^2}$, i.e., about 1 % of the optical saturation intensity.

The smallest dark resonance linewidth recorded so far is only 42 Hz. Fig. 5.21 shows both the absorptive and the dispersive part of the spectrum obtained from the numerical inversion of the experimentally recorded spectra.

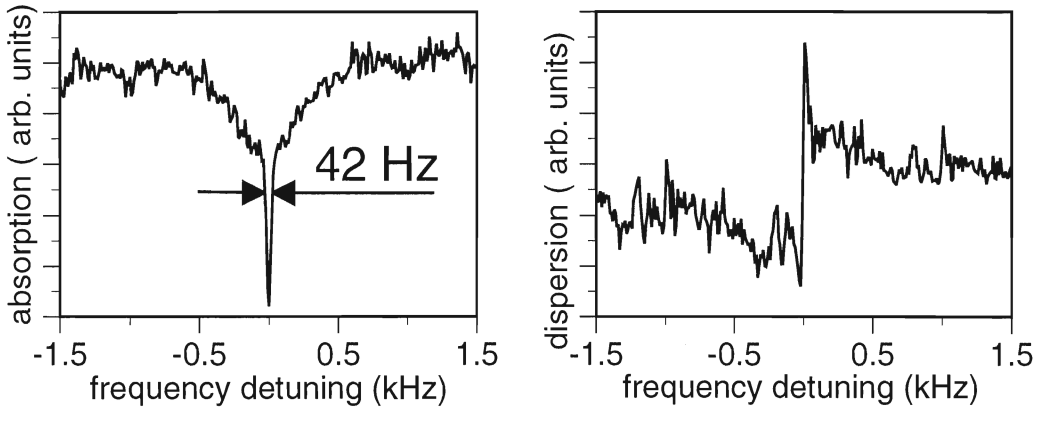

Figure 5.21: *Absorptive and dispersive part of a dark resonance line with only* 42 Hz *full width at half maximum. The pedestal resulted from line interferences at multiples of* 50 Hz *in the phase-locked loop.*

For each buffer gas pressure the line centre frequency was extrapolated to zero laser intensity in order to correct the results for the intensity dependent shift. Fig. 5.22 depicts the buffer gas induced shift of the dark resonance. A straight line fit yielded a shift rate of (480 ± 10) Hz/mbar

[BRA97] which is in agreement with a value of (452 ± 20) Hz/mbar determined for the corresponding microwave transition [BEV81]. Note that the error given for the dark resonance shift results from the fit only. In principle spurious impurities present in the vacuum chamber used to refill the cell could have a considerable influence which was completely neglected here.

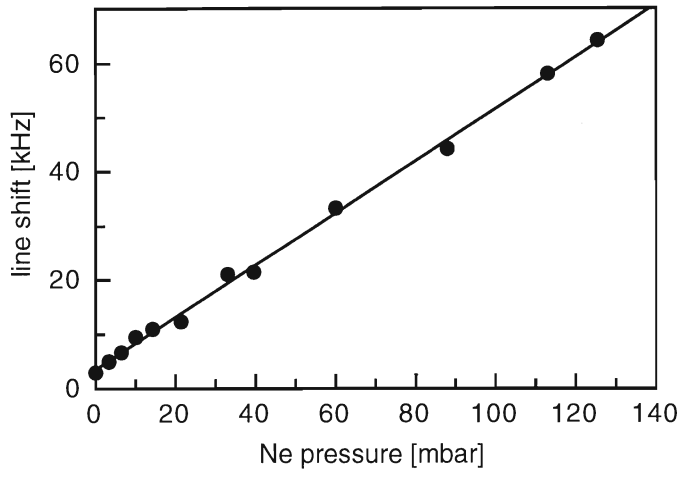

Figure 5.22: *Position of the* $0-0$ *dark resonance component extrapolated to zero intensity as a function of neon buffer gas pressure.*

As discussed above, the use of heavier noble gases would result in a negative pressure shift of the dark resonance, therefore a suitable combination of different buffer gases is expected to even cancel the pressure shift. However, as it will be discussed in chapter 6, precision measurements might require the use of a cesium/rubidium combination to compensate other frequency shifting effects. This further complicates the search for an ideal buffer gas combination cancelling or at least reducing the shift for both species with minimum broadening of the line.

5.4 AC-Stark shift

5.4.1 AC-Stark shift in pure cesium vapour

According to the theory presented in chapter 3.4 the dark resonance line centre is expected to depend on laser intensities due to the AC-Stark shift. Although the measurable net effect is expected to be washed out by the thermal Doppler distribution residual intensity dependence was readily detected.

The phase-lock set-up was used to measure the dark resonance position as a function of laser intensity for the standard configuration. The relative intensity of master and slave lasers was kept at a constant ratio of 3 : 2 whereas the total intensity was changed from $10\,\mu\mathrm{W/cm^2}$ to $1.9\,\mathrm{mW/cm^2}$ with the help of variable attenuators. In order to retain the same overall power

on the photo diode the sum of attenuators always remained the same in that attenuators were simply moved from the front to the back of the cesium cell. For all measurements the master laser was stabilized near the 3, 4 crossover transition on the absorption line involving the ground state $F = 4$ level. From the fit of an FM-AM line profile to each spectrum the line centre could be determined with typically a few Hz uncertainty. According to the discussion of dark resonance line shapes in chapter 2.2 the underlying line profile was assumed as the sum of an absorptive and a dispersive Lorentzian. Despite the precision of a few Hz it has to be noted that the absolute value of the dark resonance centre frequency could only be determined with an accuracy of a few kHz, due to the specifications of the frequency standard available. Therefore, a constant offset between experimental and theoretical values has no significance here and such an offset can be added to the theoretical curves so as to provide the best fit.

Fig. 5.23 shows the resulting line centre dependence on intensity together with theoretical curves according to the model developed in chapter 3.4, where the value $\Gamma_{12} = 4.2\,\text{kHz}$ was taken from the treatment of saturation broadening in section 5.6.

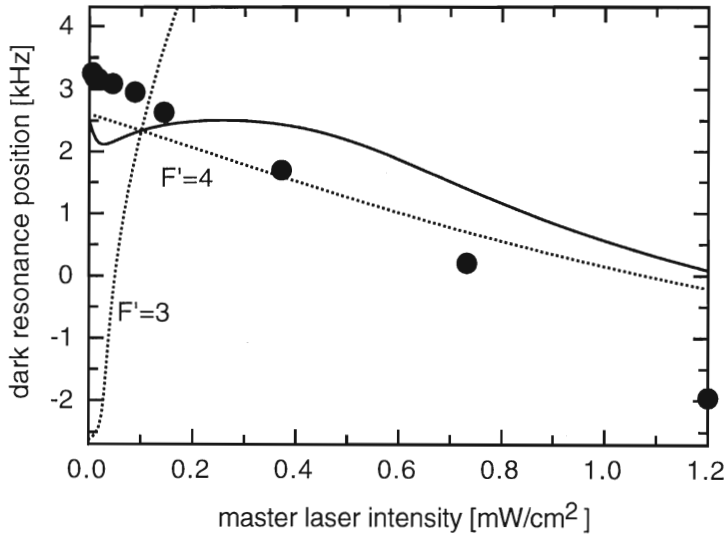

Figure 5.23: *AC-Stark shift of the dark resonance: line centre as a function of intensity where the solid circles represent the experimental results. The solid line is calculated with the parameter values taken from the experiment (under the additional assumption of $\gamma_{12} = \Gamma_{12}$) and the dotted lines correspond to calculations taking into account only one of the excited states.*

Although the zero parameter calculated Stark shift curve (solid line) roughly gives the correct order of magnitude it considerably differs from the data derived from the experiment. The latter intensity dependence appears basically linear, resembling the behavior of a two-level system under monochromatic illumination, whereas the calculated curve shows a more complicated behaviour. This nonlinear behaviour can at least be qualitatively understood with the help of the dotted curves that were calculated taking only one of the excited states F'=3 and F'=4 into account. As the optical detuning is positive with respect to the ground state $F = 3$ level, but negative with respect to the $F = 4$ level the respective light shift rates are opposed to each other.

Since the coupling strengths are different, as well, the shape of the two curves also differs. In the experiment only the superposition of the two upper state contributions is observable, hence each point on the total curve (solid line in fig. 5.23) corresponds to the minimum of a dark resonance line shape superposition with contributions from both excited states. From eq. (3.43) one calculates that the coupling strength for the Λ-system involving the upper state $F' = 4$ is about a factor of three stronger than that for the upper state $F' = 3$. Therefore it comes as no surprise that the resulting curve in fig. 5.23 is closer to the $F' = 4$ contribution than to the $F' = 3$ contribution, although for a detailed description it is essential to include both of them. Hence the remarkable shape of the total curve reflects the incoherent addition of the two excited states' contribution. Small deviations of the experimental curve from a straight line might show this very behaviour although the effect is hardly visible.

When varying the parameters used in the calculation the resulting curves retain the same general shape but exhibit both different slopes and shifted maxima which might also be more or less pronounced.

Slightly better agreement could only be reached with the help of rather arbitrary alterations, in that the light shift curves for the F'=3 and F'=4 transitions were calculated separately, using slightly changed parameter values, and the total curve was given as the weighted sum of the two contributions, with the weighting factor chosen for best fit. In doing so, different choices of parameters could effectively result in nearly the same theoretical curves. The introduction of such phenomenological factors cannot be justified within the theoretical model described so far because different weights of the two contributions should principally be accounted for by different coupling strengths and optical detunings only. Nevertheless, the need for such additional factors might result from loss mechanisms due to optical pumping to atomic states not involved in dark state preparation. Therefore altered population balances might be considered as yet another relevant aspect (also see the discussion in section 5.5).

Furthermore, it is not obvious, to what extent changes of parameters might be justified as an effective treatment of experimental influences that have not been included into the calculation explicitly, such as the Gaussian transverse laser beam profile or time-of-flight broadening. For instance, it has not yet been investigated in enough detail, to what extent time-of-flight broadening can be accounted for by stationary density matrix solutions with effective decay rates γ_{12}, Γ_{12}, and whether the intuitive assumption of $\gamma_{12} = \Gamma_{12}$ is correct.

In total, although a certain understanding of the dark resonance light shift can be gathered from the comparison with the theoretical model, the complicated experimental situation can so far not be modelled with the help of the simple approach discussed here.

5.4.2 AC-Stark shift in the presence of buffer gas

A most welcome side-effect of a buffer gas is the concomitant reduction in the AC-Stark shift. For high enough intensity the AC-Stark shift is approximately a linear function of intensity, therefore for each buffer gas pressure a straight line was fitted to the data, the slopes of which are shown in fig. 5.24. Apparently, a few mbar of neon are sufficient to produce a dramatic decrease in slope, whereas a further increase of the buffer gas pressure does not lead to additional effects discernible in the linear approximation. The strong dependence on buffer gas pressure at low pressures resembles the behaviour found for the dark resonance linewidth (section 5.3.3) and saturation broadening (section 5.6). As this behaviour is attributed to collisional interaction with the buffer gas atoms it goes well beyond the simple three-level model description. For the precision measurements envisioned the decrease in AC-Stark shifts is yet another favourable aspect because it reduces effective line broadening or shifts due to intensity fluctuations.

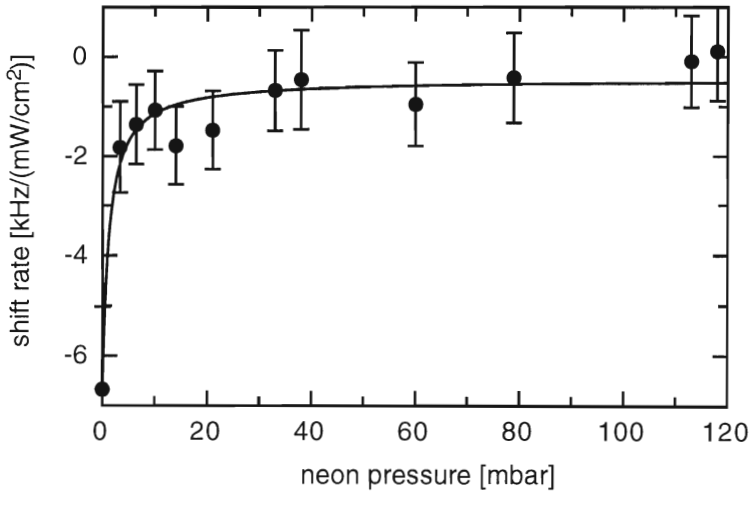

Figure 5.24: *Slope of the linear approximation for the AC-Stark shift rate as a function of buffer gas pressure. The solid line represents a phenomenological* $1/p_{\mathrm{Ne}}$ *fit.*

5.5 Optical detuning

Due to the AC-Stark effect the dark resonance position does not only depend on intensity but also on the optical detuning. With the VCSEL set-up, a cell with 72 mbar neon, and the standard configuration, the dark resonance position δ_{CPT} was determined as a function of the optical detuning for different intensities, where δ_{CPT} was defined as the minimum of the absorption profile. The results for intensities $I_1 = 0.97\,\mathrm{mW/cm^2}$ and $I_2 = 0.44\,\mathrm{mW/cm^2}$ are shown in fig. 5.25(a), (b). Solid circles always correspond to the experimental situation where the carrier near-resonantly interacts with the $F = 4$ transition and dark states are prepared with the carrier and the +1st-order sideband. In contrast, the open circles show the results for dark state preparation with the carrier and the −1st-order sideband, i.e., in this configuration the carrier is near resonant with the $F = 3$ transition. In all of the experiments the two sidebands could be characterized as either mainly contributing towards dark state preparation or as far off-resonant. For the interesting configuration where the detuning of both sidebands was roughly equal, i.e., for a carrier detuning near 4.5 GHz, the S/N ratio was too poor to record dark resonance spectra and investigate the behaviour in the presence of such a third frequency component.

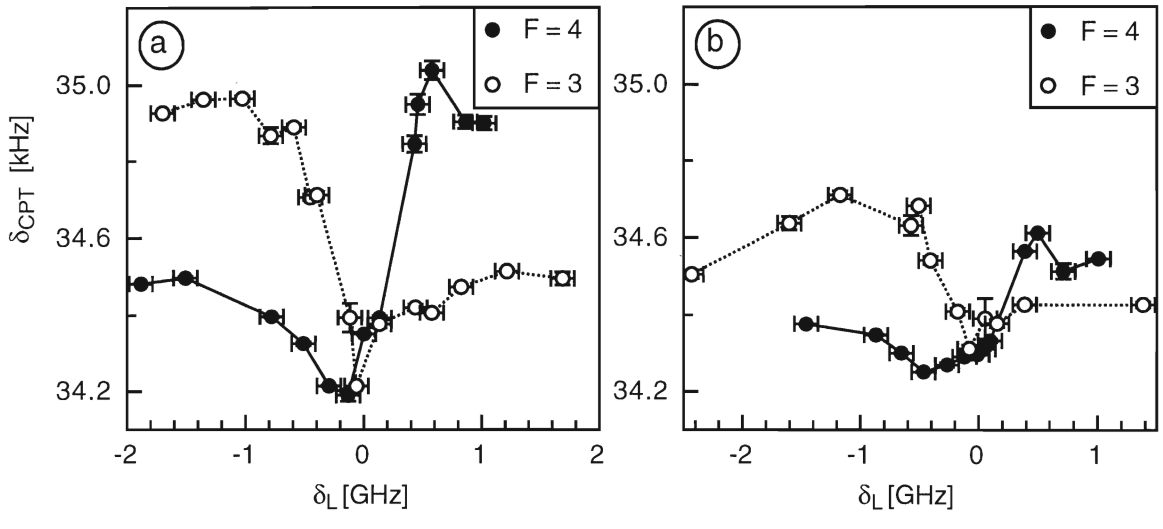

Figure 5.25: *CPT resonance position δ_{CPT} as a function of the optical detuning δ_L: (a) intensity $I_1 = 0.97\,\mathrm{mW/cm^2}$, (b) intensity $I_2 = 0.44\,\mathrm{mW/cm^2}$. Dark resonances were prepared with the carrier frequency near-resonant with the $F = 4$-component and the +1st-order sideband (solid circles), or with the carrier frequency near-resonant with the $F = 3$-component and the −1st-order sideband (open circles). Measurement points are connected to guide the eye.*

For the discussion of fig. 5.25 it has to be kept in mind that the dark resonance is shifted due to the presence of the buffer gas according to fig. 5.22. Uncertainties concerning the buffer gas pressure do not allow to determine the buffer gas shift with better than a few kHz accuracy, therefore it is not possible to define $\delta_{\mathrm{CPT}} = 0$ in fig. 5.25. However, since the buffer gas pressure was kept constant, the frequency offset is the same in all cases.

The functional dependence of the dark resonance position on optical detuning is roughly point-symmetric and a comparison of figs. 5.25(a) and (b) shows that for each of the two configurations (i.e., solid and open circles) within the rather large errors for δ_L this symmetry does not depend too crucially on intensity. An inspection of eq. (3.47) reveals that $n''(\delta_L, \delta_R)$ is invariant under the transformation $(\delta_L, \delta_R) \mapsto (-\delta_L, -\delta_R)$. Hence the simple three-level model in fact predicts point symmetry for the dark resonance position dependence on δ_L, as it was demonstrated in fig. 2.5 as well. But the model developed in section 3.4.2 does not yield curves for which the characteristic dependence of δ_{CPT} on the optical detuning is of the correct order of magnitude. Furthermore, the fact that the symmetry points for the two configurations are shifted by several hundreds of MHz cannot be explained with the help of a simple three-level model. Hence the experimentally recorded shifts might originate not only in the AC-Stark shift. Fitting dispersive Lorentzians to the curves of fig. 5.25 yields for the optical detuning of the symmetry points δ_L^{pos}:

$$\begin{aligned}
&\text{(a) } \delta_L^{(\mathrm{pos,a})} = +220 \pm 40\,\mathrm{MHz}, \quad \text{(b) } \delta_L^{(\mathrm{pos,b})} = +177 \pm 41\,\mathrm{MHz} \quad \text{for the solid circles and} \\
&\text{(a) } \delta_L^{(\mathrm{pos,a})} = -490 \pm 36\,\mathrm{MHz}, \quad \text{(b) } \delta_L^{(\mathrm{pos,b})} = -420 \pm 46\,\mathrm{MHz} \quad \text{for the open circles.}
\end{aligned} \tag{5.24}$$

Comparison with the cesium level scheme of fig. 3.1 reveals an interesting feature of these shifts. From an intensity average one gets a frequency interval of 653 ± 41 MHz between the solid and open circles curves, which is roughly equal to the maximum hyperfine splitting of the excited state. Hence one can suppose that for large enough optical detuning all of the excited state hyperfine components might play a major role for the CPT resonance dependence on δ_L, even the $F' = 2, 5$ levels which have not been taken into consideration explicitly so far. Since these effects appear to be hardly affected by intensity, it is well justified to treat intensity and detuning dependence independently of each other.

In order to further characterize the influence of the optical detuning both the CPT linewidth and amplitude were considered. Fig. 5.26 shows the functional dependence of the linewidth on δ_L for two different intensities, where the notation is the same as in fig. 5.25.

Apart from the character of the curve's symmetry (axial symmetry instead of point symmetry, again as expected at least qualitatively from fig. 2.5) the main features of the functional dependence on the optical detuning correspond to the behaviour of the line position in fig. 5.25. Again, the symmetry of the curves roughly resembles the behaviour expected for a three-level system, whereas the symmetry point shifts between the two curves clearly does not. Fitting absorptive Lorentzian profiles to all curves yields for these symmetry points δ_L^{FWHM}:

$$\begin{aligned}
&\text{(a) } \delta_L^{(\mathrm{FWHM,a})} = +143 \pm 45\,\mathrm{MHz}, \quad \text{(b) } \delta_L^{(\mathrm{FWHM,b})} = +165 \pm 43\,\mathrm{MHz}, \quad \text{for the solid circles and} \\
&\text{(a) } \delta_L^{(\mathrm{FWHM,a})} = -444 \pm 30\,\mathrm{MHz}, \quad \text{(b) } \delta_L^{(\mathrm{FWHM,b})} = -472 \pm 36\,\mathrm{MHz}, \quad \text{for the open circles.}
\end{aligned} \tag{5.25}$$

Within the relatively large uncertainties these shifts agree with those determined for the dark resonance position in eq. (5.24). In contrast, the dark resonance amplitude dependence on the optical detuning is different, as shown in fig. 5.27.

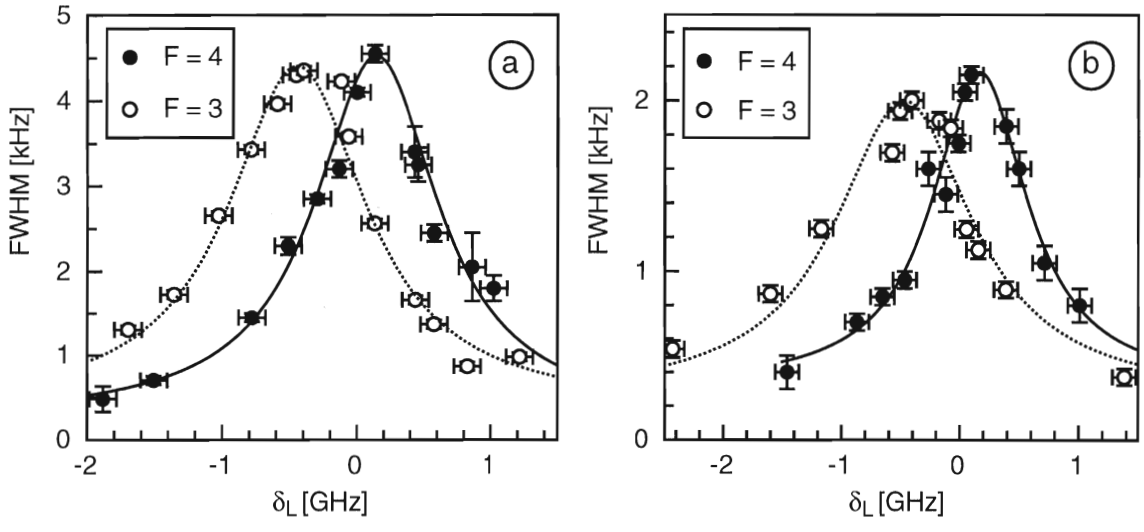

Figure 5.26: *Dark resonance linewidth as a function of the optical detuning for intensities (a) $I_1 = 0.97\,\mathrm{mW/cm^2}$, (b) $I_2 = 0.44\,\mathrm{mW/cm^2}$. Solid circles correspond to an optical carrier frequency near the $F = 4$ transition whereas open circles describe the situation for the optical carrier frequency near the $F = 3$ transition. Lorentzian fit curves are included for all configurations.*

Whereas the curve symmetry for amplitudes is about the same as that for the linewidths, the curves for the two different configurations (solid and open circles, respectively) are hardly shifted with respect to each other. In this case, from the fit of Lorentzian profiles one gets for the symmetry points δ_L^{Ampl}:

$$\begin{aligned}
&\text{(a) } \delta_L^{(\mathrm{Ampl,a})} = -103 \pm 33\,\mathrm{MHz}, \quad \text{(b) } \delta_L^{(\mathrm{Ampl,b})} = -164 \pm 30\,\mathrm{MHz}, \quad \text{for the solid circles and} \\
&\text{(a) } \delta_L^{(\mathrm{Ampl,a})} = -226 \pm 27\,\mathrm{MHz}, \quad \text{(b) } \delta_L^{(\mathrm{Ampl,b})} = -237 \pm 36\,\mathrm{MHz}, \quad \text{for the open circles.}
\end{aligned} \tag{5.26}$$

Comparison with eqs. (5.24), (5.25) also shows that the values for δ_L^{Ampl} roughly lie halfway in between the frequency interval spanned by the values of both δ_L^{pos} and δ_L^{FWHM} for the two different configurations. As for the linewidths γ_{δ_L} of the Lorentzian fit curves for the experimental data of figs. 5.24, 5.26 and 5.27, another interesting aspect arises. Since the intensity dependence of γ_{δ_L} is negligible one can consider intensity averages and gets:

$$\begin{aligned}
\gamma_{\delta_L}^{(\mathrm{pos})} &= 587 \pm 40\,\mathrm{MHz} \quad \text{for the solid circles and} \\
\gamma_{\delta_L}^{(\mathrm{pos})} &= 569 \pm 53\,\mathrm{MHz} \quad \text{for the open circles;}
\end{aligned} \tag{5.27}$$

$$\begin{aligned}
\gamma_{\delta_L}^{(\mathrm{FWHM})} &= 1052 \pm 93\,\mathrm{MHz} \quad \text{for the solid circles and} \\
\gamma_{\delta_L}^{(\mathrm{FWHM})} &= 1336 \pm 100\,\mathrm{MHz} \quad \text{for the open circles;}
\end{aligned} \tag{5.28}$$

$$\begin{aligned}
\gamma_{\delta_L}^{(\mathrm{Ampl})} &= 641 \pm 66\,\mathrm{MHz} \quad \text{for the solid circles and} \\
\gamma_{\delta_L}^{(\mathrm{Ampl})} &= 790 \pm 59\,\mathrm{MHz} \quad \text{for the open circles.}
\end{aligned} \tag{5.29}$$

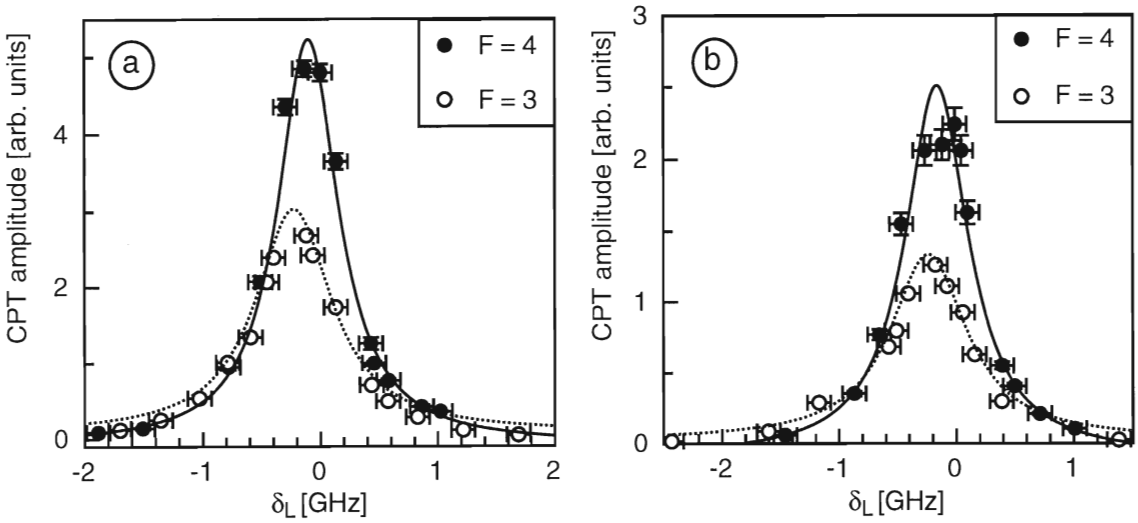

Figure 5.27: *Dark resonance amplitude as a function of the optical detuning for intensities (a)* $I_1 = 0.97\,\mathrm{mW/cm^2}$*, (b)* $I_2 = 0.44\,\mathrm{mW/cm^2}$*. Solid circles correspond to an optical carrier frequency near the* $F = 4$ *transition whereas open circles describe the situation for the optical carrier frequency near the* $F = 3$ *transition. Lorentzian fit curves are included for all configurations.*

In contrast to the symmetry point dependence, there appears to be some agreement between $\gamma_{\delta_L}^{(\mathrm{pos})}$ and $\gamma_{\delta_L}^{(\mathrm{Ampl})}$, whereas $\gamma_{\delta_L}^{(\mathrm{FWHM})}$ is nearly twice as large. Comparison with eq. (3.11) shows that for a neon pressure of 72 mbar collisional broadening of the optical transition is estimated as 620 MHz which is roughly in agreement with $\gamma_{\delta_L}^{(\mathrm{pos})}$ and $\gamma_{\delta_L}^{(\mathrm{Ampl})}$. Comparison with fig. 2.5 indicates that under certain circumstances a larger value for $\gamma_{\delta_L}^{(\mathrm{FWHM})}$ than for $\gamma_{\delta_L}^{(\mathrm{Ampl})}$ might already arise from the simple three-level theory as well. On the other hand, combining the excited state hyperfine splitting with the homogeneous collisional linewidth one also arrives at the same order of magnitude as $\gamma_{\delta_L}^{(\mathrm{FWHM})}$.

A detailed model for the underlying physical mechanisms manifested in the dark resonance dependence on δ_L does not yet exist. One would have to consider a multilevel system taking into account the excited state hyperfine splitting. Furthermore, a more detailed knowledge of the excited state modification due to collisional interaction would certainly be required. Therefore, only a few hypotheses shall be discussed here.

An illustration of the results of this section is given in fig. 5.28 which summarizes the dark resonance position, linewidth, and amplitude dependence on the optical detuning. For each configuration the Lorentzian profiles with parameters determined by the fit to the data of figs. 5.24(a), 5.26(a), 5.27(a) are sketched.

In a first approximation one might assume that buffer gas collisions mainly cause a total shift of all hyperfine levels as well as dephasing and relaxation between the levels. If relative collisional shifts between different hyperfine levels and state mixing remains negligible, one can compare the results of figs. 5.24, 5.26, 5.27 with the usual cesium level scheme, as it is indicated in fig. 5.28.

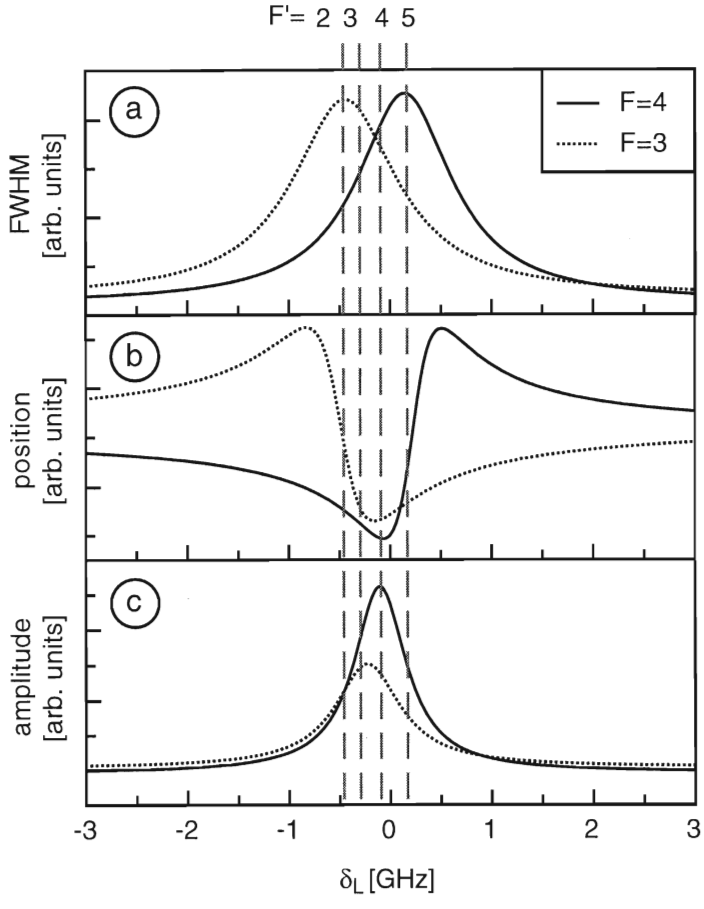

Figure 5.28: *Lorentzian fit curves for the dark resonance FWHM, position and amplitude dependence on the optical detuning. The vertical dashed grey lines roughly correspond to the excited state hyperfine splitting, collisionally shifted as a whole by* $\approx -150\,\mathrm{MHz}$.

For a total shift of the optical transition of approximately $-150\,\mathrm{MHz}$ the maximum linewidths in fig. 5.28(a) are reached if the carrier frequency is resonant with the $F = 4 \mapsto F' = 5$ or $F = 3 \mapsto F' = 2$ transition, respectively. Therefore one might suppose that apart from mere power broadening, which should reach a maximum for zero optical detuning (see 2.5), losses for dark state preparation due to resonant interaction of the strong carrier component with the transition that does not contribute towards the dark state play an important role. Due to electric dipole selection rules this is the case for the $F' = 5$ level, if the carrier frequency near-resonantly couples to the $F = 4$ ground state component, and for the $F' = 2$ level, if the carrier frequency couples to the $F = 3$ component. Under these assumptions, the loss channels are driven effectively as long as the carrier frequency lies within the homogeneous linewidth of the respective transition. This behaviour is only approximately found here, as the linewidths of eq. (5.28) are slightly broader than the expected collisional linewidth of the optical transition.

Pursuing these ideas one anticipates furthermore that within a given Λ-system the dark resonance amplitude increases the nearer the carrier frequency gets to one-photon resonance. Fig. 5.28(c) shows that this is, in fact, the case. Here, the linewidths agree well with the colli-

sional linewidth of about 620 MHz. Even the small shift between the curves corresponding to the $F = 4$ and $F = 3$ components might be explained with this model. From the coupling strengths of the unperturbed cesium atom in eq. (3.43) one finds stronger coupling on the $F = 4 \mapsto F' = 4$ transition than on the $F = 4 \mapsto F' = 3$ transition, and stronger coupling on the $F = 3 \mapsto F' = 3$ transition than on the $F = 3 \mapsto F' = 4$ transition. Hence for the $F = 4$ component one assumes that the main contribution stems from the Λ-system $(|F = 4, 0\rangle, |F' = 4, 1\rangle, |F = 3, 0\rangle)$ whereas for the $F = 3$ component it is the Λ-system $(|F = 3, 0\rangle, |F' = 3, 1\rangle, |F = 4, 0\rangle)$. Comparison with fig. 5.28(b) shows, in fact, that the curve for $F = 4$ (solid line) peaks near the $F = 4 \mapsto F' = 4$ transition and the curve for $F = 3$ (dotted line) peaks near the $F = 3 \mapsto F' = 3$ transition, as expected.

In total, according to the experimental results of this section and the explanations given, the influence of the complete excited state hyperfine multiplet appears to be well resolved in the CPT resonance dependence on the optical detuning δ_L. Whereas in the preceding sections qualitative understanding of experimental results could be reached without having to explicitly include the $F' = 2, 5$ levels into the theory, this appears to be valid only as long as δ_L remains roughly constant. Otherwise both the CPT amplitude and linewidth dependence on δ_L reflect resonant one-photon couplings. If the strong carrier frequency is resonant with an excited level not contributing towards dark state preparation this results in strongly driven loss channels, i.e., increased CPT linewidths. On the other hand, resonant excitation of a Λ-system leads to maximum CPT amplitudes.

Yet, there is also a number of features evading a straightforward explanation within this simple model. For instance, it is not clear, why the symmetry points of the dark resonance position dependence on δ_L (fig. 5.28(c)) coincide with those of the linewidth dependencies, if the linewidth is dominated by loss mechanisms. Moreover, the correspondences discussed above agree with the experimental data only if the total shift of the optical transition is assumed smaller than the prediction of approximately -250 MHz from eq. (3.11). But as the latter results from low resolution measurements only, this discrepancy can not yet be decided upon. As for the dark resonance experiment, the main difficulty arose from the fact that due to the large VCSEL linewidth the optical detuning could only be determined with an uncertainty of about 100 MHz. This might be improved dramatically if power line interferences can be removed from the VCSEL current because then the VCSEL linewidth should reduce to near its intrinsic value of about 20 MHz. Then it should also be possible to calibrate the optical frequency with a much better accuracy from the beat note with another stabilized laser reference frequency. A good test of the hypotheses discussed above might be provided if the dependence of the above effects on relative laser intensities were studied. If the underlying mechanisms really consist of losses one expects the shifts of fig. 5.28 to decrease dramatically for nearly equal relative intensities, i.e., for nearly equal coupling strengths on the $4 \mapsto 5$ and $3 \mapsto 2$ transitions.

5.6 Saturation broadening

As indicated in chapter 2.2 the dark resonance linewidth γ_{CPT} exhibits a strong dependence on intensity. Fig. 5.29 shows the dark resonance full width at half maximum as a function of the master laser intensity measured with the phase-lock set-up for three different buffer gas pressures. As usual, the standard configuration was used and the relative intensity of the two lasers was kept at a constant ratio of 3 : 2. Then the fitting procedure for an FM/AM line profile consisting of the sum of an absorptive and a dispersive Lorentzian allowed to determine the respective parameter set for each experimental spectrum. Finally, the dark resonance linewidth was determined as the FWHM of the demodulated line profile given by the sum of the absorptive and dispersive Lorentzians with the fitted parameters.

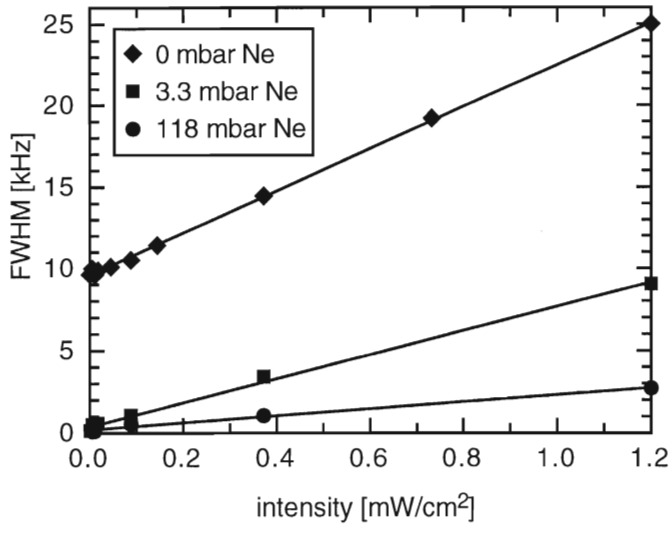

Figure 5.29: *FWHM of the dark resonance as a function of intensity for three different neon buffer gas pressures.*

For high enough intensities one finds a linear dependence with a slope declining for increasing buffer gas pressure. For each buffer gas pressure a straight line fit yielded the line broadening rates ($\mathrm{kHz}/\frac{\mathrm{mW}}{\mathrm{cm}^2}$) which are depicted in fig. 5.30 as a function of buffer gas pressure.

From the model leading to eq. (2.20) a linear dependence of the dark resonance linewidth on intensity is in fact expected. But as that model is based on assumptions which are not fulfilled in the experimental situation (e.g., equal Rabi frequencies) it is hardly possible to draw a quantitative comparison between theory and experiment. Therefore, the model discussed for the AC-Stark shift was applied to saturation broadening as well, and the full width at half maximum was determined directly from the line shapes calculated according to eq.(3.39). For any choice of parameters within the correct order of magnitude a linear dependence results but quantitative agreement with the experimental data cannot be reached for a set of parameters consistent with the experimental conditions. Whereas the constant offset almost exclusively depends on the value for Γ_{12}, the linear slope is mainly determined by the absolute scaling factor for the Rabi

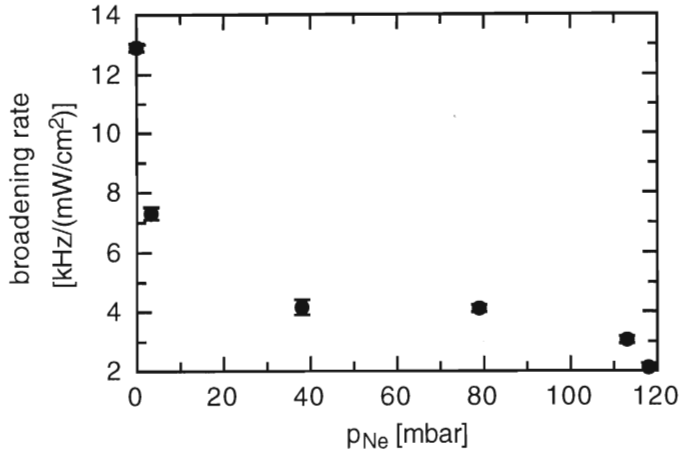

Figure 5.30: *Saturation broadening rate of the dark resonance as a function of buffer gas pressure*

frequencies. All other parameters, such as the ratio γ_{12}/Γ_{12} and the optical detuning δ_L, only have a minor influence.

In the absence of buffer gas a straight line fit to the experimental data yields $\gamma_{\mathrm{CPT}} = (9.60 \pm 0.06)\,\mathrm{kHz} + (12.9 \pm 0.1)\,\mathrm{kHz}/\frac{\mathrm{mW}}{\mathrm{cm}^2} \cdot I_{\mathrm{master}}$. For the best fit to these values the theoretical model gives $2\Gamma_{12} = 8.4\,\mathrm{kHz}$ and an artificial scaling factor for the absolute Rabi intensity of $1/40$. Whereas Γ_{12} is of the same order of magnitude as expected from time-of-flight broadening the scaling factor for the Rabi frequencies cannot be understood. Inserting 'correct' Rabi frequencies yields a far too strong saturation broadening behaviour: the broadening rate is wrong by a factor of about 35, as opposed to the low intensity limit which roughly remains the same. In contrast to the minor discrepancies between theory and experiment arising from the discussion of the AC-Stark shift, the disagreement encountered here shows that this theory does not lead to quantitative understanding of the dark resonance power broadening.

As for the influence of the buffer gas, one can compare the experimental results depicted in figs. 5.30 and fig. 5.20. Both the power broadening rate and the dark resonance linewidth remain roughly constant over the same range of intermediate buffer gas pressures, whereas in both cases major changes occur for smaller and larger pressures. This indicates that the dark resonance power broadening behaviour depends in a complicated manner on the experimental conditions. If it were dependent on the optical decay rates only, one would expect a fairly uniform dependence on the buffer gas pressure according to the collisional broadening of the excited states. Instead, the two characteristic processes of line narrowing due to the onset of atom diffusion at low pressures and collisional ground state relaxation at higher buffer gas pressures manifest themselves in both the dark resonance linewidth and the power broadening behaviour. Similarly to the treatment of line narrowing with the help of diffusion theory a more adequate model for power broadening still has to be sought.

For a further investigation of these questions the power broadening behaviour was examined for the set of experimental and theoretical curves illustrated in fig. 5.18. The neon pressure of 72 mbar corresponds to the intermediate buffer gas pressure range where for the dark resonance time-of-flight broadening is well suppressed and collisional broadening is still negligible. In contrast to the measurements with the phase-lock set-up discussed so far in this section, the use of the VCSEL set-up entails that the intensities of the bichromatic field strongly differ from each other. Hence the linear power broadening behaviour of eq. (2.20) need not necessarily hold any more.

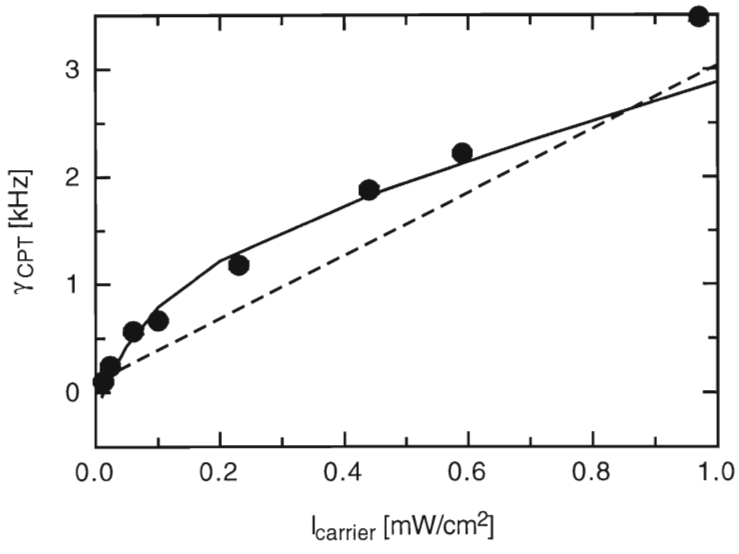

Figure 5.31: *Dark resonance power broadening for 72 mbar neon and the configuration of fig. 5.18: experimental data (solid circles), calculations for two different treatments of the Lamb-Dicke effect (solid and dashed lines)*

Fig. 5.31 shows the resulting dependence of the dark resonance linewidth on intensity, where the solid circles represent the experimental values. The solid line corresponds to the calculation at first ignoring the Lamb-Dicke effect. Since under this assumption the linewidth remains much too broad (see fig. 5.18(c)) a total of 9.5 kHz was subtracted from each calculated linewidth. This might be considered as yet another approach towards the treatment of Lamb-Dicke narrowing. The dashed line corresponds to the calculation leading to fig. 5.18(b), i.e., ignoring Doppler-broadening at the 9 GHz frequency, without any further treatment. Whereas the slope of the overall dependence is in fact reproduced correctly by the dashed line, the solid line correctly describes the non-linear behaviour at low intensities. Hence, despite the fact that both of the two approaches towards Lamb-Dicke narrowing consist of rough approximations only, the agreement with the experimental data is even better than for the unbuffered case. Whereas an additional factor of 35 for intensity was needed to reproduce the power broadening behaviour in the absence of buffer gas, here it is only a factor of 0.5. The enormous discrepancy between these factors might again be a hint at the influence of time-of-flight effects dominating dark state preparation in the unbuffered case such that the stationary approach applied here would

not be adequate. According to fig. 5.30 the factor would be more different from unity for higher buffer gas pressures as well, which could then be attributed to the fact that the ground state coherence directly gets disturbed by collisions. On the whole, the best agreement is reached for intermediate buffer gas pressures where dark state preparation is essentially free of both influences. But this conclusion can certainly not yet be considered final because — as discussed throughout this chapter — the description of the dark resonance dependence on buffer gas collisions, laser linewidth, optical pumping etc., is phenomenological in some parts and guided by physical intuition and not mathematical rigour.

5.7 Optical pumping

Optical pumping is not investigated in detail in this thesis. As the CPT model developed in chapter 3.3 (based on equal population of Zeeman levels, i.e., the absence of optical pumping between those levels) shows excellent agreement with the experimental results, the concern of this section is only to demonstrate that population redistribution can be detected at all. The effects of optical pumping within a multilevel system exposed to light irradiation have been studied for several decades, for review articles see, for instance, [HAP72, WAL97]. In the case of the hyperfine split cesium D_2 line both depopulation and repopulation pumping occurs. Whereas repopulation pumping transfers excited state polarization to the ground state via spontaneous emission, the former results from different excitation rates out of the ground state Zeeman levels and thus gets dominant if the excited state polarization is instantaneously destroyed, e.g., by buffer gas collisions. The use of $\sigma^+\sigma^+$ polarized light tends to polarize the atom via optical pumping between Zeeman levels. Due to the respective coupling strengths under many circumstances the net effect is population redistribution towards higher values of m_F, although, e.g., if depopulation pumping is dominant, the net effect might well be different for $F = 4$ and $F = 3$, as calculated by a rate equation model for atomic populations [LAN97].

The optical pumping rate $\gamma^{(p)}$ is given by $\gamma^{(p)} = \tilde{g}^2/\gamma_{\text{hom}}$, where $\tilde{g}$ is the Rabi frequency for the respective transition and γ_{hom} the homogeneous linewidth of the excited state. Thus on Raman resonance there are two rivalling processes: direct optical pumping into a coherent dark state at a rate $\gamma^{(\text{CPT})}$ such that the atoms are lost for other processes, and Zeeman pumping via absorption-emission cycles accumulating atomic population in higher m_F states at a rate $\gamma^{(p)}$ before the atoms finally end up in a coherent dark state. The contributions of both processes become apparent from the distribution of the relative strengths of the CPT Zeeman components. Fig. 5.32 shows relative strengths of CPT Zeeman components for the standard configuration in a cell containing 5 mbars of neon for two different total intensities $I_1 = 1.8\,\text{mW/cm}^2$, $I_2 = 0.2\,\text{mW/cm}^2$.

For I_1 the spectrum's centre of gravity is clearly shifted towards higher m_F values whereas for I_2 there is reasonable agreement with the the calculated spectrum (solid line) according to chapter 3.3. Note that the asymmetry of a spectrum is in itself not necessarily a signature of optical

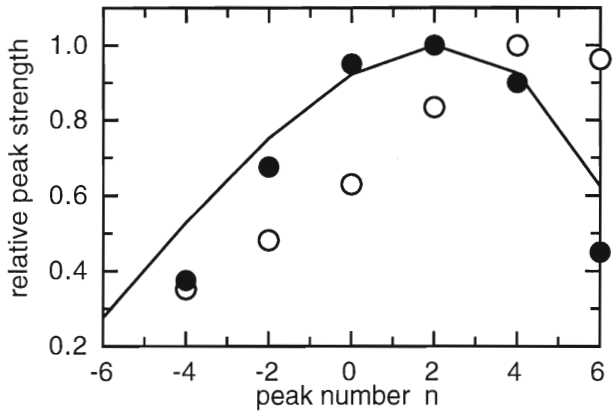

Figure 5.32: *Relative strengths of CPT Zeeman components for the standard configuration, a cesium cell also containing* 5 mbars *of neon, and total intensities* $I_1 = 1.8\,\mathrm{mW/cm^2}$ *(open circles),* $I_2 = 0.2\,\mathrm{mW/cm^2}$ *(solid circles). The solid line represents a calculation according to chapter 3.3.*

pumping because it could also be produced by different coupling strengths. For instance, comparison of fig. 5.7 and fig. 5.2 shows that for the standard configuration the calculated spectrum is symmetric in the buffer gas case, whereas in the absence of buffer gas it is asymmetric, with increasing peak strengths for higher values of m_F.

For fixed intensity $\gamma^{(p)}$ is reduced with increasing buffer gas pressure as γ_{hom} increases. Furthermore, for increased collisional depolarization of the excited state, depopulation pumping gets more important which leads to much less pronounced population redistribution. From these qualitative remarks one expects Zeeman pumping to become considerably less effective for higher buffer gas pressure. In fact, for high buffer gas pressures deviations from the symmetrical spectrum as in fig. 5.2 could hardly be detected.

6 Precision measurements

6.1 Magnetometry

Currently the sensitive detection of small magnetic fields finds many applications and each appears to have a different method specialized to meet particular needs. Whereas biomedical applications are almost exclusively the realm of so-called SQUIDS, optical pumping magnetometers (OPM) are frequently used in geophysics and archaeology [BEC95]. Sensitivities as low as a few $\mathrm{fT}/\sqrt{\mathrm{Hz}}$ are reported for both devices [ALE94, VOD92].

Still it is for a number of reasons that magnetometry with coherent dark states appears to be very promising. First of all, the practical implementation of a dark state magnetometer does not have some of the drawbacks of the other devices. In contrast to SQUID detectors no cryogenic cooling is required. And if compared to optical pumping magnetometers the advantage of an all-optical set-up becomes apparent: in contrast to the typically cm-sized microwave interaction region a spatial resolution in the micrometre range could in principle be reached. Furthermore, the detector head does not have to consist of any metal components but could consist of a (miniature) sealed glass cell and optical fibres only. Therefore stray fields from electric wires do not appear and the sensor head can even reach points that are less easily accessible, e.g., in medical applications, since its only connection to the rest of the set-up consists of a thin optical fibre. Furthermore, the successful preparation of dark states using VCSELs allows for a miniaturized device which is mechanically stable and needs battery supply only.

Apart from these practical considerations a fundamental advantage of a dark state magnetometer over an OPM has been discussed, where for a set-up of Mach-Zehnder type reduced susceptibility to power broadening and sensitivities as low as 0.1 fT for 1 s averaging time were predicted [SCU92, FLE94].

However, apart from the experiment described below [NAG98] so far no experimental implementation of a coherent dark state magnetometer has been realized. It also has to be noted that the configuration described below is completely different from the one proposed in [SCU92, FLE94] where higher optical power and atomic densities are required.

For the sensitive detection of small magnetic fields the signal of interest has to be extracted from the background of ever-present magnetic noise signals. Such noise components arise, e.g., from laboratory electronics or fluctuations of the geomagnetic field with typical flux densities of several nT for Fourier components in the kHz range. Several methods can be thought of to overcome this difficulty. The sensor could be shielded from external magnetic fields with the help of a high-quality μ-metal shielding. However, for practical applications one does not always want to perform measurements inside an extremely well shielded environment only. Measuring DC fields in the presence of large noise contributions can be facilitated with the help of so-called gradiometric arrangements of SQUIDs [ROM82]. For single Fourier components of AC fields phase sensitive detection with a lock-in amplifier can be used as described below.

6.1.1 Experimental realizations

As explained in detail in chapter 5.1 the presence of a magnetic field destroys the Zeeman degeneracy of the dark states which are shifted at a rate given by the Breit-Rabi formula, where the relative height of the respective Zeeman components depends on the geometry of field direction and laser polarizations. In principle, coherent dark states can be used for the determination of magnetic fields of arbitrary strength. Therefore one might distinguish between two cases:

Strong field If the magnetic field is strong enough to resolve the individual Zeeman components a fit of the peak positions according to the Breit-Rabi formula results in an absolute value for the magnetic field. As long as the field is small enough for (F, m_F) to remain good quantum numbers for all atomic levels involved, which is usually the case for flux densities up to a few mT, the magnetic field strength only changes line positions whereas the line shape of the individual Zeeman components remains unaffected. Hence the relative accuracy is independent of the magnetic field strength. However, since the experiment only allows to infer the parameter $x = (g_J - g_I)\mu_B B/\hbar$, the determination of the absolute field strength requires knowledge of g-factors which are known only to within $1.3 \cdot 10^{-6}$ [WHI73], the accuracy is thus limited. Fig. 6.1 shows an example of a dark resonance spectrum in a strong field recorded with the phase-lock set-up from which the respective flux density was determined as $B = (21.2265 \pm 0.0006)\,\mu$T with a relative uncertainty for the numerical fit parameter x of about $3 \cdot 10^{-5}$.

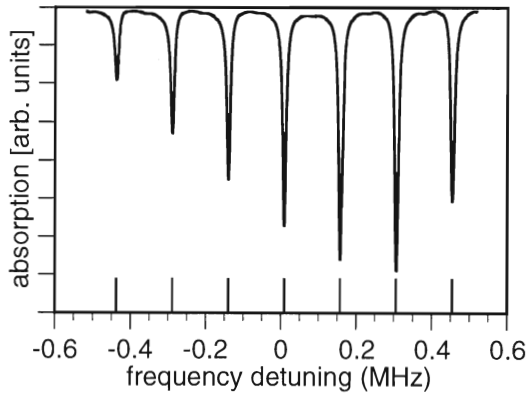

Figure 6.1: *Zeeman-split dark resonances (standard configuration and 87 mbar neon) from which the flux density could be determined with better than $3 \cdot 10^{-5}$ relative uncertainty. The short vertical lines indicate the fitted resonance positions.*

Weak field If for a given linewidth of the dark resonance Zeeman components the magnetic field is not strong enough to resolve single components a slightly more complicated situation results, and the information on magnetic field strength has to be drawn from changes in line shape instead of line position directly.

In the following only the experimentally tested case of phase-locked lasers with equal circular laser polarizations and an unbuffered cell is considered. The cesium cell could be placed inside a double-layer μ-metal cylinder with an estimated shielding factor of about 1000. Since the magnetic shielding available was by far not good enough for the envisioned precision of the experiment one had to retreat to a modulation technique in order to filter the signal out of a large background noise. Therefore only Fourier components of a magnetic field oscillating at a given frequency could be detected in this experiment. Instead of the usual modulation of the slave laser injection current this time the modulation in the kHz range was applied via an oscillatory magnetic field. This could be accomplished either with the help of a wire in a single-turn Helmholtz configuration wrapped directly around the cell, or by a current coil placed at a certain distance from the cell.

The alternating magnetic field $B(t) = B_{\text{const}} + B_{\text{mod}} \cos(\omega_{\text{mod}} t)$ modulates the frequency separation between the dark resonance Zeeman components. The photodiode recording the transmission signal behind the cesium cell of length l effectively averages over all optical and r. f. frequencies beyond its response bandwidth such that the photocurrent is finally given by

$$I(\nu, B(t)) = I_0 \, e^{-2\delta(\nu, B(t))} \, . \tag{6.1}$$

The resulting line shape as recorded by a lock-in amplifier is proportional to the derivative of the transmission signal:

$$S(\nu, B_{\text{const}}) = B_{\text{mod}} \left. \frac{dI(B)}{dB} \right|_{B_{\text{const}}} . \tag{6.2}$$

For a longitudinal magnetic field $\delta(\nu, B(t))$ is represented by a superposition of seven Lorentzian components with relative strengths $\delta_j = (0.47, 0.68, 0.88, 0.91, 1, 1, 0.75)$ calculated from eq. (3.30):

$$\delta(\nu, B) = \delta_0 \sum_{j=-3}^{j=3} \delta_j \frac{(\gamma_{\text{CPT}}/2)^2}{(\nu - \nu_0 - 2\, j\, \xi\, B(t))^2 + (\gamma_{\text{CPT}}/2)^2} \tag{6.3}$$

with a shift rate $\xi \approx 3.5\,\text{Hz/nT}$ according to eq. (3.16). Hence the signal can be calculated as:

$$S(\nu, B_{\text{const}}) \propto B_{\text{mod}} \, e^{-2\delta(\nu, B_{\text{const}})} \sum_{j=-3}^{j=3} \delta_j \frac{j\,(\nu - \nu_0 - 2\, j\, \xi\, B_{\text{const}})}{(\nu - \nu_0 - 2\, j\, \xi\, B_{\text{const}})^2 + (\gamma_{\text{CPT}}/2)^2} \, . \tag{6.4}$$

For $B_{\text{const}} \neq 0$ the line shape shows an asymmetry depending on B_{const}. This allows to actually use the method even in the weak field limit because it is possible to determine a constant offset

field without the need to resolve the Zeeman components. Furthermore, for zero offset field and $\delta_j = \delta_{-j}$ (as it is the case for high buffer gas pressures) the lock-in signal is identically zero such that this method is not always applicable. Finally, the total signal strength is expected to be proportional to the amplitude of the alternating magnetic field B_{mod}. This was demonstrated in a series of measurements where a transverse field of several hundred pT amplitude oscillating at $\nu_{\mathrm{mod}} = 8\,\mathrm{kHz}$ was applied. The field was generated by a current coil placed at a distance of 1 m from the cell for sufficient homogeneity. Since no shielding or DC compensating field was used the dark resonance was split into eight components and for each amplitude B_{mod} the total signal strength $S(B_{\mathrm{mod}})$ was determined as $S(B_{\mathrm{mod}}) = \int R d\nu$, with $R = \sqrt{X^2 + Y^2}$ calculated from the in-phase and quadrature components of the lock-in signal. Fig. 6.2 confirms the expected linear dependence.

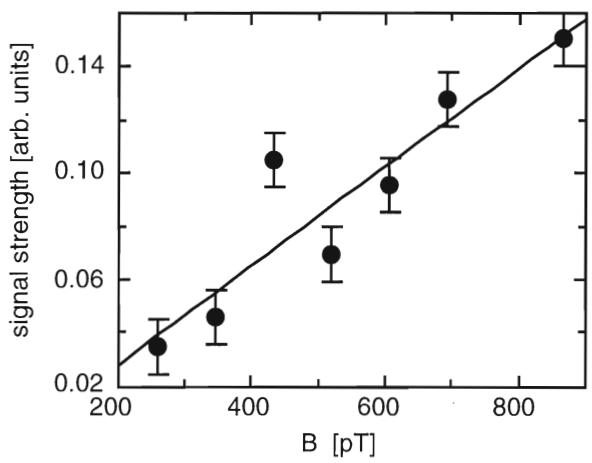

Figure 6.2: *Total signal strength as a function of the oscillatory magnetic field amplitude exhibiting the expected linear dependence*

In order to evaluate the sensitivity of such a device the cell was placed inside the shielding cylinder and the alternating field was applied via the Helmholtz wire loops. The magnetic field thus produced was calibrated in the μT range where the flux density was determined directly from the dark resonance Zeeman splitting. Agreement was reached with the calculated values. Fig. 6.3 shows a typical spectrum obtained for an amplitude of $B_{\mathrm{mod}} = (7.2 \pm 0.8)\,\mathrm{pT}$ at a modulation frequency of 8 kHz together with a fit according to eq. (6.4). Each point of the experimentally recorded spectrum resulted from averaging over 0.6 s. The DC offset field was determined from the fit as $B_{\mathrm{const}} = (31 \pm 3)\,\mathrm{nT}$ which is consistent with the geomagnetic field attenuated by the estimated shielding factor. The fitted linewidth $\Delta\nu = 40\,\mathrm{kHz}$ is also in agreement with the estimated power broadening for a laser intensity of about $1\,\mathrm{mW/cm^2}$.

Because of the linear dependence of the signal strength on B_{mod} it is possible to extrapolate the minimum detectable oscillatory amplitude ΔB_{min} from the recorded spectra and the respective signal-to-noise ratios S/N: $\Delta B_{\mathrm{min}} = B_{\mathrm{mod}}/(S/N)$. The noise was taken as the residual rms value of the difference between the fit function and the experimental data. With $S/N \approx 15$ for the spectrum of fig. 6.3 extrapolated sensitivities below 500 fT result for modulation frequencies of

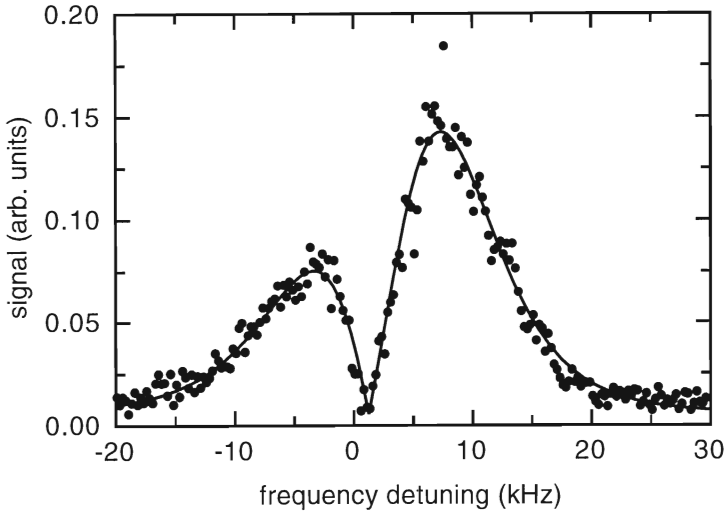

Figure 6.3: *Dark resonance line shape (R-component of the lock-in signal) for field modulation at* $\omega_{\mathrm{mod}} = 8\,kHz$ *with amplitude* $B_{\mathrm{mod}} = 7\,pT$. *The solid line is a numerical fit for R based on eq.* (6.4).

5 – 10 kHz. Although this method is based on the detection of changes in line shape as a measure of changes in magnetic field strength one does not always have to record a whole spectrum. For instance, monitoring the amplitude of the two maxima allows to determine AC field changes from a change of the overall amplitude whereas DC field changes can be inferred from a change in relative height of the two maxima. More details on these magnetometry measurements can be found in [GRA97].

By definition, i.e., the restriction to a longitudinal field only, the methods described here are examples of scalar magnetometers which are sensitive to line positions depending on $|\vec{B}|$ only. But principally one might also think of a vector device exploiting the field directional dependences discussed in chapter 5.1. Recently, a certain configuration of a dark resonance vector magnetometer was analysed theoretically [LEE98].

In comparison with typical field strengths and sensitivities sketched in fig. 6.4 the sensitivity obtained so far has to be extended towards lower frequencies in order to compete with the existing devices for interesting applications, e. g. in medicine. Although the absolute value of the field amplitudes detected can already be compared to typical performances of optical pumping magnetometers one has to keep in mind that the 1/f noise components increase considerably for the interesting range of low frequencies. Therefore a direct comparison is not yet possible. However, the results obtained here are nowhere near the maximum sensitivity achievable. First of all, due to the particular features of eq. (6.4) only unbuffered cells entailing broad CPT linewidths could be used. Secondly, from the shielding factor of about 1000 the AC component of the geomagnetic field is attenuated only to about a few pT. Therefore hardly any improvement could be expected without switching to a much better magnetic shielding which was not available at the time.

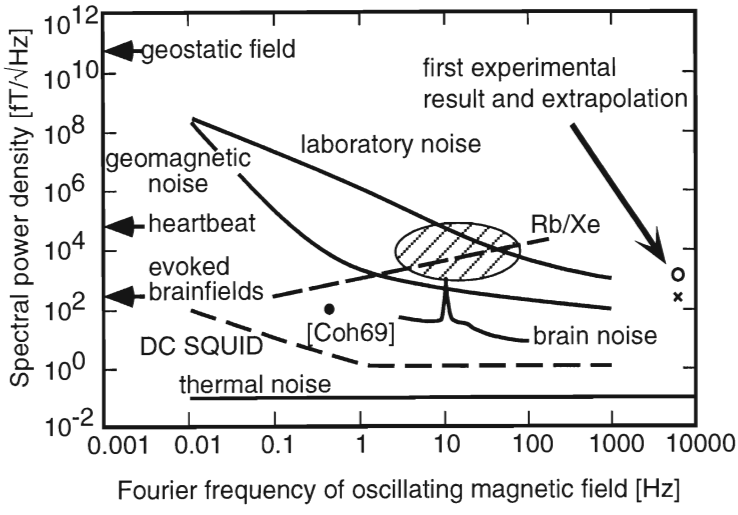

Figure 6.4: *Typical field strengths of various sources, and typical sensitivities of selected magnetometers, taken from* [HÄM93]. *The symbols at 8 kHz Fourier frequency represent the first test experiment (circle) and its extrapolation to a S/N ratio of unity (cross). 'Rb/Xe' stands for a particular type of optical pumping magnetometer* [WÄC97]. *If the dark state magnetometer could be optimize for the shaded region it would be a novel compact room-temperature device, e.g., for the measurement of magnetic fields of the beating heart.*

6.2 Measurements of g-factor ratios

As discussed in section 6.1.1 the ultimate accuracy for magnetic flux density measurements could be increased if the g-factors were known with higher accuracy. Furthermore, knowledge of the g-factors also allows to test electronic wavefunction calculations, which, in turn, are important for experiments on the violation of fundamental symmetries in atoms [BOU74, WOO97]. The determination of g-factors is based on the sensitive detection of magnetic fields where current knowledge for cesium stems from magnetic resonance experiments [WHI73]. Following the discussion in section 6.1 a CPT-based device should exhibit similar advantages for the determination of g-factor ratios as it is supposed to do with respect to magnetometers.

In the following, two proof-of-principle experiments are reported which exploit different experimental configurations. In both cases it has to be kept in mind that the presence of a buffer gas has a significant influence on the measurements. As discussed theoretically in [HER68], collisional interaction with the buffer gas atoms causes g-factor shifts. Therefore optimization of g-factor ratio measurements would have to include a detailed analysis of the dependence on buffer gas pressure. Moreover, as the absolute position of the CPT resonance cannot be determined with high enough accuracy (mainly due to insufficient knowledge of the buffer gas pressure and thus the corresponding shift according to fig. 5.22) the dark resonance position is yet another parameter to be obtained from a fit to the data.

6.2.1 g-factor ratios from low resolution spectra

As seen in fig. 6.5, for equal circular laser polarizations and an oblique magnetic field the dark resonance splits into 15 Zeeman components, in agreement with the theoretical model of chapter 3.3. Even-numbered components correspond to couplings with $\Delta m = \pm 1$ and odd-numbered components to those with $\Delta m = 0$.

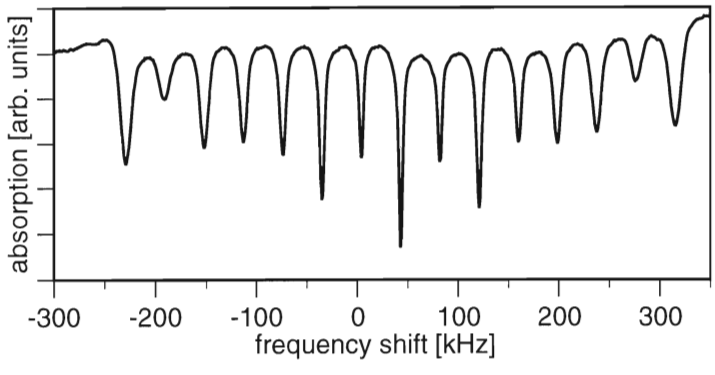

Figure 6.5: *Dark resonance split into 15 Zeeman components in an oblique magnetic field with $B = 11.1\,\mu T$ and equal circular polarizations.*

In this experiment the splitting due to the nuclear contribution discussed in section 5.1.4 was not resolved. Since the linewidth of each Zeeman component was much larger than the expected splitting due to the nuclear contribution (by about a factor of 40) it was sufficient to neglect the splitting and to take into account the stronger components only. Recalling the expression for the dark resonance Zeeman shift of eq. (3.15) and including an additional shift δ_p (e.g., accounting for pressure shifts) one finds

$$\Delta f(m_3, m_4) = \delta_p + a(m_4 - m_3) + \frac{\Delta_{\text{hfs}}}{2}\left(\sqrt{1 + \frac{m_4}{2}x + x^2} + \sqrt{1 + \frac{m_3}{2}x + x^2}\right) . \tag{6.5}$$

Hence a fit for the line positions with $\Delta m = 0$ yields the parameters $x^{(\text{fit})} = (g_J - g_I)\mu_B B/h\Delta_{\text{hfs}}$ and δ_p. With $x^{(\text{fit})}$ and δ_p fixed the position of the resonance lines with $\Delta m = \pm 1$ can be used to determine $a^{(\text{fit})} = g_I \mu_B B/h$ such that

$$\frac{g_I}{g_J} = \frac{1}{1 + \Delta_{\text{hfs}} \frac{x^{(\text{fit})}}{a^{(\text{fit})}}} . \tag{6.6}$$

Thus for the spectrum of fig. 6.5 one obtains

$$\frac{g_I}{g_J} = -1.87(11) \cdot 10^{-4} \tag{6.7}$$

which agrees with the acknowledged value of $-1.9917400(26) \cdot 10^{-4}$ [WHI73], although with much lower precision. But this does not come as a surprise because the experiment has by far not been optimized yet. In fact, it is only due to the high precision of the dark resonance spectrometer

that the influence of the tiny nuclear magnetic moment can be detected already at a field of $11\,\mu$T. Straightforward improvements include the application of much higher magnetic fields, and lower intensities so as to obtain smaller linewidths. Apart from that, optimization will also have to include the experimental configuration (magnetic field direction and laser polarizations) and the fitting procedure for $x^{(\mathrm{fit})}$, $a^{(\mathrm{fit})}$ and δ_p.

6.2.2 g-factor ratios from higher resolution spectra

Using the configuration leading to the detection of line splittings in section 5.1.4 one might hope for increased precision because the spectra resolve more subtle details depending on the parameters of interest. Using the data set depicted in fig. 5.11 one has to include all contributions of eq. (6.5) such that the fitting procedure gets more complicated. Replacing (g_i, g_J ,B) by ($r := -\frac{g_I}{g_J}$, $b := g_J \mu_B B/h$) in equation (6.5) and using $m_4 = \frac{1}{2}(n + \Delta m)$, $m_3 = \frac{1}{2}(n - \Delta m)$ one finds

$$\Delta f(n, \Delta m) = \delta_p + rb\Delta m + \frac{\Delta_{\mathrm{hfs}}}{2}\left(\sqrt{1 + \frac{n + \Delta m}{4}\frac{(1-r)\,b}{\Delta_{\mathrm{hfs}}} + \frac{(1-r)^2\,b^2}{\Delta_{\mathrm{hfs}}^2}} + \sqrt{1 + \frac{n - \Delta m}{4}\frac{(1-r)\,b}{\Delta_{\mathrm{hfs}}} + \frac{(1-r)^2\,b^2}{\Delta_{\mathrm{hfs}}^2}} \right). \quad (6.8)$$

Without detailed knowledge of B it is not possible to infer both g_I and g_J from eq. (6.8) but only the g-factor ratio r. From a fit of r, b, δ_p to the 8 dark resonance positions obtained from the spectra of fig. 5.11 one gets

$$\frac{g_I}{g_J} = -1.9821(31) \cdot 10^{-4}\,, \quad (6.9)$$

corresponding to a precision of $1.6 \cdot 10^{-3}$ which is an improvement with respect to eq. (6.7) but still three orders of magnitude worse than the literature value of $-1.9917400(26) \cdot 10^{-4}$ [Whi73]. The error reported in eq. (6.9) only results from the precision with which the dark resonance line centres could be determined and does not pay attention to systematic errors at all. Therefore the 0.5 % deviation from the literature value does not bear any significance yet. Sources for systematic errors concerning the measurement of g-factor ratios are manifold, but major contributions certainly arise from drifts of the applied magnetic fields such that different spectra were obtained for different magnetic field strengths. For instance, since decreasing the total time interval needed to record the spectra changes the influence of those drifts, performing the fit with the peaks corresponding to $n = -1, \pm 3$ only, yields $\frac{g_I}{g_J} = -1.9920(42) \cdot 10^{-4}$, i.e., agreement with the literature value and a slightly increased fitting error. Hence the total error of this proof-of-principle measurement must be estimated at least an order of magnitude larger than the fitting error. Further systematic errors can arise from most of the line shifting effects discussed in chapter 5. In particular, due to different coupling strengths the AC-Stark shifts

for the various peaks under consideration can well differ from each other by several percent of the total line splittings. Considerable improvement in precision can be expected, e.g., from decreasing the dark resonance linewidth. Eq. (6.9) was derived from dark resonances with typically a few kHz linewidth and line positions determined to within a few ten Hz, which is almost two orders of magnitude from the smallest linewidths obtained so far, mainly due to magnetic field inhomogeneities.

7 Conclusion

The combination of recent advances in semiconductor laser technology and well-known buffer gas techniques facilitates precision spectroscopy of coherent dark resonances with a compact and robust experimental set-up. In the beginning, coherent coupling of two independent grating stabilized diode lasers via optical phase-lock had allowed to study and understand the influence of laser polarizations on CPT resonances. Since such a set-up still covers an area of about half a square metre on an optical table and is mechanically too unstable for practical applications envisioned also outside the laboratory environment, it was replaced by a much simpler device that might also be imagined in a miniature version as small as several cubic centimetres only. Frequency modulation of recently developed *vertical-cavity surface-emitting lasers* at 9.2 GHz was demonstrated to be efficient enough for dark state preparation and precision spectroscopy.

On the whole, the main concern of the experiments described in this thesis was twofold:

Systematic investigations of coherent population trapping resonances in thermal cesium vapour were performed, and the results were compared with theoretical models.

A physically intuitive model has been developed which explains multilevel CPT resonance dependence on the geometrical configuration, i.e., the number and relative strengths of the Zeeman components as a function of laser polarizations and magnetic field direction. Since the model is based on symmetry arguments rather than a complete description of the atom light interaction it allows to treat the influence of geometry independently of line shapes, shifts, and widths. Agreement with the prediction of this model could be reached in all of the relevant experimental investigations. These also included CPT resonances induced by pure quadrupole coupling and line splittings due to the nuclear contribution only.

The addition of a buffer gas led to the unprecedented observation of CPT linewidths as narrow as 42 Hz in thermal cesium vapour. Systematic investigations were performed to scrutinize the CPT resonance susceptibility towards line shifting and broadening influences such as the AC-Stark shift, power broadening, collisional interaction with the buffer gas atoms, and the optical detuning from one-photon resonance. In order to understand the respective results a theoretical approach complementary to the multilevel model was chosen in that the properties of a single CPT Zeeman component were sought to be understood from a three-level based model. Although qualitative and in some cases also quantitative agreement was reached the limitations of this approach also became obvious thus necessitating further refinement of the theory.

Although **applications** for CPT resonances in the sensitive measurement of magnetic fields have been proposed, the experiments described in this thesis and published in [NAG98] constitute the first proof-of-principle demonstrations of these possibilities.

Static fields in the μT range could be determined directly from the CPT Zeeman splitting with $3 \cdot 10^{-5}$ relative uncertainty. A modulation technique allowed to detect magnetic fields oscillating in the kHz range for flux densities as low as 7 pT where an integration time of 0.6 s

per measurement point was used. Extrapolation from the S/N ratio yielded a sensitivity limit of about 500 fT for that particular experimental set-up. Furthermore, the method also permitted to determine a residual static field of about 30 nT from characteristic features of the line shape.

Also based on the sensitive detection of magnetic fields is the determination of the ratio g_I/g_J. For suitable geometrical configurations this ratio could be inferred from the position of the CPT Zeeman components. Using magnetic fields strong enough to resolve non-linear Zeeman shifts and to completely separate all components predicted by the Breit-Rabi formula yielded a precision of about 10^{-3} which is still three orders of magnitude below the current literature value, mainly because in this proof-of-principle experiment not enough attention had been paid to the stability of the applied magnetic field. Future experiments might also allow to determine g_I/g_J as a function of buffer gas pressure in order to look for collisional modifications.

After these successful proof-of-principle experiments future developments will certainly have to focus on the high potential for technical improvements, e.g., concerning the stability of various current sources. The availability of VCSEL with higher optical power and probably the use of heated cesium cells might yet be other steps towards an implementation of a magnetometer with unprecedented sensitivity.

A Frequency modulation techniques

A.1 Frequency modulation with residual amplitude modulation

In order to calculate the frequency dependence of the two lock-in phase components one starts from the expression for a frequency- and amplitude-modulated light field oscillating at the optical frequency ω_0 with modulation frequency ω_m, phase modulation index M, amplitude modulation index R and phase ψ between FM and AM:

$$E = \frac{E_0}{2}\big(1 + R\sin(\omega_m t + \psi)\big)\exp(i(\omega_0 t + M\sin(\omega_m t)) + c.c.\,. \tag{A.1}$$

Expansion into series of Bessel functions $J_k(M)$ yields a decomposition into modulation sidebands of all orders:

$$E = \sum_k a_k e^{i(\omega_0 + k\omega_m)t} + c.c. \tag{A.2}$$

with coefficients

$$a_k = \frac{E_0}{2}\Big(J_k(M) - i\frac{R}{2}e^{i\psi}J_{k-1}(M) + i\frac{R}{2}e^{-i\psi}J_{k+1}(M)\Big)\,. \tag{A.3}$$

After the passage through the medium, which is assumed to be optically thin, both the amplitude and the phase of each sideband have been modified. This can be described with the help of complex transmission coefficients $T_k = \exp(-\delta_k - i\phi_k)$, where $(-\phi_k\,, \delta_k)$ are proportional to the real and imaginary parts of the non-linear susceptibility of the medium, evaluated at frequencies $\omega_0 + k\omega_m$. Hence the transmitted light field E_T reads

$$E_T = \sum_k a_k T_k e^{i(\omega_0 + k\omega_m)t} + c.c. \tag{A.4}$$

With a factor η describing detector sensitivity and electronic gain factors the intensity I_0 on a square-law detector is given by

$$\begin{aligned} I_0 &= \frac{1}{2}\epsilon_0 c\eta |E_T|^2 \\ &= \frac{1}{2}\epsilon_0 c\eta \sum_{k,l} a_k a_l^* T_k T_l^* e^{i(k-l)\omega_m t} + c.c.\,, \end{aligned} \tag{A.5}$$

where frequency contributions at twice the optical frequency ω_0 have been omitted because they are well beyond the detector response bandwidth. Then the lock-in amplifier picks out the signal component I oscillating at ω_m:

$$I = \epsilon_0 c\eta \sum_k a_k a_{k-1}^* T_k T_{k-1}^* e^{i\omega_m t} + c.c. \tag{A.6}$$

and under the assumption of $|\phi_k(\omega) - \phi_{k-1}(\omega)| \ll 1$, $|\delta_k(\omega) - \delta_{k-1}(\omega)| \ll 1$ one gets:

$$\begin{aligned} I \approx \quad & \epsilon_0 c\eta e^{-2\delta_0} \sum_k a_k a_{k-1}^* \Big(1 + 2\delta_0 - \delta_k - \delta_{k-1} - i\phi_k + i\phi_{k-1}\Big) e^{i\omega_m t} + c.c. \\ = \quad & 2\epsilon_0 c\eta e^{-2\delta_0} \Bigg[\mathrm{Re}\Bigg(\sum_k a_k a_{k-1}^* \big(1 + 2\delta_0 - \delta_k - \delta_{k-1} - i\phi_k + i\phi_{k-1}\big) \Bigg) \cos(\omega_m t) \\ & \quad -\mathrm{Im}\Bigg(\sum_k a_k a_{k-1}^* \big(1 + 2\delta_0 - \delta_k - \delta_{k-1} - i\phi_k + i\phi_{k-1}\big) \Bigg) \sin(\omega_m t) \Bigg] \\ = \quad & \tfrac{1}{2}\epsilon_0 c\eta |E_0|^2 e^{-2\delta_0} \Big[S(\omega)\sin(\omega_m t) + C(\omega)\cos(\omega_m t) \Big] . \end{aligned} \tag{A.7}$$

For moderate $M \approx 1$ (where $J_2^2(M)$ is small and $J_\nu(M)$ can be neglected for $\nu > 2$) and small AM (where terms proportional to R^2 can be dropped) one obtains

$$\begin{aligned} S(\omega) =& J_0(M)J_1(M)\big(\phi_{+1} + \phi_{-1} - 2\phi_0\big) + J_1(M)J_2(M)\big(\phi_{+2} + \phi_{-2} - \phi_{+1} - \phi_{-1}\big) \\ & + \frac{1}{2}RJ_0^2(M)\Big[-\sin\psi\big(\phi_{-1} - \phi_{+1}\big) + \cos\psi\big(2 + 2\delta_0 - \delta_{+1} - \delta_{-1}\big)\Big] \\ & + \frac{1}{2}RJ_1^2(M)\Big[-\sin\psi\big(\phi_{-2} - \phi_{+2}\big) + \cos\psi\big(4 + 6\delta_0 - 2\delta_{+1} - 2\delta_{-1} - \delta_{+2} - \delta_{-2}\big)\Big] \end{aligned} \tag{A.8}$$

$$\begin{aligned} C(\omega) =& J_0(M)J_1(M)\big(\delta_{-1} - \delta_{+1}\big) + J_1(M)J_2(M)\big(\delta_{-2} - \delta_{+2} + \delta_{-1} - \delta_{+1}\big) \\ & + \frac{1}{2}RJ_0^2(M)\Big[\sin\psi\big(2 + 2\delta_0 - \delta_{+1} - \delta_{-1}\big) + \cos\psi\big(\phi_{-1} - \phi_{+1}\big)\Big] \\ & + \frac{1}{2}RJ_1^2(M)\Big[\sin\psi\big(4 + 6\delta_0 - 2\delta_{+1} - 2\delta_{-1} - \delta_{+2} - \delta_{-2}\big) + \cos\psi\big(\phi_{-2} - \phi_{+2}\big)\Big] . \end{aligned} \tag{A.9}$$

Note that the general procedure described here closely follows the derivation in [LEN84] but also includes some higher order contributions which become necessary for a typical phase modulation index of unity.

A.2 Line shape retrieval

Since a more detailed account on the line shape retrieval procedure is given in [WYN99B], only a few relevant aspects are summarized here.

Discretizing eq. (A.7) with equidistant frequency points ω_i $(i = 1, ..., n)$ leads to:

$$I_i \propto e^{-2\delta_i}\big(Y_i \sin\omega_m t + X_i \cos\omega_m t\big) \tag{A.10}$$

with $Y_i = Y(\omega_i)$, $X_i = X(\omega_i)$. Thus for n frequency points there are $2n$ equations for the $2n+8k$ unknowns $\delta_i, \phi_i, i = n-2, ..., n+2$, where k is defined by $\omega_m = k(\omega_i - \omega_{i-1})$. If $Y(\omega)$ and $X(\omega)$ drop off to zero near the edges of the scan range one can assume that $\delta_i = \phi_i = 0$ for $i < 1, i > n$ so that the number of equations matches the number of remaining unknowns. Furthermore, one

has to demand that k be integer, and that n be an integer multiple of k. If the experimental data do not comply with these conditions the spectra could first be resampled following a spline curve.

For small absorption the absolute change in δ_i near the resonance is small enough for the approximation of $\exp(-2\delta_i) \approx 1$ to be valid such that the nonlinearity vanishes from the set of equations. The remaining system of linear equations can simply be solved for the set (δ_i, ϕ_i), $i = 1, ..., n$ which is done numerically. Whereas the parameter M is chosen beforehand, the lock-in reference phase φ can usually be chosen correctly after a close inspection of the resulting (X, Y)-signals. Still, some difficulties arise from the fact that the parameters η, R and ψ are not known beforehand. However, once φ is known, ψ can be determined with the help of sum rules. In addition, a wrong choice of any parameter, including k, leads to characteristic jumps and excursions in the deconvoluted line shapes ($\delta(\omega)$, $\phi(\omega)$) such that R, ψ can be adjusted until all discontinuities in the deconvoluted line shapes have disappeared. Since the deconvolution process is numerically more involved for $\phi(\omega)$ than for $\delta(\omega)$ the S/N ratio in the deconvoluted spectrum is usually much better for $\delta(\omega)$ than it is for $\phi(\omega)$. For further discussion, examples, and limitations of the algorithm, see [WYN99B].

A.3 Double-modulation technique

Using the VCSEL set-up leads to a double-modulation of the laser current: 9.2 GHz sideband creation with an additional frequency-modulation in the kHz range for lock-in detection. Hence one might expect the modulation efficiency at 9.2 GHz and the inevitable AM at 9.2 GHz to interfere with the feature of interest. However, in the following paragraph it will be shown that the final formula obtained for such spectra is surprisingly easy and readily allows the application of the above deconvolution algorithm.

For the calculation of the resulting spectra one starts from an expression for the double-modulated light field. The optical frequency ω_0 is modulated by $x(t)$, oscillating at $\omega =$ 9.2 GHz, with frequency and amplitude contributions M_0, R_0, respectively. $x(t)$ is itself frequency-modulated by ω_m in the kHz range with a modulation index M according to: $x(t) = \omega t + M \sin(\omega_m t)$. Thus in total the field reads:

$$\begin{aligned} E &= \frac{E_0}{2}(1 + R_0 \sin(x(t) + \psi))e^{i(\omega_0 t + M_0 \sin(x(t))} + c.c. \\ &= \frac{E_0}{2}\Big[1 + R_0 \sin\big(\omega t + M \sin(\omega_m t) + \psi\big)\Big] e^{i\left(\omega_0 t + M_0 \sin(\omega t + M \sin(\omega_m t))\right)} + c.c. \\ &= \sum_{k,l} b_{kl} e^{i(\omega_0 + k\omega + l\omega_m)t} + c.c. \end{aligned} \tag{A.11}$$

with

$$\begin{aligned} b_{kl} &= J_l(kM) \cdot c_k \\ &= J_l(kM)\frac{E_0}{2}\left[J_k(M_0) - i\frac{R_0}{2}e^{i\psi}J_{k-1}(M_0) + i\frac{R_0}{2}e^{-i\psi}J_{k+1}(M_0)\right]. \end{aligned} \tag{A.12}$$

Again inserting transmission factors T_{kl}, this time depending on both the GHz sideband order k and the kHz sideband order l, the intensity on a square-law detector is given by

$$I_0 = \frac{1}{2}\epsilon_0 c\eta \sum_{k,l,m,n} b_{kl}b^*_{mn}T_{kl}T^*_{mn}e^{i\left((k-m)\omega+(l-n)\omega_m\right)t} + c.c. \tag{A.13}$$

For $k-m=0$, required because of the detector response bandwidth, and $l-n=\pm 1$, i.e., lock-in detection at ω_m, this leads to:

$$\begin{aligned} I = 2\epsilon_0 c\eta\Bigg[&- \mathrm{Im}\Big(\sum_{kl} b_{kl}b^*_{kl-1}T_{kl}T^*_{kl-1}\Big)\sin(\omega_m t) \\ &+ \mathrm{Re}\Big(\sum_{kl} b_{kl}b^*_{kl-1}T_{kl}T^*_{kl-1}\Big)\cos(\omega_m t)\Bigg]. \end{aligned} \tag{A.14}$$

Since the second order GHz-modulation sidebands are typically both weak and off-resonant, it is sufficient to evaluate the sum for $k=0,\pm 1$ only. Since b_{0l} vanishes for $l\neq 0$ the direct carrier contribution with $k=0$ is identically zero. Note that, of course, the carrier contribution is still contained in the non-linear transmission factors $T_{\pm 1l}$. Depending on which combination of the carrier- and first order GHz-sideband frequencies was used for dark state preparation the dominant signal contribution stems from either $k=+1$ or $k=-1$ whereas the respective other term is again off-resonant enough to be neglected. Hence with the same approximations made as in eqs. (A.8), (A.9) the signal can be calculated as:

$$I_k = 2k\epsilon_0 c\eta|c_k|^2\Big[S_0(\omega)\sin(\omega_m t) + C_0(\omega)\cos(\omega_m t)\Big], \tag{A.15}$$

where S_0, C_0 are given by eqs. (A.8), (A.9) with $R=0$, and

$$|c_k|^2 = \frac{E_0^2}{4}\left[J_1^2(M_0)\left(1+2k\frac{R_0}{M_0}\sin(\psi)+\frac{R_0^2}{M_0^2}\right) - \frac{R_0^2}{2}J_0(M_0)J_2(M_0)\left(1+\cos(2\psi)\right)\right]. \tag{A.16}$$

Depending on which sideband is used in the experiment, i.e., on whether the carrier frequency is near-resonant with the $F=4$ or the $F=3$ hyperfine transition, one has to choose $k=\pm 1$, respectively. From eq. (A.15) it becomes obvious that any dependence on the GHz-modulation parameters R_0, M_0, ψ is contained in the overall amplitude, and changing from $k=+1$ to $k=-1$ only results in a change of the overall amplitude. Therefore, the deconvolution method described in the preceding section can be applied to the spectra obtained with the double-modulation technique as well. However, in doing so, one finds that for the algorithm to work out one nevertheless has to chose $R\neq 0$ in some cases. Hence, some non-linearity in the whole system causes additional amplitude-modulation at ω_m, the origin of which is not known yet.

B Coefficients used in analytical solutions

The coefficients appearing in eqs. (2.12), (2.13), (2.14) for the analytical solution of ρ_{32} read:

$$
\begin{aligned}
A &= 64\gamma_{12}\Gamma_1^2(\gamma_1+\gamma_2)+16\Gamma_1 g_1^2(3\gamma_{12}+\gamma_2)\\
B &= 64\gamma_{12}(\gamma_1+\gamma_2)\\
C &= 32\gamma_{12}(4\Gamma_1^2+g_2^2)(\gamma_1+\gamma_2)+32\Gamma_1 g_1^2(3\gamma_{12}+\gamma_2)\\
D &= 128\gamma_{12}(\gamma_1+\gamma_2)\\
E &= 32(\gamma_1+\gamma_2)\gamma_{12}\Gamma_1(\Gamma_{12}g_2^2-\Gamma_1 g_1^2+2\Gamma_1\Gamma_2^2+2\Gamma_1\Gamma_{12}^2)\\
&\quad +4g_2^2(\gamma_1+\gamma_2)(\gamma_{12}g_2^2-\Gamma_1 g_1^2)+24\gamma_{12}\Gamma_1(2\Gamma_2(\Gamma_2 g_1^2+\Gamma_1 g_2^2)\\
&\quad +g_1^2(g_2^2-g_1^2))+4\Gamma_{12}g_1^2(g_2^2+4\Gamma_{12}\Gamma_1)(3\gamma_{12}+\gamma_2)+16\Gamma_1\Gamma_2\\
&\quad (\Gamma_1\gamma_1 g_2^2+\Gamma_2\gamma_2 g_1^2)-8\Gamma_1 g_1^2(\gamma_2 g_1^2-3\Gamma_2 g_2^2)\\
F &= 32(\gamma_1+\gamma_2)\gamma_{12}(2\Gamma_1^2+2\Gamma_2^2+2\Gamma_{12}^2+2g_2^2-g_1^2)+\\
&\quad 16g_2^2\Gamma_2(3\gamma_{12}+\gamma_1)+16\Gamma_1 g_1^2(3\gamma_{12}+\gamma_2)\\
G &= 64\gamma_{12}(\gamma_1+\gamma_2)\\
H &= (\gamma_1+\gamma_2)(4g_1^2g_2^2(\Gamma_2-\Gamma_1+\Gamma_{12})+8\gamma_{12}(8\Gamma_{12}\Gamma_1(2\Gamma_{12}\Gamma_1+g_2^2)+\\
&\quad 4\Gamma_2^2g_2^2-4g_1^2\Gamma_1^2+g_2^2(g_2^2-g_1^2)))+8g_1^2\Gamma_1(3\gamma_{12}+\gamma_2)(4\Gamma_{12}^2-g_1^2)\\
&\quad +8(3\gamma_{12}+\gamma_1)g_2^4\Gamma_2+8g_1^2g_2^2(3\gamma_{12}(\Gamma_1-\Gamma_2)+\Gamma_{12}\gamma_2)
\end{aligned}
$$

$$
\begin{aligned}
J &= 32\gamma_{12}(\gamma_1+\gamma_2)(4\Gamma_{12}^2+g_2^2-g_1^2)\\
K &= (\gamma_1+\gamma_2)(32\Gamma_{12}\Gamma_1\Gamma_2\gamma_{12}(2\Gamma_{12}\Gamma_1\Gamma_2+\Gamma_2 g_2^2+\Gamma_1 g_1^2)\\
&\quad +4\gamma_{12}(\Gamma_2 g_2^2+\Gamma_1 g_1^2)^2+g_1^2g_2^2(\Gamma_1 g_1^2+\Gamma_2 g_2^2+4\Gamma_{12}\Gamma_1\Gamma_2))\\
&\quad +\Gamma_2(3\gamma_{12}+\gamma_1)g_2^6+\Gamma_1(3\gamma_{12}+\gamma_2)g_1^6+3\gamma_{12}(g_1^2g_2^2+16\Gamma_{12}^2\Gamma_1\Gamma_2)\\
&\quad (\Gamma_2 g_1^2+\Gamma_1 g_2^2)+6g_1^2g_2^2(\Gamma_{12}-\gamma_{12})(\Gamma_2 g_2^2+\Gamma_1 g_1^2)+(g_1^2g_2^2\\
&\quad +16\Gamma_{12}^2\Gamma_1\Gamma_2)(\Gamma_1\gamma_1 g_2^2+\Gamma_2\gamma_2 g_1^2)+24\Gamma_{12}\gamma_{12}\Gamma_2\Gamma_1\\
&\quad (g_1^2-g_2^2)^2+24\Gamma_{12}g_2^2\Gamma_2\Gamma_1 g_1^2(\Gamma_{12}+\gamma_{12})+8\Gamma_{12}\Gamma_1\Gamma_2\\
&\quad (\gamma_2 g_1^4+\gamma_1 g_2^4)+12\Gamma_{12}\gamma_{12}g_1^2g_2^2(\Gamma_1^2+\Gamma_2^2)+4\Gamma_{12}g_1^2g_2^2\Gamma_2\gamma_2\\
&\quad (\Gamma_2-\Gamma_1)+4\Gamma_{12}g_1^2g_2^2\Gamma_1(\Gamma_2\gamma_2+\Gamma_1\gamma_1)\\
L &= 4(\gamma_1+\gamma_2)\gamma_{12}(8\Gamma_{12}(2\Gamma_{12}(\Gamma_1^2+\Gamma_2^2)+\Gamma_1 g_2^2+\Gamma_2 g_1^2)\\
&\quad +(g_1^2-g_2^2)^2)+8\Gamma_{12}(2\Gamma_{12}(3\gamma_{12}+\gamma_1)(\Gamma_2 g_2^2+\Gamma_1 g_1^2)\\
&\quad +g_1^2(\gamma_1(g_2^2-2\Gamma_{12}\Gamma_1)+\gamma_2(2\Gamma_{12}\Gamma_1+g_2^2)))\\
M &= 64\Gamma_{12}^2\gamma_{12}(\gamma_1+\gamma_2)
\end{aligned}
$$

$$
\begin{aligned}
A_i &= 4\Gamma_1\gamma_{12}(\gamma_1+\gamma_2)(4\Gamma_1\Gamma_2+g_1^2)+8\Gamma_1\Gamma_2 g_1^2\gamma_2 \\
B_i &= 16\Gamma_2\gamma_{12}(\gamma_1+\gamma_2) \\
C_i &= 4(\gamma_1+\gamma_2)(\Gamma_2\gamma_{12}(g_2^2-g_1^2)+\gamma_{12}(\Gamma_2 g_2^2+\Gamma_1 g_1^2)-\gamma_{12}\Gamma_{12}g_1^2) \\
D_i &= 16\Gamma_{12}^2\Gamma_2\gamma_{12}(\gamma_1+\gamma_2) \\
E_i &= (\gamma_1+\gamma_2)(16\Gamma_{12}^2\Gamma_1^2\Gamma_2\gamma_{12}-4g_1^2\Gamma_1\gamma_{12}\Gamma_2\Gamma_{12} \\
&\quad +4g_1^2\Gamma_1^2\Gamma_{12}\gamma_{12}+8\Gamma_{12}\Gamma_1\Gamma_2 g_2^2\gamma_{12}+g_1^2\Gamma_1 g_2^2\gamma_{12} \\
&\quad +g_2^4\Gamma_2\gamma_{12}-\gamma_{12}g_1^4\Gamma_1-\gamma_{12}\Gamma_2 g_1^2 g_2^2)+\gamma_2(2\Gamma_{12}g_1^2 \\
&\quad (\Gamma_2 g_2^2+\Gamma_1 g_1^2)+8\Gamma_2\Gamma_1\Gamma_{12}^2 g_1^2)
\end{aligned}
$$

$$
\begin{aligned}
A_r &= 16\gamma_{12}\Gamma_1^2(\gamma_1+\gamma_2)+8\Gamma_1 g_1^2\gamma_2 \\
B_r &= 16\gamma_{12}(\gamma_1+\gamma_2) \\
C_r &= 16\gamma_{12}\Gamma_1^2(\gamma_1+\gamma_2)+8\gamma_{12}g_2^2(\gamma_1+\gamma_2)-4g_1^2(\gamma_{12}(\gamma_1+\gamma_2) \\
&\quad -2\Gamma_1\gamma_2) \\
D_r &= 16\gamma_{12}(\gamma_1+\gamma_2) \\
E_r &= -4\Gamma_1^2\gamma_{12}(\gamma_1+\gamma_2)g_1^2-4g_1^2\Gamma_1\gamma_{12}(\gamma_1+\gamma_2)\Gamma_2 \\
&\quad +16\Gamma_{12}^2\Gamma_1^2\gamma_{12}(\gamma_1+\gamma_2)+8\Gamma_{12}\Gamma_1 g_2^2\gamma_{12}(\gamma_1+\gamma_2) \\
&\quad +\gamma_{12}(\gamma_2 g_2^2(g_2^2-g_1^2)+\gamma_1 g_2^2(g_2^2-g_1^2)-4g_1^2\Gamma_1\gamma_1\Gamma_{12}) \\
&\quad -2\Gamma_1 g_1^2(\gamma_2 g_1^2+\gamma_1 g_2^2)+2\Gamma_{12}g_1^2\gamma_2(g_2^2+4\Gamma_{12}\Gamma_1) \\
&\quad -4g_1^2\Gamma_1\gamma_{12}\Gamma_{12}\gamma_2 \\
F_r &= 8(\gamma_1+\gamma_2)\gamma_{12}(2\Gamma_{12}^2+g_2^2-g_1^2) \\
G_r &= (\gamma_1+\gamma_2)(2g_2^2\Gamma_{12}(g_1^2+4\Gamma_1\gamma_{12})+\gamma_{12}(g_1^2-g_2^2)^2 \\
&\quad +4\Gamma_{12}\gamma_{12}(4\Gamma_{12}\Gamma_1^2+(\Gamma_2-\Gamma_1)g_1^2))+8\Gamma_{12}^2\Gamma_1 g_1^2\gamma_2 \\
H_r &= 16\Gamma_{12}^2\gamma_{12}(\gamma_1+\gamma_2)\,.
\end{aligned}
$$

C Modulation efficiency of the VCSEL

For a quantitative description of the measured modulation characteristics one starts once more from an amplitude- and frequency-modulated electric field with modulation indices R, M, respectively, modulation frequency ω_m and carrier frequency ω_0:

$$\begin{aligned} E &= \frac{E_0}{2}\Big(1 + R\sin(\omega_m + \psi)\Big)e^{i(\omega_0 t + M\sin(\omega_m t))} + c.c. \\ &= \sum_{n=-\infty}^{+\infty} a_n e^{i(\omega_0 + n\omega_m)} + c.c., \end{aligned} \tag{C.1}$$

with

$$a_n = \frac{E_0}{2}\Big(J_n(M) - i\frac{R}{2}e^{i\psi}J_{n-1}(M) + i\frac{R}{2}e^{-i\psi}J_{n+1}(M)\Big) \tag{C.2}$$

where $J_n(M)$ is the nth Bessel function of M. Inserting the complex transmission coefficients $T_n = T(\omega_0 + n\omega_m) = \exp(-\delta_n - i\phi_n)$, similarly to the procedure described in appendix A, the intensity on the detector behind the cesium cell reads:

$$\begin{aligned} I &\propto \sum_{n,k}(a_n T_n e^{i(\omega_0 + n\omega_m)t} + c.c.)(a_k T_k e^{i(\omega_0 + n\omega_m)t} + c.c.) \\ &\propto \sum_n |a_n|^2 |T_n|^2 \\ &= \sum_n |a_n|^2 e^{-2\delta_n} \end{aligned} \tag{C.3}$$

where all oscillating terms are averaged out because both frequencies ω_0 and ω_m are too fast for the photodiode response bandwidth. Hence the strength of the nth sideband $S_n = |a_n|^2$ is given by

$$S_n = \frac{J_n^2(M)(1 + 2n\frac{R}{M}\sin(\psi) + n^2\frac{R^2}{M^2}) - \frac{R^2}{2}J_{n-1}J_{n+1}(1 + \cos(2\psi))}{1 + \frac{R^2}{2}} \tag{C.4}$$

where the total line strength has been normalized to unity:

$$\sum_n S_n = 1 \quad . \tag{C.5}$$

D Decay rates and Rabi frequencies

For the unperturbed cesium atom the decay rates must be proportional to the corresponding dipole transition rate averaged over polarizations q and all Zeeman sublevels. Hence for a given upper state hyperfine component F' one has

$$\begin{aligned}
\gamma_i &\propto \sum_{q,m_F,m'_F} |\langle F'\ m'_F|\, r_q\, |F_i\ m_F\rangle|^2 \\
&= |\langle F'\|r\|F_i\rangle|^2 \sum_{m_F,m'_F} \begin{pmatrix} F' & 1 & F_i \\ -m'_F & m'_F - m_F & m_F \end{pmatrix}^2 \\
&= \frac{1}{2F'+1} |\langle F'\|r\|F_i\rangle|^2 \\
&= (2F_i+1) \begin{Bmatrix} J' & F' & I \\ F_i & J & 1 \end{Bmatrix}^2 |\langle J'\|r\|J\rangle|^2\,, \qquad i = 1,2\,,
\end{aligned} \tag{D.1}$$

where the Wigner-Eckart theorem and properties of $3j$- and $6j$-symbols have been used. With $F_1 = 4$, $F_2 = 3$ this results in

$$\frac{\gamma_1}{\gamma_2} = \frac{2F_1+1}{2F_2+1} \frac{\begin{Bmatrix} J' & F' & I \\ F_1 & J & 1 \end{Bmatrix}^2}{\begin{Bmatrix} J' & F' & I \\ F_2 & J & 1 \end{Bmatrix}^2}\,, \tag{D.2}$$

i.e.,

$$\begin{aligned}
\gamma_1/\gamma_2 &= 7/5 \qquad &&\text{for } F' = 4 \\
\gamma_1/\gamma_2 &= 1/3 \qquad &&\text{for } F' = 3\,,
\end{aligned} \tag{D.3}$$

with $\gamma_0 = \gamma_1 + \gamma_2 = 2\pi \cdot 5.3\,\mathrm{MHz}$ for the cesium D_2 line.

As for the Rabi frequencies, one has to consider two different aspects. Relative Rabi frequencies depend on angular momentum coupling and can be treated in a similar way as the decay rates. Absolute values of the Rabi frequencies have to be related to experimentally measured intensities.

According to eq. (2.2) the Rabi frequencies g_i were defined as $g_i^2 = \frac{|E_i|^2}{\hbar^2}|d_{3i}|^2$. With intensities $I_i = \frac{1}{2}c\epsilon_0|E_i|^2$, and for a laser polarization described by r_q this yields

$$\begin{aligned}
g_i^2 &= \frac{2I_i e^2}{\hbar^2\epsilon_0 c} |\langle P_{3/2}\, F'\, m_{F'}|\, r_q\, |S_{1/2}\, F_i\, m_{F_i}\rangle|^2 \\
&= \frac{2I_i e^2}{\hbar^2\epsilon_0 c}(2F'+1)(2F_i+1) \begin{pmatrix} F' & 1 & F_i \\ -m_{F'} & q & m_{F_i} \end{pmatrix}^2 \begin{Bmatrix} J' & F' & I \\ F_i & J & 1 \end{Bmatrix}^2 |\langle 6P_{3/2}\|r\|6S_{1/2}\rangle|^2\,.
\end{aligned} \tag{D.4}$$

Hence the scaling factors $W_i(F')$ for the relative Rabi frequencies of eq. (3.42) result.

For the absolute Rabi frequencies the reduced matrix element of eq. (D.4) can be related to the experimentally accessible lifetime $\tau = 33\,\mathrm{ns}$ via the Einstein coefficient $A = 1/\tau$:

$$A = \frac{2e^2\omega^3}{3\epsilon_0 hc^3}\frac{1}{(2J'+1)}|\langle 6P_{3/2}\|r\|6S_{1/2}\rangle|^2 . \tag{D.5}$$

For simplicity, the Rabi frequencies will also be written as

$$g_i^2 = G(I_i)\cdot(2F'+1)(2F_i+1)\begin{pmatrix} F' & 1 & F_i \\ -m_{F'} & q & m_{F_i}\end{pmatrix}^2\begin{Bmatrix} J' & F' & I \\ F_i & J & 1\end{Bmatrix}^2 , \tag{D.6}$$

with

$$G(I_i) := \frac{3\lambda^3}{2\pi hc\tau}(2J'+1)I_i . \tag{D.7}$$

References

[AFF99] C. AFFOLDERBACH, *Dunkelresonanz-Spektroskopie mit vertikal emittierenden Diodenlasern*, Diploma thesis, Bonn University (1999), in German.

[ALE94] E. B. ALEXANDROV, M. V. BALABAS, A. K. VERSHOVSKII, A. E. IVANOV, N. N. YAKOBSON, V. L. VELICHANSKII, N. V. SENKOV, *Laser Pumping in the Scheme of an Mx-Magnetometer*, Optics and Spectroscopy **78**, 292–298 (1995).

[ALL82] N. ALLARD, J. KIELKOPF, *The effect of neutral nonresonant collisions on atomic spectral lines*, Rev. Mod. Phys. **54**, 1103–1182 (1982).

[ALZ76] G. ALZETTA, A. GOZZINI, L. MOI, G. ORRIOLS, *An experimental method for the observation of r. f. transitions and laser beat resonances in oriented Na vapor*, Il Nuovo Cim. **36B**, 5–20 (1976).

[ARI94] E. ARIMONDO, *Limits in preparation of coherent population trapping states*, in: Fundamentals of Quantum Optics III, Lecture Notes in Physics **420**, ed. F. Ehlotzky (Springer, Berlin), pp. 170–184 (1994).

[ARI96A] E. ARIMONDO, *Coherent population trapping in laser spectroscopy*, Progress in Optics **XXXV**, 257–354 (1996).

[ARI96B] E. ARIMONDO, *Relaxation processes in coherent-population trapping*, Phys. Rev. A **54**, 1–8 (1996).

[ASP88] A. ASPECT, E. ARIMONDO, R. KAISER, N. VANSTEENKISTE, C. COHEN–TANNOUDJI, *Laser cooling below the one-photon recoil energy by velocity-selective coherent population trapping*, Phys. Rev. Lett. **61**, 826–829 (1988).

[BEC95] H. BECKER, *From nanotesla to picotesla – a new window for magnetic prospecting in archaeology*, Archaeological Prospection **2**, 217–228 (1995).

[BEV71] N. BEVERINI, P. MINGUZZI, F. STRUMIA, *Foreign-gas-induced cesium hyperfine relaxation*, Phys. Rev. A **4**, 550–555 (1971).

[BEV81] N. BEVERINI, F. STRUMIA, G. ROVERA, *Buffer gas pressure shift in the $m_F = 0 \rightarrow m_F = 0$ ground state hyperfine line in Cs*, Opt. Commun. **37**, 394–396 (1981).

[BHA80] N. D. BAHSKAR, J. PIETRAS, J. CAMPARO, W. HAPPER, *Spin destruction in Collisions between Cesium Atoms*, Phys. Rev. Lett. **44**, 930–933 (1980).

[BJO83] G. C. BJORKLUND, M. D. LEVENSON, W. LENTH, C. ORTIZ, *Frequency modulation (FM) spectroscopy*, Appl. Phys. B **32**, 145–152 (1983).

[BON84] K. D. BONIN, T. J. MCILRATH, *Two-photon electric-dipole selection rules*, J. Opt. Soc. Am. **1**, 52–55 (1984).

[BOU74] M. A. BOUCHIAT, C. BOUCHIAT, *I. Parity violation induced by weak neutral currents in atomic physics*, J. Phys. (Paris) **35**, 899–927 (1974).

[BRA96] S. BRANDT, *Kohärente Dunkelzustände im Cäsiumdampf unter dem Einfluss von Puffergas*, Diploma thesis, Bonn University (1996), in German.

[BRA97] S. BRANDT, A. NAGEL, R. WYNANDS, D. MESCHEDE, *Buffer-gas-induced linewidth reduction of coherent dark resonances to below 50 Hz*, Phys. Rev. A **56**, R1063–R1066 (1997).

[CAG73] B. CAGNAC, G. GRYNBERG, F. BIRABEN, *Spectroscopie d'absorption multiphotonique sans effect Doppler*, J. de Physique **34**, 845–858 (1973).

[CHA98] J. CHANG-HASNAIN, *VCSELs. Advances and future prospects*, Optics & Photonics News (5) 34–39 (May 1998).

[COH69] C. COHEN-TANNOUDJI, J. DUPONT-ROC, S. HAROCHE, F. LALOË, *Detection of the static magnetic field produced by the oriented nuclei of optically pumped ^{3}He gas*, Phys. Rev. Lett. **22**, 758–760 (1969).

[COH92] B. LOUNIS, C. COHEN-TANNOUDJI, *Coherent population trapping and Fano profiles*, J. Phys. II France **2**, 579–592 (1992).

[DIC53] R. H. DICKE, *The effect of Collisions upon the Doppler Width of Spectral Lines*, Phys. Rev. **89**, 472–473 (1953).

[EBE97] K. J. EBELING, *Diodenlaser für die Kommunikation: Vertikaldiodenlaser (VCSEL)*, DPG Summer School on diode lasers, Bad Honnef (1997), unpublished.

[ENL65] L. H. ENLOE, J. L. RODDA, *Laser phase-locked loop*, Proc. IEEE **53**, 165–166 (1965).

[FLE94] M. FLEISCHHAUER, M. O. SCULLY, *Quantum sensitivity limits of an optical magnetometer based on atomic phase coherence*, Phys. Rev. A **49**, 1973–1986 (1994).

[FLE95] M. FLEISCHHAUER, M. O. SCULLY, *Magnetometer based on atomic coherence and possible application to the search for P and T violating permanent electric dipole moments of atoms*, Quantum Semiclass. Opt. **7**, 297–305 (1995).

[GAL61] L. GALATRY, *Simultaneous Effect of Doppler and Foreign Gas broadening on Spectral Lines*, Phys. Rev. **122**, 1218–1223 (1961).

[GAR79] F. M. GARDNER, *Phaselock Techniques*, J. Wiley & Sons (1979).

[GEH85] M. GEHRTZ, G. C. BJORKLUND, E. A. WHITTAKER, *Quantum-limited laser frequency-modulation spectroscopy*, J. Opt. Soc. Am. B **2**, 1510 (1985).

[GRA97] L. GRAF, *Magnetometrie mit kohärenten Dunkelzuständen*, Diploma thesis, Bonn University (1997), in German.

[GRI98] B. A. GRISHANIN, V. N. ZADKOV, D. MESCHEDE, *Modification of resonance fluorescence and absorption in a Λ-system by four-wave mixing*, Phys. Rev. A **58**, 4235–4238 (1998).

[GRO94] R. GROBE, F. T. HIOE, J. H. EBERLY, *Formation of shape-preserving pulses in a nonlinear adiabatically integrable system*, Phys. Rev. Lett. **73**, 3183–3186 (1994).

[HAG79] H. E. HAGEMEIER, S. R. ROBINSON, *Field properties of multiple coherently combined lasers*, Appl. Opt. **18**, 270–280 (1979).

[HÄM93] M. HÄMÄLÄINEN, R. HARI, R. ILMONIEMI, J. KNUUTILA, O. V. LOUNASMAA, *Magnetoencephalography — theory, instrumentation, and applications to noninvasive studies of the working human brain*, Rev. Mod. Phys. **65**, 413–491 (1993).

[HAP67] W. HAPPER, B. S. MATHUR, *Effective operator formalism in optical pumping*, Phys. Rev. **163**, 12–25 (1967).

[HAP72] W. HAPPER, *Optical Pumping*, Rev. Mod. Phys. **44**, 169–249 (1972).

[HAU99] L. V. HAU, S. E. HARRIS, Z. DUTTON, C. H. BEHROOZI, *Light speed reduction to 17 metres per second in an ultracold atomic gas*, Nature **397**, 594–598 (1999).

[HEM83] P. R. HEMMER, S. EZEKIEL, C. C. LEIBY, JR., *Stabilization of a microwave oscillator using a resonance Raman transition in a sodium beam*, Opt. Lett. **8**, 440–442 (1983).

[HEM93] P. R. HEMMER, M. S. SHAHRIAR, H. LAMELA-RIVERA, S. P. SMITH, B. E. BERNACKI, S. EZEKIEL, *Semiconductor laser excitation of Ramsey fringes by using a Raman transition in a cesium atomic beam*, J. Opt. Soc. Am. B **10**, 1326–1329 (1993).

[HER68] R. M. HERMAN, *Rare-gas-induced g_J shifts in the ground states of alkali atoms*, Phys. Rev. **175**, 10–11 (1968).

[HER86] P. P. HERRMANN, J. HOFFNAGLE, N. SCHLUMPF, V. L. TELEGDI, A. WEIS, *Stark spectroscopy of forbidden two-photon transitions: a sensitive probe for the quantitative measurement of small electric fields*, J. Phys. B: At. Mol. Opt. Phys. **19**, 1271–1280 (1986).

[JAE97] R. JÄGER, M. GRABHERR, C. JUNG, R. MICHALZIK, G. REINER, B. WEIGL, K. J. EBELING, *57% wallplug efficiency oxide-confined 850nm wavelength GaAs VCSELs*, Electron. Lett. **33**, 330–331 (1997).

[JUN97] C. JUNG, R. JÄGER, M. GRABHERR, P. SCHNITZER, R. MICHALZIK, B. WEIGL, S. MÜLLER, K. J. EBELING, *4.8mW singlemode oxide confined top-surface emitting vertical-cavity laser diodes*, Electron. Lett. **33**, 1790–1791 (1997).

[KAI85] M. KAIVOLA, P. THORNSEN, O. POULSEN, *Dispersive line shapes and optical pumping in a three-level system*, Phys. Rev. A **32**, 207–213 (1985).

[KAN96] H. KANAKOGI, K. SAKURAI, *Optical dark resonance in multilevel systems with a treelike configuration*, Phys. Rev. A **54**, 2334–2346 (1996).

[KAS95] A. KASAPI, M. JAIN, G. Y. YIN, S. E. HARRIS, *Electromagnetically Induced Transparency: Propagation Dynamics*, Phys. Rev. Lett. **74**, 2447–2450 (1995).

[KAS99] M. M. KASH, V. A. SAUTENKOV, A. S. ZIBROV, L. HOLLBERG, G. R. WELCH, M. D. LUKIN, Y. ROSTOVTSEV, E. S. FRY, M. O. SCULLY, *Ultra-Slow Light and Enhanced Nonlinear Optical Effects in a Coherently Driven Hot Atomic Gas*, submitted to Phys. Rev. Lett. (1999).

[KEL94] P. L. KELLEY, P. J. HARSHMAN, O. BLUM, T. K. GUSTAFSON, *Radiative renormalization analysis of optical double resonance*, J. Opt. Soc. Am. B **11**, 2298–2302 (1994).

[KIN98] R. KING, R. MICHALZIK, C. JUNG, M. GRABHERR, F. EBERHARD, R. JÄGER, P. SCHNITZER, K. J. EBELING, *Oxide confined 2D VCSEL arrays for high-density inter/intra-chip interconnects*, in: Vertical-Cavity Surface-Emitting Lasers II, Hrsg. R. A. Morgan and K. D. Choquette, 64–71, Proc. SPIE 3286 (1998).

[KNA99] S. KNAPPE, Bonn University, private communication (1998).

[KOR97] E. A. KORSUNSKY, W. MAICHEN, L. WINDHOLZ, *Dynamics of coherent optical pumping in a sodium atomic beam*, Phys. Rev. A **56**, 3908–3915 (1997).

[LAN97] S. LANG, *Optisch detektierte Magnetresonanz an Cäsium Atomen in festem* ^4He, Dissertation der Fakultät für Physik der Ludwig-Maximilians-Universität München (1997), in German.

[LEE98] H. LEE, M. FLEISCHHAUER, M. O. SCULLY, *Sensitive detection of magnetic fields including their orientation with a magnetometer based on atomic phase coherence*, Phys. Rev. A **58**, 2587–2595 (1998).

[LEN84] W. LENTH, *High frequency heterodyne spectroscopy with current-modulated diode lasers*, IEEE J. Quantum Electron. **QE-20**, 1045–1050 (1984).

[LIN96] H. Y. LING, Y. Q. LI, M. XIAO, *Coherent population trapping and electromagnetically induced transparency in multi-Zeeman-sublevel atoms*, Phys. Rev. A **53** 1014–1026 (1997).

[LOU83] R. LOUDON, *The quantum theory of light*, Oxford University Press (Oxford 1983).

[LUK96] M. D. LUKIN, M. O. SCULLY, G. R. WELCH, E. S. FRY, L. HOLLBERG, G. G. PADMABANDU, H. G. ROBINSON, A. S. ZIBROV, *Lasing without Inversion: the Road to New Short-Wavelength Lasers*, Laser Physics **3**, 436-444 (1996).

[MAC92] K. B. MACADAM, A. STEINBACH, C. WIEMAN, *A narrow-band tunable diode laser system with grating feedback, and a saturated absorption spectrometer for Cs and Rb*, Am. J. Phys. **60**, 1098–1111 (1992).

[MYA93] C. J. MYATT, N. R. NEWBURY, C. E. WIEMAN, *Simplified atom trap by using direct microwave modulation of a diode laser*, Opt. Lett. **18**, 649–651 (1993).

[NAG98] A. NAGEL, L. GRAF, A. NAUMOV, E. MARIOTTI, V. BIANCALANA, D. MESCHEDE, R. WYNANDS, *Experimental realization of coherent dark-state magnetometers*, Europhys. Lett. **44**, 31-36 (1998).

[ORR79] G. ORRIOLS, *Nonabsorption Resonances by Nonlinear Coherent Effects in a Three-Level System*, Il nuovo cimento **53 B, 1**, 1–23 (1979).

[PRE95] M. PREVEDELLI, T. FREEGARDE, T. W. HÄNSCH, *Phase locking of grating-tuned diode lasers*, Appl. Phys. B **60**, S241–S248 (1995).

[REN97] F. RENZONI, W. MAICHEN, L. WINDHOLZ, E. ARIMONDO, *Coherent population trapping with losses observed on the Hanle effect of the D_1 sodium line*, Phys. Rev. A **55**, 3710–3718 (1997).

[REN98] F. RENZONI, E. ARIMONDO, *Population-loss-induced narrowing of dark resonances*, Phys. Rev. A **58**, 4717–4722 (1998).

[ROM82] G. L. ROMANI, S. J. WILLIAMSON, L. KAUFMAN, *Biomagnetic Instrumentation*, Rev. Sci. Instrum. **53**, 1815–1845 (1982).

[SCH94] O. SCHMIDT, K.-M. KNAAK, R. WYNANDS, D. MESCHEDE, *Cesium saturation spectroscopy revisited: How to reverse peaks and observe narrow resonances*, Appl. Phys. B **59**, 167–178 (1994).

[SCH95] O. SCHMIDT, *Dunkelzustände in Cäsiumdampf*, Ph. D. thesis, Hannover University (1995), in German.

[SCH96] W. SCHMID, C. JUNG, B. WEIGL, G. REINER, R. MICHALZIK, K. J. EBELING, *Delayed Self-Heterodyne Linewidth Measurement of VCSEL's*, IEEE Phot. Tech. Lett. **8**, 1288–1290 (1996).

[SCU92] M. O. SCULLY, M. FLEISCHHAUER, *High-sensitivity magnetometer based on index-enhanced media*, Phys. Rev. Lett. **69**, 1360–1363 (1992).

[SIE92] I. SIEMERS, M. SCHUBERT, R. BLATT, W. NEUHAUSER, P. E. TOSCHEK, *The ≪Trapped State≫ of a Trapped Ion — Line Shifts and Shape*, Europhys. Lett. **18**, 139–144 (1992).

[SWE88] D. R. SWENSON, L. W. ANDERSON, *Relaxation rates for optically pumped Na vapor on silicone surfaces*, Nucl. Instrum. Meth. **B29**, 627–642 (1988).

[TAI96] A. V. TAICHENACHEV, A. M. TUMAIKIN, V. I. YUDIN, *An atom in an elliptically polarized resonant field: the exact steady-state solution for closed $j_g = j \to j_e = j + 1$ transitions*, JETP **83**, 949–961 (1996).

[TAK75] K. TAKAGI, R. F. CURL, R. T. M. SU, *Spectroscopy with modulation sidebands*, Appl. Phys. **7**, 181–185 (1975).

[TEL90] H. R. TELLE, H. LI, *Phase-locking of laser diodes*, Electron. Lett. **26**, 858–859 (1990).

[THO80] J. E. THOMAS, W. W. QUIVERS, *Transit-time effects in optically pumped coupled three-level systems*, Phys. Rev. A **22**, 2115–2121 (1980).

[THO82] J. E. THOMAS, P. R. HEMMER, S. EZEKIEL, C. C. LEIBY, JR., R. H. PICARD, C. R. WILLIS, *Observation of Ramsey fringes using a stimulated, resonance Raman transition in a sodium atomic beam*, Phys. Rev. Lett. **48**, 867–870 (1982).

[VAN89] J. VANIER, C. I. AUDOIN, *The Quantum Physics of Atomic Frequency Standards, Vol.1*, Adam Hilger (Bristol and Philadelphia, 1989).

[WÄC97] G. WÄCKERLE, Stuttgart University, private communication (1997).

[VOD92] W. VODEL, K. MÄKINIEMI, *An ultra low noise DC SQUID system for biomagnetic research*, Meas. Sci. Technol. **3**, 1155–1160 (1992).

[WAL97] T. G. WALKER, W. HAPPER, *Spin-exchange optical pumping of noble-gas nuclei*, Rev. of Mod. Phys. **69**, 629–642 (1997).

[WHI73] C. W. WHITE, W. M. HUGHES, G. S. HAYNE, H. G. ROBINSON, *Determination of g-factors for free ^{133}Cs and ^{87}Rb atoms*, Phys. Rev. A **7**, 1178–1182 (1973).

[WIE91] C. E. WIEMAN, L. HOLLBERG, *Using diode lasers for atomic physics*, Rev. Sci. Instrum. **62**, 1–20 (1991).

[Woo97] C. S. Wood, S. C. Bennett, D. Cho, B. P. Masterson, J. L. Roberts, C. E. Tanner, C. E. Wieman, *Measurement of parity nonconservation and an anapole moment in cesium*, Science **275**, 1759–1763 (1997).

[Wyn98a] R. Wynands, A. Nagel, S. Brandt, D. Meschede, A. Weis, *Selection rules and line strengths of Zeeman-split dark resonances*, Phys. Rev. A **58**, 196–203 (1998).

[Wyn98b] R. Wynands, *Precision spectroscopy with Coherently Coupled Laser*, Habilitation thesis, Bonn University (1998).

[Wyn99a] R. Wynands, A. Nagel, *Precision spectroscopy with coherent dark states*, Appl. Phys. **B, 68**, 1–25 (1999).

[Wyn99b] R. Wynands, A. Nagel, *Inversion of frequency modulation (FM) spectroscopy line shapes*, submitted to J. Opt. Soc. Am. B.

[Yar91] A. Yariv, *Optical Electronics*, Saunders College Publishing, 4th Ed. (1991).

[Yur76] M. A. Yuratich, D. C. Hanna, *Nonlinear atomic susceptibilities*, J. Phys. B: Atom. Molec. Phys. **9**, 729–750 (1976).

[Zib95] A. S. Zibrov, M. D. Lukin, D. E. Nikonov, L. Hollberg, M. O. Scully, V. L. Velichansky, H. G. Robinson, *Experimental Demonstration of Laser Oscillation without Population Inversion via Quantum Interference in Rb*, Phys. Rev. Lett. **75**, 1499–1502 (1995).

Thank you

I feel very grateful towards the people who supported me in many different ways during the last three years.
In particular, I want to thank Robert, for everything from teaching me the Abc of dark resonances, Betreuungseinheiten, criticism and discussions to yummy cookies and his zest.
It was real fun in the lab with Christoph and Svenja, carrying to and fro so many cups of hot drinks, exchanging bits of relevant literature, and taking care of our baby, the VCSEL.
Speaking of cups, I definitely liked Michael's tea and I was glad we shared the job in next door's basement hole.
From cups to glasses: I hope I'll win the quest for the case of champagne. But in any case, the refreshment I got on the third floor was not only due to the doses of caffein. Probably, I would have needed less pens, had I not enjoyed the chat with Dagmar and Fien.
From the taming of the phase-lock to the creation of pieces of modern art, such as the wrapped experiment and the coffin, I liked working with Steffie and Lutz.
There are situations I'll remember such as our exhausting trip to the underworld, although we did not discover any well kept secrets and somehow missed the dragon.
To all those who suddenly found themselves serving me coffee or beer: I really enjoyed the game.
Many members of the group contributed towards the relaxed atmosphere of great helpfulness which I found very pleasant.
I won't forget 'the Italians', in particular Emilio, Valerio, Luigi, Carmen and Olga, and the trips to Pisa and Lerici.
Finally, I want to thank Prof. Meschede for his understanding and support, and for having given me opportunities well off the beaten track. I really appreciated the opportunity to spend half a year in Italy and the freedom to proceed basically as we wanted to.

I thank my parents, family and friends.